

Nanoscale organic / inorganic hybrid photovoltaic devices

A dissertation submitted to the

École Polytechnique Fédérale De Lausanne

for the degree of

Docteur ès Sciences

by

Thomas Dufaux

Abstract

There is an increasing trend of using various types of nanostructures as components of solar cells. This highlights the need to gain a deeper understanding of the nanoscale interface in such devices. The present thesis aims to study individual photoactive junctions as the elementary functional unit of bulk photovoltaic devices, and exploit the gained knowledge toward further improving the solar cells' efficiency.

Along this direction, Schottky-contacts to cadmium sulphide nanowires were thoroughly studied using scanning photocurrent microscopy (SPCM). In conjunction with theoretical simulations of the measured photocurrent profiles, it was found that charge carriers can be very efficiently extracted out of a few micrometer long nanowire segments below the metal contact. Moreover, the carrier combination rate in this section could be determined as a function of an applied bias or backgate voltage. These findings provide valuable clues about how electric fields are distributed within semiconductor nanowire-based devices.

Moreover, SPCM was employed to explore the local photoresponse along graphene/CdS heterojunctions, representing a first step toward implementing graphene as an active acceptor material into solar cells. The short circuit current of such devices could be enhanced by two orders of magnitudes through chemical tailoring of the graphene-CdS interface. In addition, evidence was obtained that surface plasmon excitation in the metal contacts can make significant contributions to the generated photocurrent. This effect was exploited in the fabrication of novel surface plasmon detectors, which support different plasmon modes depending on the polarization direction of the incoming light.

Finally, it was attempted to realize photovoltaic devices comprising a pn-junction implemented into a π -conjugated organic polymer. While the electric-field assisted exciton dissociation in this system could be successfully modelled in the framework of the Braun-Onsager model, photoinduced charge separation at the interface between differently gated regions of the polymer could not be achieved due to insufficient electron conduction of the material.

Keywords: hybrid solar cell, nanowire, scanning photocurrent microscopy, surface plasmons,

exciton dissociation, Onsager-Braun model, interface engineering, nanoscale photojunction, model systems, drift- and diffusion current, Schottky-contact

Zusammenfassung

Fortschritte in der Nanotechnologie erlaubt es zunehmend Nanostrukturen in Solarzellen zu verwenden. Hierfür ist ein tieferes Verständnis der Eigenschaften von Grenzflächen im Nanobereich notwendig. Die vorliegende Doktorarbeit befasst sich mit einzelnen, photoaktiven Halbleiterübergängen, welche die elementaren Funktionseinheiten von nanostrukturierten Solarzellen nachbilden. Die gewonnenen Erkenntnisse sind viel versprechend, um die Effizienz von nanostrukturierten Solarzellen weiter zu verbessern.

Im Hinblick auf diese Zielsetzung wurden Schottky-Kontakte an Cadmiumsulfid-Nanodrähten mittels Rasterphotostrommikroskopie untersucht. Anhand numerischer Modellrechnungen der Stromprofile konnte gezeigt werden, dass eine sehr effiziente Ladungsträgerextraktion innerhalb eines Mikrometers entlang des Kontaktes möglich ist. Außerdem gelang es die Ladungsträger Rekombinationsrate innerhalb des Schottky-Kontaktes in Abhängigkeit einer angelegten Spannung zu bestimmen. Diese Experimente geben somit wertvollen Aufschluss über die Verteilung elektrischer Felder innerhalb von Halbleiter-Nanodraht Kontakten.

Darüber hinaus wurde der Photostrom entlang eines Graphen/CdS-Nanodraht-Heteroübergangs mit Rasterphotostrommikroskopie untersucht, was einen ersten Schritt in Richtung der Verwendung von Graphen als aktives Akzeptormaterial in Solarzellen darstellt. Der Kurzschlussstrom konnte durch Verbesserungen der Graphene/CdS Grenzfläche um zwei Größenordnungen erhöht werden. Außerdem wurde die Anregung von Oberflächenplasmonen an den Metallkontakten beobachtet, welche einen signifikanten Anteil zum Photostrom beitragen können. Dieser Effekt wurde ausgenutzt um neuartige Detektoren für Oberflächenplasmonen zu entwickeln, welche in Abhängigkeit von der gewählten Lichtpolarisation verschiedene Moden detektieren können.

Schließlich wurde eine Solarzelle basierend auf einem pn-Übergang innerhalb eines π -konjugierten, organischen Polymers untersucht. Die Exzitonen-Dissoziation durch ein externes elektrisches Feld, konnte anhand des Onsager-Braun Modells erklärt werden. Allerdings war es nicht möglich, eine Ladungsträgertrennung zwischen den Gate-Bereichen zu messen, was auf die begrenzte Elektronenleitfähigkeit des Polymers zurückgeführt wurde.

Schlagwörter: Hybride Solarzellen, Nanodrähte, Rasterphotostrommikroskopie, Oberflächen-

plasmonen, Exzitonen Dissoziation, Onsager-Braun Modell, Grenzflächen im Nanobereich, Modellsysteme, Drift und Diffusionsströme, Schottky-Kontakte

Contents

1	Introduction	7
2	Fundamentals of solar cells	11
2.1	Semiconductor basics	11
2.1.1	Charge transport in semiconductors	11
2.1.2	PN-junction	16
2.1.3	Photoconversion efficiency	20
2.2	Novel materials for solar cells	21
2.2.1	Organic bulk-heterojunction solar cells	22
2.2.2	Hybrid solar cells	24
2.2.3	Dye-sensitized solar cells	26
2.2.4	Plasmon enhancement	28
3	Cadmium sulfide nanowire Schottky-contacts	31
3.1	Photoresponse distribution	31
3.2	Calculated electric potential along a nanowire/metal contact	34
3.3	Drift- and diffusion-currents	36
4	Graphene-Cadmium sulfide solar cells	43
4.1	Solar cell structure and assembly	43
4.2	Chemical interface tailoring	45
4.3	Device performance and efficiency	47
5	Electrical detection of surface plasmons	49
5.1	Surface plasmons in Graphene-CdS nanowire solar cells	49
5.2	Electrical detection of SPPs	51
5.2.1	Polarization dependence	53
5.2.2	FDTD calculations	54

5.2.3	Position-dependent coupling efficiency	55
5.2.4	Bias dependence	56
6	Hybrid organic solar cells	59
6.1	Anodic oxidation of titanium	59
6.2	Photocurrent distribution in TiO ₂ /P3HT/Au devices	61
6.3	Blend solar cells: Ligand exchange of CdSe NP	61
6.4	Nanostructured solar cells: charge transfer at CdS-P3HT heterojunction	64
7	Field-stimulated exciton dissociation	67
7.1	Limitations of bulk heterojunction solar cells	67
7.2	The Onsager-Braun model of exciton dissociation	67
7.2.1	Charge transfer states in π -conjugated polymers	68
7.2.2	Field-assisted exciton dissociation	69
7.3	SPCM-based experiments	70
7.4	Split gate solar cells	72
7.5	Gate penetration depth in split gate devices	72
7.6	Undoping of P3HT by oxygen desorption	74
7.7	SPCM on split gate devices	75
8	Summary and outlook	81
	Bibliography	85

1 Introduction

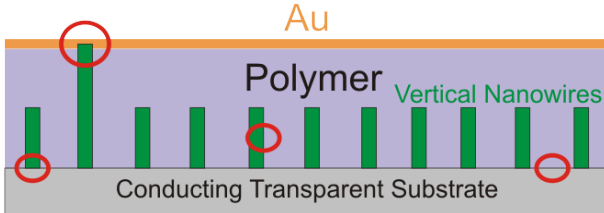
The era of modern photovoltaics started with the discovery, that semiconductors can produce currents upon illumination (1954, Bell Laboratories). Since then the basic working principle of solar cells has remained unchanged. Nowadays, the field of photovoltaics embraces a variety of different technologies and materials, whereof silicon is still the most successful one. Silicon is outstanding due to its advantageous physical properties and the vast knowledge which exists on the use of this material in information technology. To render photovoltaics more competitive to fuel-based energy sources, the efficiency (ratio of output to input energy) of solar cells has to be further improved. Thus far, especially the use of new materials like III-V semiconductors (40.8 % [1]) has enabled major efficiency enhancements.

Apart from material improvements, also optimization of the solar cell structure is important to enhance the performance. As the development of nanoscale fabrication methods progresses, solar cells with increasingly complex device designs have been realized. This allows to combine the advantageous characteristics of several materials, instead of searching for a single compound which combines all desired properties. An example is to use separate materials for light absorption and conduction. Dye-sensitized solar cells are based on this concept and attain impressive efficiencies of up to 11.2 % (see section 2.2.3). A counterexample are silicon solar cells, where all functional elements are realized by one material.

The assembly of nanostructured, three-dimensional structures made of several materials, requires novel and advanced fabrication methods. Especially bottom-up approaches are useful in this respect, as they provide the necessary building blocks as nanoparticles [2, 3], nanowires [4], or more complicated shapes like tetrapods [5] for assembly of nanostructured devices. However, the design of such solar cells poses novel challenges, in particular to identify which of the interfaces most strongly limits the photoconversion efficiency. In comparison, knowledge about the bulk material properties is only of limited value, as at microscopic scales the interfaces play a significant role. It thus becomes necessary to study and optimize single nanoscale photojunc-

tions, as a complement to the characterization of bulk solar cells.

a) Nanostructured solar cell



b) Lateral model system

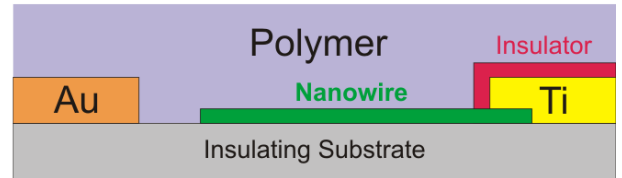


Figure 1.1: Schematic side view of a nanostructured bulk solar cell a) and the corresponding, laterally arranged model system b).

In the following, it is exemplified how such nanoscale photojunctions can be characterized. Figure 1.1.a shows a schematic drawing of a representative nanostructured solar cell [6]. The device consists of a vertical array of semiconductor nanowires grown on a conducting, transparent substrate. The nanowires are surrounded by an organic, π -conjugated polymer which makes contact to the top gold electrode. The advantages of such an architecture are detailed in section 2.2.2. There are several possible issues (marked by red circles) which can lower the device efficiency, like bad electrical contacts at the nanowire interface or shortcuts either at the bottom or top electrode. Such problems are difficult to locate in bulk solar cells as the single interfaces are not accessible. This becomes possible by a lateral model system (figure 1.1.b), which enables studying the local photoresponse of a single nanowire/polymer heterojunction. It represents the minimal working unit of nanostructured solar cells, and its optimization is essential to improve the overall performance. As the device is arranged in a lateral configuration on a surface, the individual photojunctions can be illuminated separately.

A very useful technique to address the aforementioned goals is scanning photocurrent microscopy (SPCM) whose working principle is shown in figure 1.2.a. Specifically, a focussed laser spot is scanned across the sample surface, while the reflected light and the photocurrent are recorded simultaneously, providing a reflection image and a photocurrent map of the device, respectively. By overlapping both images, the photoresponses can be correlated to the corresponding interface. An example is given in figure 1.2.b (reflection image) and 1.2.c (photocurrent map) for a graphene sheet contacted by two metal electrodes. As the photocurrent

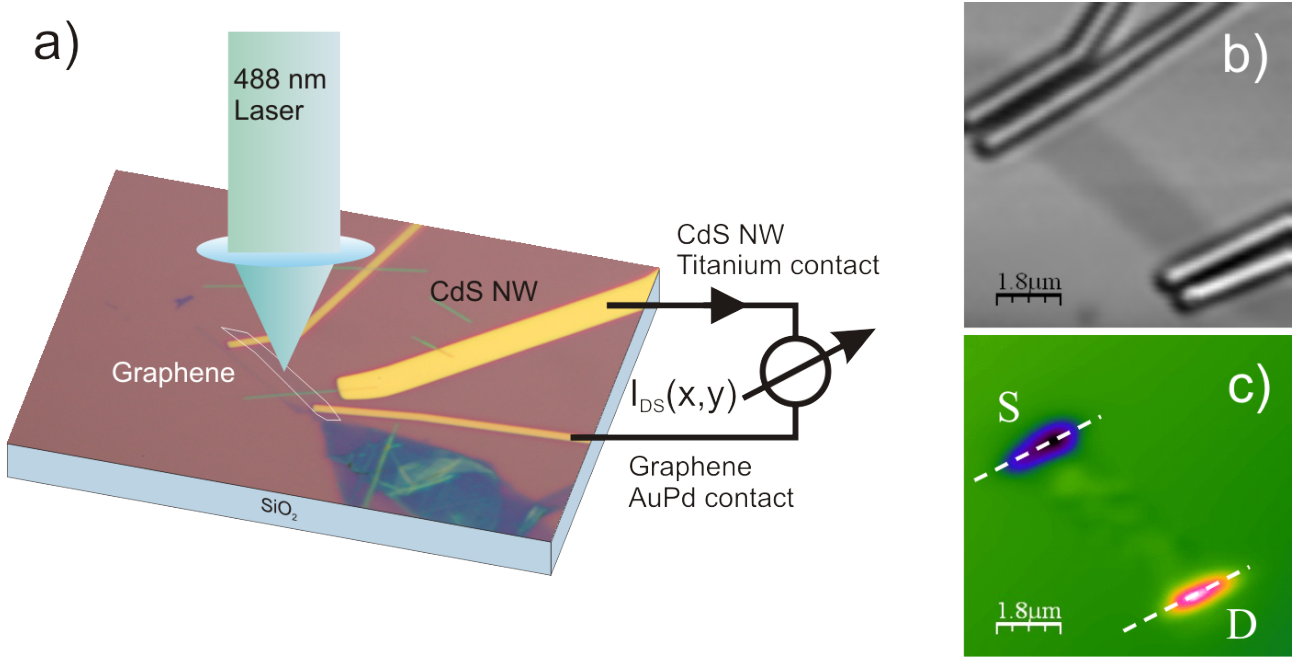


Figure 1.2: a) Schematic illustration of the principle of scanning photocurrent microscopy (SPCM). Upon scanning a focussed laser spot over a sample surface, the reflected light and the photocurrent is measured. This yields a reflection image and a photocurrent map, respectively. As an example, panel b) and c) show a reflection and a photocurrent image of a contacted graphene flake [7].

map shows, photocurrents are generated at both contacts. They can be attributed to the local band bending due to the doping by the metal electrode. The resulting built-in electric field separates excited charge carriers which then drive an electrical current. As solar cells rely on the same working principle, the investigation of nanoscale photovoltaic devices by SPCM is a powerful approach to improve nanostructured devices. The model systems are fabricated by lithography methods enabling a high degree of flexibility and control in the device design. This further allows to easily incorporate novel materials like graphene or carbon nanotubes, which have interesting properties for solar cell application. Finally, due to the lateral arrangement of the photojunctions, the photoresponses of the various interfaces can be easily distinguished, even if they have a different sign. Such information cannot be obtained from bulk solar cells.

Our approach represents an extension of previous studies based on a similar technique called laser beam-induced currents (LBIC). LBIC has been used to characterize series and shunt re-

sistances in silicon solar cells [8], to measure the lifetime degradation due to extended material defects [9, 10], or simply for quality control in production [11]. Whereas the measurement principle is similar, the use of LBIC has thus far been limited to fully assembled solar devices. Specifically, contrary to the SPCM method, it has not been used to characterize single, nanoscale photojunctions, since most LBIC setups do not achieve the necessary resolution.

This thesis is organized as follows:

Chapter 2 consists of a theoretical and an overview section. In the theoretical part the basic differential equations which are necessary to describe transport and charge carrier lifetimes in solar cells are derived. Furthermore, physical terms like efficiency, fill factor, open circuit voltage, and short circuit current are introduced using the example of a pn-junction. In the second part, this chapter gives a general overview of the most relevant types of solar cells.

Chapter 3 addresses the spatial distribution of photocurrents along cadmium sulfide nanowire Schottky-contacts. The obtained SPCM data is compared to numerical calculations of the charge transport and recombination rates in the nanowire. On this basis, it is demonstrated that charge carriers can be efficiently extracted out of such contacts.

Chapter 4 discusses the photoelectric properties of a graphene/cadmium sulfide nanowire junction. It is shown how chemical interface tailoring can efficiently improve the performance of this device.

Chapter 5 extends the experiments in the previous chapter to develop an electrical detector for surface plasmons. The polarization dependent measurements are explained with the aid of numerical solutions of the Maxwell equations.

Chapter 6 presents spatially resolved photocurrent measurements on hybrid model systems for blend and nanostructured solar cells.

Chapter 7 deals with electric field-assisted exciton dissociation in π -conjugated organic polymers, and its potential use in solar cells.

2 Fundamentals of solar cells

The operation of solar cells relies on the interplay between charge generation recombination, and associated drift- diffusion-currents. Therefore, in the following sections a basic set of differential equations is established, which fully describes charge transport in solar cells. Subsequently, the properties of pn-junctions are discussed, in order to introduce several physical parameters which are important for photovoltaics. In the second part of this chapter a general overview of current and future solar cell technologies is given. While silicon-based devices are shortly discussed, the major focus is on new materials and improved solar cell designs.

2.1 Semiconductor basics

2.1.1 Charge transport in semiconductors

Upon illumination of a semiconductor, electrons and holes are generated in equal amounts. To obtain a net current which can perform work in an external circuit, the charges must be separated and transported out of the device. Therefore, adequate forces on the charge carriers are needed to separately extract electrons and holes. The charge movements can be driven by different means. Such handles are the gradient of gravitational potential (acts on their mass), the gradient of the electrical potential (acts on their charge), the temperature gradient (changes their entropy) and the gradient of the chemical potential (influences their quantity).

Gravitational forces can be generally neglected, since they are much smaller compared to the other forces. Temperature gradients can give rise to thermal diffusion currents which is described by the Seebeck effect [12]. This effect is neglected in the following discussion, as it plays only a minor role in solar cells (although section 7.7 discusses thermoelectric currents in SPCM measurements). Most currents in solar cells are due to changes in the electrical and chemical potential. The resulting two types of currents are discussed in the following.

Gradient in the chemical potential

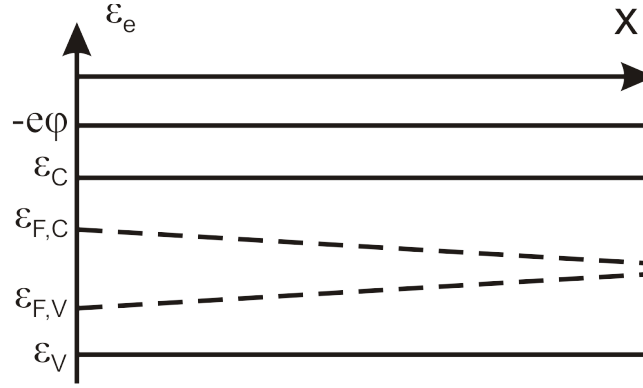


Figure 2.1: Energy diagram for constant potential energy $e\varphi$ and varying chemical potential μ_e in a semiconductor. (Adapted from P. Wuerfel [13])

The plot in figure 2.1 shows a possible arrangement of energy levels which gives rise to diffusion currents. To exclude contributions from drift currents, the electrical potential $e\varphi$ must be constant. The quasi-Fermi levels for electrons $\epsilon_{F,C}$ and for holes $\epsilon_{F,V}$ vary along the semiconductor. In this example, the charge carrier density is lower on the right side of semiconductor, such that a diffusion current will try to compensate the difference in the charge carrier density (described by the chemical potential μ). The density of electrons n as a function of μ_e is given by:

$$n = N_C \cdot \exp\left(\frac{\mu_e - \mu_{e,0}}{kT}\right) \quad \Rightarrow \quad \mu_e = \mu_{e,0} + kT \cdot \ln \frac{n}{N_C} \quad (2.1)$$

where N_C is the effective density of states, k the Boltzmann constant, and T the temperature, while $\mu_{e,0}$ is given by the electron affinity of the material $\chi = -\mu_{e,0}$. The chemical potential of holes μ_h is described by a similar equation.

The gradient of the carrier concentration leads to a diffusion current $j_{D,i}$, which is generally described by Fick's Law:

$$j_{D,i} = z_i e (-D_i \cdot \text{grad } n_i) \quad (2.2)$$

where i is the type of particle, z_i denotes the charge of a single carrier (i.e., $z_i = -1$ for electrons), D_i is the diffusion coefficient, and e the elementary charge. To express Fick's Law

as a function of the chemical potential, equation 2.2 is extended to:

$$j_{D,i} = -z_i e n_i D_i \cdot \frac{\text{grad } n_i}{n_i} \quad (2.3)$$

By replacing $(\text{grad } n_i)/n_i$ with $(\text{grad } \ln(n_i/N_i))$ and with equation 2.1, $j_{D,i}$ is obtained as:

$$j_{D,i} = -\frac{z_i e n_i D_i}{kT} \cdot \text{grad } \mu_i \quad (2.4)$$

With the Einstein relation $D_i = b_i kT/e$, where b_i is the mobility of the charge carriers, equation 2.4 can be rewritten as:

$$j_{D,i} = -z_i n_i b_i \cdot \text{grad } \mu_i = -\frac{\sigma_i}{z_i e} \cdot \text{grad } \mu_i \quad \text{with} \quad \sigma = z_i^2 e n_i b_i \quad (2.5)$$

Gradient in the electrical potential

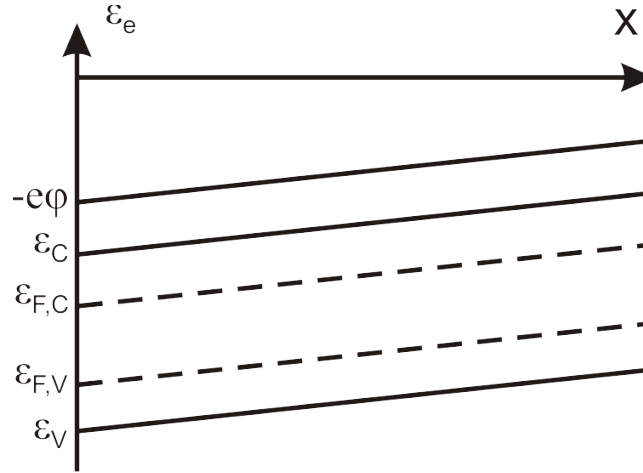


Figure 2.2: Energy diagram for varying potential energy $e\phi$ and constant chemical potential μ_e in a semiconductor. (Adapted from P. Wuerfel [13])

Figure 2.2 shows the energy diagram of a semiconductor for the case of drift current generation. Here the electrical potential varies along the semiconductor. The quasi-Fermi levels also change, but their location between the conduction (ϵ_C) and valence (ϵ_V) band remains unchanged. Thus, the charge carrier density remains constant and the diffusion current is zero.

The drift current is due to the movement of charges in the electric field. It can be calculated from:

$$j_{F,i} = z_i e n_i v_i \quad (2.6)$$

where v_i is the average velocity of the charge carriers. The charge carriers are accelerated in an electric field until they collide with an obstacle, which could be a defect, an impurity, or a phonon. The average time between two collisions is given by τ . Upon the assumption that the charge carriers completely lose their kinetic energy upon collision, the average velocity is given by:

$$v_i = z_i \frac{e}{m_i^*} \tau_i E \quad (2.7)$$

where m_i^* is the effective mass of the charge carrier, and E is the electric field. By defining the mobility $b_i = e\tau_i/m_i^*$ and with the conductivity σ_i equation 2.6 simplifies to:

$$j_{F,i} = z_i^2 e n_i b_i E = \sigma_i E \quad (2.8)$$

Finally, equation 2.8 can be rewritten as a function of the electric potential by using $E = -\text{grad } \varphi$:

$$j_{F,i} = -\frac{\sigma_i}{z_i e} \text{grad}(z_i e \varphi) \quad (2.9)$$

Total current

Above, the separate terms (equation 2.5 and 2.9) of the drift and diffusion currents were derived as a function of their corresponding potential. If both types of currents occur at the same time, they combine to a total current of:

$$j_i = j_{D,i} + j_{F,i} = -\frac{\sigma_i}{z_i e} \{ \text{grad } \mu_i + \text{grad}(z_i e \varphi) \} \quad (2.10)$$

To express drift and diffusion currents as a function of electrical and chemical potential it is useful to combine both effects in a single equation, which can be further simplified by replacing $\text{grad}(\mu_i + z_i e \varphi)$ with $\text{grad } \eta$. As a result, the current is described by the gradient of the electrochemical potential η . As the electrochemical potential relates to the quasi-Fermi levels by $\epsilon_{FC} = \eta_e$ and $\epsilon_{FV} = -\eta_h$, the total current for electrons and holes follows as:

$$j_e = \frac{\sigma_e}{e} \text{grad } \epsilon_{FC} \quad j_h = \frac{\sigma_h}{e} \text{grad } \epsilon_{FV} \quad (2.11)$$

Charge transport in semiconductors

Though the currents in a semiconductor are now available as a function of the quasi-Fermi levels, this is not yet sufficient to completely describe the operation of a solar cell. This task requires including effects like charge carrier generation/recombination and the potential distribution in the semiconductor. Charge carrier lifetimes and generation rates are described by the continuity equation:

$$\frac{dn_i}{dt} = G_i - R_i - \text{div } j_i \quad (2.12)$$

where G_i is the generation and R_i is the recombination rate. In the time-independent case ($dn/dt = 0$) and by replacing j_i with equation 2.11 one obtains:

$$\text{div } \frac{\sigma_i}{e} \text{grad } \epsilon_i = G_i - R_i \quad (2.13)$$

The electric potential in a semiconductor depends on the spatial charge carrier density distribution ρ , which is related to the electric field by the Maxwell equation:

$$\text{div } \epsilon_0 \epsilon_r E = \rho \quad (2.14)$$

Replacing E by the electrical potential yields the Poisson equation:

$$\text{div } \epsilon_0 \epsilon_r \text{grad } \varphi = -\rho \quad (2.15)$$

Finally, one obtains a set of three differential equations which fully describe charge carrier excitation, separation and extraction in a solar cell. To render them more compact, equation 2.13 and 2.15 are often written in operator form (using $\text{div } x = \nabla \cdot x$; $\text{grad } x = \nabla x$):

$$\nabla \cdot (\epsilon \nabla \varphi) = -\rho \quad (2.16)$$

$$\nabla \cdot (\mu_e n \nabla \epsilon_{FC}) = G_e - R_e \quad (2.17)$$

$$\nabla \cdot (\mu_h p \nabla \epsilon_{FV}) = G_h - R_h \quad (2.18)$$

By solving those equations, one obtains the three potentials φ , ϵ_{FC} , and ϵ_{FV} . All other parameters like current or charge carrier density can be calculated from these potentials.

2.1.2 PN-junction

A common realization of a solar cell is a pn-junction. It is described in detail in the following since it is a technologically important system and it is well suited to introduce the fundamental physical quantities of solar cells.

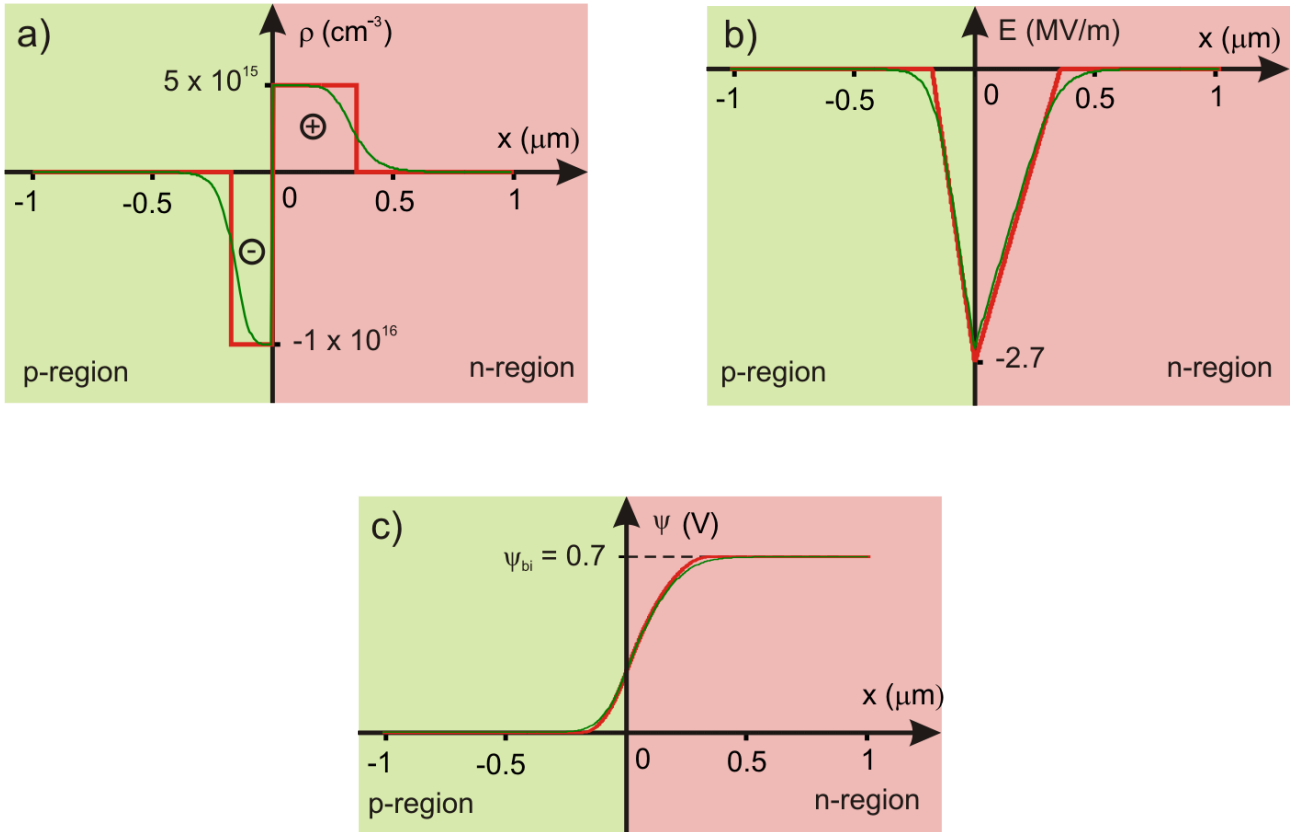


Figure 2.3: Calculated charge density ρ a), electric field E b) and potential ψ c) of a silicon pn-junction. The red curves are approximations by Schottky [14], while the green curves are the "exact" numerical solution.

A pn-junction consists of a n-doped and a p-doped region in a semiconductor. Since they are doped differently, both regions have different chemical potentials and accordingly, different Fermi levels. Upon joining them, charge carriers are exchanged until equilibrium is reached and the Fermi level is constant. Since the chemical potential far away from the junction is fixed in both regions, the Fermi level can only be kept constant by a change of the electrical

potential across the junction. As charge carriers are exchanged, a depletion zone with non-zero net charge forms around junction. Figure 2.3.a shows the net charge carrier density ρ calculated for a silicon pn-junction. The left side ($x < 0$) is p-doped with $N_A = 10^{16}$, while the right side ($x > 0$) is n-doped with $N_D = 5 \times 10^{15}$. As holes are transferred from the p- to the n-region and recombine there with the majority carriers, only the immobile, negatively charged acceptors remain. The inverse scenario holds for the donors in the n-region. As a consequence, there remains a net charge ρ at both sides of the interface, as shown by the red curve in figure 2.3.a. Since there exists no analytical solution to this problem, the charge is often approximated as being constant in the depletion zone (see [14] for the detailed mathematical description). By integrating the relation $\text{div } \epsilon E = \rho$ one obtains the electric field (figure 2.3.b) which displays a distinct maximum at the interface. Upon illumination, this electric field separates the excited electrons and holes which are then transported as majority carriers out of the solar cell. Without this field the excited charges would just recombine with the majority carriers. Finally, with $E = -\text{grad } \phi$ the electric potential can be calculated (see figure 2.3.c). There is a difference of 0.7 V across the pn-junction, which is called the built-in potential ψ_{bi} . Its magnitude depends on the doping density in both regions.

Instead of using the Schottky approximation [14], the "exact" numerical solution can be calculated by using the differential equations 2.16-2.18 derived in the previous sections. The results are shown as the green curves in figure 2.3. Although there is quite a discrepancy in the charge carrier density ρ between the two approaches, the electric field and the potential agree well.

Schottky contacts, a junction between a metal and a semiconductor, can be treated as a special case of a pn-junction. Since metals have very high charge carrier densities ($\approx 10^{23} \text{ cm}^{-3}$) compared to semiconductors ($\approx 10^{19} \text{ cm}^{-3}$) the depletion region has a significant extend in the latter case. Its extension depends on the work function of the metal and the charge carrier density in the semiconductor. Similar to a pn-junction, excited electrons and holes can be separated in the built-in electric field and thus generate a current upon illumination. However, pn-junctions are generally more efficient, since in Schottky contacts charge carriers can recombine with the metal electrode [13].

Current-voltage characteristic

Upon applying a positive bias to a pn-junction electrons (holes) are injected in the n(p)-region. As the charge carriers reach the oppositely doped region, they move as minority carriers and finally recombine. Under reverse bias, electrons (holes) are transferred out of the n(p)-region. Since no electrons (holes) can be injected in the p(n)-region from the contacts, they must have been generated inside the junction. Thus, those electrons which are thermally excited in the p-region and which reach the n-region can contribute to the reverse bias current. However, only electrons which are generated at a distance of the diffusion length L_e away from the junction can reach the n-doped region. Since the same applies to the holes, all charges contributing to the reverse saturation current are generated within the pn-junction. Thus, for example the hole current can be calculated by:

$$j_Q = -e \int_{-L_h}^{L_e} \text{div } j_h dx \quad (2.19)$$

where j_Q is the charge current coming out of the pn-junction. At $x < -L_h$ the hole current j_h is zero because of the recombination with majority electrons. However, at $x > L_e$ the hole current will be finite and constant ($j_h = j_Q/e$). The divergence of j_h is obtained from the continuity equation in the time-independent case:

$$\frac{\partial p}{\partial t} = G_h - R_h - \text{div } j_h = 0, \quad \text{div } j_h = G_h - R_h \quad (2.20)$$

The generation rate can be split up in thermally excited charge carriers (G_h^0) and a contribution due to illumination (ΔG_h):

$$G_h = G_h^0 + \Delta G_h \quad (2.21)$$

The recombination rate R_h is given by:

$$R_h = R_h^0 \frac{n \cdot p}{n_i^2} \quad (2.22)$$

where n_i is the intrinsic carrier density [14], corresponding to a semiconductor in the dark without any bias. The electron and hole concentration are related by the law of mass action $n_0 \cdot p_0 = n_i^2$, where n_0 and p_0 are the intrinsic electron and hole concentration. Under non-equilibrium the law of mass action can be extended to:

$$n \cdot p = n_i^2 \exp\left(\frac{\eta_e + \eta_h}{kT}\right) \quad (2.23)$$

Thus equation 2.22 can be rewritten as:

$$R_h = R_h^0 \exp\left(\frac{\eta_e + \eta_h}{kT}\right) \quad (2.24)$$

Under equilibrium ($\eta_e + \eta_h = 0$), G_h^0 must be equal to R_h^0 . Therefore the integral 2.19 takes the form:

$$j_Q = -e \int_{-L_h}^{L_e} \left\{ G_h^0 \left[1 - \exp\left(\frac{\eta_e + \eta_h}{kT}\right) \right] + \Delta G_h \right\} dx \quad (2.25)$$

If the conductivity of the material is high enough, η_e and η_h can be assumed to be constant between $-L_h < x < L_e$ [13]. Upon application of a bias V it follows that $\eta_e + \eta_h = eV$. Thus the integral 2.25 can be solved to:

$$j_Q = eG_h^0(L_e + L_h) \left[\exp\left(\frac{eV}{kT}\right) - 1 \right] - e \int_{-L_h}^{L_e} \Delta G_h dx \quad (2.26)$$

By setting $V = 0$ the short circuit current j_{sc} is defined as:

$$j_{sc} = -e \int_{-L_h}^{L_e} \Delta G_h dx \quad (2.27)$$

In the dark ($\Delta G_h = 0$) and at high negative bias, the reverse saturation current j_s is given by:

$$j_s = eG_{e,h}^0(L_e + L_h) \quad (2.28)$$

Thus the integrated term (equation 2.26) for j_Q can be rewritten as:

$$j_Q = j_s \left[\exp\left(\frac{eV}{kT}\right) - 1 \right] + j_{sc} \quad (2.29)$$

Furthermore, by fixing j_Q to zero, the open circuit voltage V_{oc} of the pn-junction is obtained as:

$$V_{oc} = \frac{kT}{e} \ln \left(1 - \frac{j_{sc}}{j_s} \right) \quad (2.30)$$

For a more detailed discussion of semiconductor transport and pn-junctions see [13, 14].

2.1.3 Photoconversion efficiency

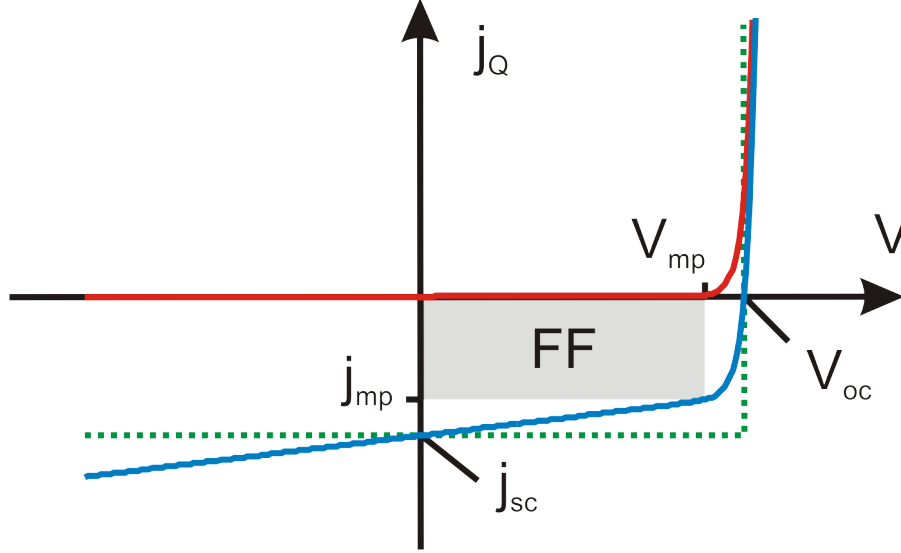


Figure 2.4: Current-voltage characteristic of a pn-junction in the dark (red curve) und under illumination (blue curve).

The efficiency η is the central figure of merit to asses the solar cell performance. To obtain the highest efficiency the solar cell has to be operated at the maximum power point (MPP). If we assume a solar cell with a perfect rectangular current-voltage characteristic, the maximum output power would be the product of j_{sc} and V_{oc} , as indicated by the green curve in figure 2.4. As discussed above, current-voltage curves show an exponential behaviour (as shown by the blue curve), and their MPP is shifted to V_{mp} and j_{mp} . The relation between the product of $j_{mp} \cdot V_{mp}$ and $j_{sc} \cdot V_{oc}$ is the fill-factor FF :

$$FF = \frac{j_{mp} V_{mp}}{j_{sc} V_{oc}} \quad (2.31)$$

Geometrically the FF corresponds to the area below the IV-curve limited by j_{mp} and V_{mp} as depicted by the gray area in figure 2.4. Since the efficiency is the ratio of output to input power, it can be written as:

$$\eta = \frac{V_{oc} \cdot j_{sc} \cdot FF}{I_{in}} \quad (2.32)$$

where I_{in} is the illumination intensity of the incident light. By the set of values V_{oc} , I_{sc} , FF , and η the major electrical properties of a solar cell are described. They are not specific to any

technology, nor the type of solar cell, and hence very useful for comparative purposes.

2.2 Novel materials for solar cells

To achieve maximum efficiency of a solar cell, its design has to be adapted to the physical properties of the absorber layer. Especially the combined requirements of strong light absorption and efficient charge transport govern the design of photovoltaics. A thoroughly studied example are solar cells made of silicon, which (still) is the most widespread material used for photovoltaics. It offers several advantages, specifically (I) it is an earth abundant element, which is necessary for cheap production; (II) it is non-toxic; (III) it is stable under ambient due to the formation of a layer of SiO_2 on the surface (no extensive sealing of the solar cells is necessary), and (IV) it has a bandgap of $E_G = 1.12$ eV which, according to Shockley and Queisser [15], is close-to ideal to achieve the maximum theoretical efficiency of 30 % for a single junction.

However, silicon also has a very significant disadvantage, most prominently its indirect bandgap, which leads to low light absorption ($\alpha \approx 10^4 \text{ cm}^{-1}$ [16]). Hence, to absorb most of the incident light, single crystalline silicon solar cells must be very thick, up to $200 \mu\text{m}$. Upon optical excitation, either electrons or holes have to diffuse long distances as minority carriers through the solar cell. Therefore, the silicon must be of high quality, as otherwise most charge carriers would be lost due to recombination at defects or impurities. The production of such high grade silicon is a well-controlled but extensive process.

In order to outperform silicon, novel materials must have direct bandgaps and high optical absorption coefficients. This enables thinner solar cells, since less material is needed to absorb the same amount of incident light. As the thickness decreases, also the necessary minimum diffusion length becomes smaller and the material quality is less critical. This allows for the use of polycrystalline materials, which have higher defect concentrations and lower mobilities than silicon. Numerous types of materials are routinely used in such thin-film solar cells, including binary (CdS/CdTe [17, 18]) or ternary (Cu(In,Ga)Se₂ [19, 20], HgCdTe [21]) semiconductors, or even amorphous silicon (a-Si) [22].

While the aforementioned solar cells are already commercially available, the following section provides a short overview of three innovative types of solar cell materials that are still under development.

2.2.1 Organic bulk-heterojunction solar cells

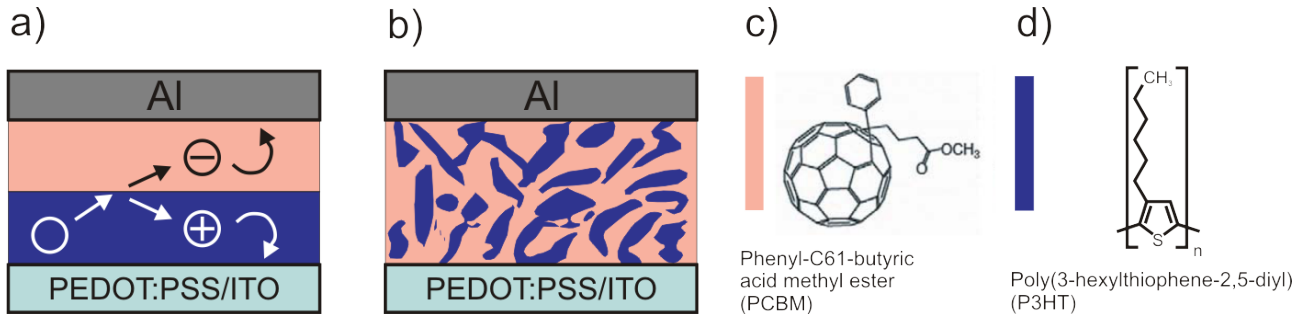


Figure 2.5: a) Planar- and b) bulk-heterojunction solar cell made of an c) organic acceptor (PCBM) and d) donator (P3HT) material.

The first studies on organic semiconductors date back to the 1940s [23]. In the beginning, this topic received only limited attention due to the low mobility of the available organic materials. The situation changed due to the steady increase in mobility which allowed to use these materials in field-effect transistors (FETS) [24], light emitting diodes [25, 26] and solar cells [27]. Nowadays, semiconducting polymers like Poly(3-hexylthiophene) (P3HT) attain hole mobilities of $\mu_h \approx 0.1 \text{ cm}^2/\text{Vs}$ [28]. This is comparable to α -Si, albeit much lower than crystalline silicon ($\approx 1000 \text{ cm}^2/\text{Vs}$). While in inorganic materials adjacent atoms are strongly bound, in organic materials the molecular building blocks are only weakly coupled by van der Waals forces. Thus, there is little overlap between neighboring wavefunctions, leading to narrow bands with large effective masses. As a consequence, mobilities in organic materials are generally lower than in inorganics.

However, compared to silicon the optical absorption of organic materials ($\alpha_{\text{P3HT}} \approx 10^5 \text{ cm}^{-1}$) is higher such that films of only $1 \mu\text{m}$ thickness can absorb most of the incident light. Further advantages of the latter include the low processing temperature, which allows to use flexible substrates. Furthermore, organic materials can often be modified, for example by attaching different substituents, which gives a lot of possibilities for optimizations. One drawback is that organics are often susceptible to oxygen or other adsorbates, which requires encapsulation for stabilization. The major drawback of organic materials is however their short exciton diffusion length.

Exciton diffusion length

In contrast to inorganic semiconductors, excitons in organic materials have high binding energies (several 0.1 eV) [13]. Accordingly these excitons easily recombine and the separation in free charge carriers is a rare process. To efficiently dissociate excitons, acceptor materials with high electron affinities are used (the exciton dissociation process is described in greater detail in section 7.2). An example for such acceptors is phenyl-C61-butyric acid methyl ester (PCBM). Upon illumination, the electrons are transferred to the PCBM acceptor while the holes remain in the P3HT, as illustrated by figure 2.5.a. The major limitation is the short exciton diffusion length ($L_{EX} = 5 - 10$ nm), since the absorption length ($1/\alpha$) is 10-100 times larger. Thus, in a planar solar cell structure as depicted in figure 2.5.a, only excitons excited in a small region around the heterojunction can contribute to the photocurrent.

L_{EX} is so small due to energy relaxation along the diffusion path. Excitons are transferred by dipole coupling between adjacent polymer chains, which is called Föster resonance energy transfer (FRET). This process works only over very short distances due to its fast spatial decay (r^{-6}). As there is disorder in the polymer chains, the exciton energies vary. Once an exciton is transferred to a polymer chain at lower energy, its excess energy relaxes and it cannot be transferred back. Thus, upon every energy transfer the number of possible transfer sites decreases, which limits the total diffusion length. As a consequence, systems with high disorder have only short exciton diffusion lengths. For example excitons in poly-phenylenevinylene (PhPPV) films have been shown to perform on average only four jumps between polymer chains [29]. By comparison, in highly ordered arrangements of small molecules like rubrene exciton diffusion length up to 8 μm have been measured [30].

Bulk heterojunction devices

Nevertheless it is possible to build efficient solar cells using organic polymers. The most successful strategy to compensate for the short exciton diffusion length are bulk heterojunction devices, as depicted in figure 2.5.b. To enhance the interfacial area, acceptor and donor material are mixed and deposited together on a conducting substrate. The domains of both materials should ideally be of the size of the exciton diffusion length, such that every excited exciton can reach a heterojunction and the separated charges are transported out of the solar cell over a percolation network. Obtaining such small domains requires a certain control over the morphol-

ogy of the donor and acceptor phase. This can be achieved by suitable material combinations. Efficient combinations are for example PPV/PCBM ($\eta = 4-5\%$ [31]), P3HT/PCBM ($\eta = 6\%$ [32]), or PTB7/PB₇₁BM ($\eta = 7.4\%$ [33]). Another possibility is to exchange the solvent [32]. As most films are spin coated, solvents with a low vapour pressure evaporate slower and leave the polymer more time to crystallize. A similar effect is obtained by short heat treatments [34]. Upon heating the film close to the glass transition temperature defects are cured and the crystallinity increases.

The major obstacle to increasing the efficiency of bulk-heterojunction solar cells is the large bandgap of the semiconductors (P3HT: $E_g = 1.9\text{ eV}$) which filter out a significant amount of the solar spectrum. Another problem is the charge transport along the percolation network. As it is apparent from figure 2.5.b, some domains are isolated or short-circuited with the wrong electrode. To reduce this problem, the device thickness can be decreased and more charge carriers will reach the electrodes. However, as the thickness decreases less light is absorbed, which in turn lowers again the efficiency.

2.2.2 Hybrid solar cells

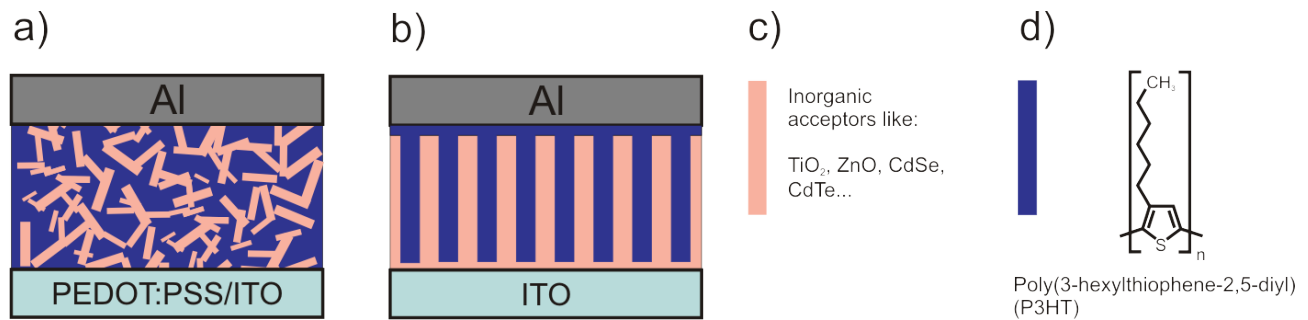


Figure 2.6: Hybrid solar cells consisting of a) a blend of an inorganic acceptor and an organic donor. b) Vertical arrays of an c) inorganic acceptor interpenetrated by an d) organic donor.

In hybrid solar cells the acceptor is typically replaced by an inorganic material which receives electrons from the organic donor. Upon exciton dissociation at the donor/acceptor interface, the hole remains in the organic material, while the electron is transferred into the quencher.

Often used as inorganic acceptors are ZnO, TiO₂, CdS, or CdSe. The simplest hybrid solar cell consist of a blend of inorganic semiconductor nanoparticles and an organic polymer (see figure 2.6.a). Despite their simple fabrication, these solar cells reach efficiencies of up to 1.7 % [35].

As for bulk-heterojunction devices, the charges are transported along a percolation network out of the solar cell. An advantage of inorganic materials is that they offer additional ways to influence the blend morphology. Charge carriers have to tunnel thermally assisted along the nanoparticle network, which is described as hopping transport. To minimize the hopping steps, instead of nanoparticles, nanorods or even more complicated structures like tetrapods have been used. In figure 2.7, the morphology of films blended with CdSe nanoparticles (7x7 nm) and nanorods (7x60 nm) are compared. Panels a & b show top- and c & d side-view scanning electron microscopy images (SEM). For the same content of inorganic material (20 wt%), a more evenly distributed network and correspondingly a better conductivity is obtained in the case of nanorods.

Nanoparticles are often coated by ligands during synthesis, which helps to control their growth and to keep them suspended in solution. As these ligands determine the interparticle distance they affect the tunneling probability. To improve the conductivity they can be exchanged by shorter ligands. There are several chemical treatments to achieve this, which at the same time passivate defects at the surface to further enhance the conductivity [36] (see section 6.3 for more details). Despite such treatments, charge transport remains an issue in these solar cells. The next section describes an approach which could reduce this problem.

Nanostructured vertical arrays

A further possibility to improve the transport in hybrid solar cells is depicted in figure 2.6.b. Instead of forming a blend, the inorganic acceptor material is structured to arrays of vertical nanowires. In a second step, the voids between the nanowires are filled up with an organic acceptor. This design has the advantage that there are separate, defined pathways for electron and hole transport without any need of tunneling. In such a solar cell there are no isolated or shorted domains.

However, solar cells of such ideal structure are difficult to fabricate. The spacing between the nanowires should be of the order of the exciton diffusion length (≈ 10 nm), while the nanowires

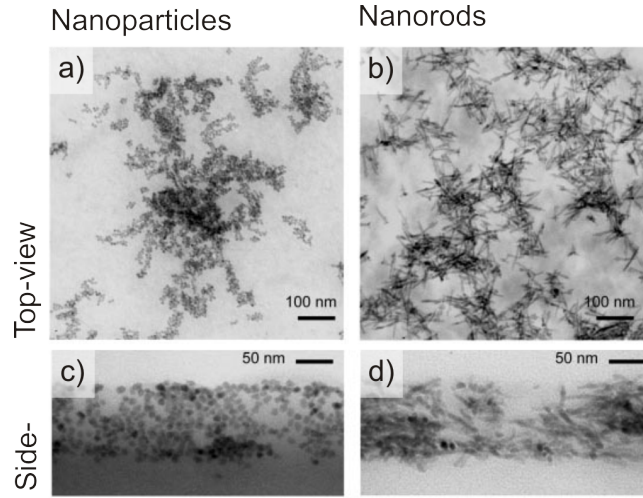


Figure 2.7: Top- (a & b) and side-view (c & d) of inorganic/polymer blends, made of P3HT and CdSe nanoparticles (a & c) or nanorods (b & d) [35].

should be as thin as possible. At the same time they should have a length of above 300-500 nm to avoid optical interference effects, so that most of the incoming light can be absorbed [37]. To realize such structures, both bottom-up and top-down [38] methods have been employed [39, 40, 6].

After the structuring of the inorganic acceptor, the voids have to be filled by an organic donor. If the voids are very small this becomes difficult. Possible approaches are *in situ* polymerization [41] or melting of the polymer [42].

2.2.3 Dye-sensitized solar cells

Figure 2.8.a shows a dye-sensitized solar cell (DSSC) where incident light is absorbed by a molecular dye layer (for example a ruthenium dye [44]). The dyes are adsorbed as a monolayer on a metal oxide film (most often TiO_2). Upon illumination the dye is excited and the electron is transferred to the TiO_2 (see figure 2.8). The photo-oxidized dye is reduced by an electrolyte containing a redox couple, like iodide/triiodide (I^-/I_3^-). At the counter electrode the triiodide is in turn reduced to iodide. To enhance this reaction the conducting glass substrate is covered with a platinum catalyst. A dye monolayer only absorbs a small amount of light. Therefore, to increase the surface, the TiO_2 electrode has a mesoscopic structure consisting of sintered nanoparticles (attaining a surface of $135 \text{ m}^2/\text{gr}$ [45]). Due to the structure of the electrode,

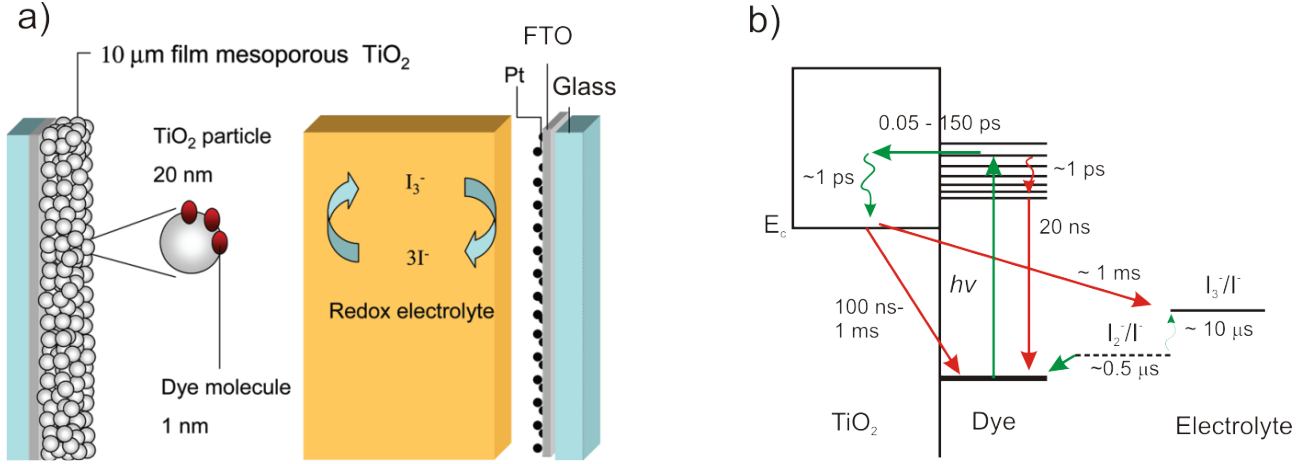


Figure 2.8: a) Schematic drawing and b) energy diagram of a dye-sensitized solar cell. Panel b) shows the forward and backward charge transfer setups with their respective time scales. (Adapted from [43])

dye-sensitized solar cells efficiently absorb diffuse light, while silicon solar cells for example work ideal only if the incident light is perpendicular to their surface.

A major reason why dye-sensitized solar cells attain impressive efficiencies of up to 11.2 % [46] is their nearly ideal alignment of energy levels, as shown in figure 2.8.b. Upon excitation of the dye, a hole cannot enter the TiO_2 electrode, due to the deep lying valence band. At the same time the electron cannot be transferred to the electrolyte, as there is no electronic state available. Thus the absorber layer (the dye) is surrounded by two layers which are only permeable for one charge carrier type. Such an architecture is considered to be ideal to minimize losses due to recombination and could even outperform pn-junction devices [13].

However there exists a significant recombination path, as indicated in figure 2.8.b. Electrons passing through the TiO_2 electrode can also reduce photo-oxidized dye molecules. This process is favourable due to the high surface of the electrode and occurs mainly under intense illumination. A solution of this problem might be the use of nanostructured DSSCs as described by Liu et al. [47]. In this work, vertical arrays of highly conductive carbon nanotubes (CNT) coated with TiO_2 serve as electrodes in DSSCs. Instead of sintered TiO_2 electrodes which have low electron mobilities, the improved transport along CNTs should yield lower recombination losses.

Intense scientific efforts were made to optimize the chemical structure of the dyes, including metal complex, indoline, or polyene dyes [48]. To achieve a very fast electron transfer to the electrode, the dyes are optimized to match the energy levels of TiO_2 (see figure 2.8.b). As a consequence the electrons are removed much quicker than any oxidation process could take place, which renders the dyes remarkably stable on the electrode. A stability issue, however, is the back electrode. Due to the harsh electrolyte environment, even the platinum catalyst is dissolved in the electrolyte over time. Therefore, many efforts are made to find alternative, more suitable redox couples and to replace the fluid electrolyte by a solid-state conductor. Moreover, the dyes have to be further optimized to match a broader part of the solar spectrum.

2.2.4 Plasmon enhancement

The design of solar cells is in many cases a tradeoff between device thickness and transport. If the thickness is increased more light is absorbed, but the charge transport out of the solar cell becomes more difficult. This conflict is usually resolved by improving the transport (like in nanostructured solar cells). In this section, an alternative approach is presented.

Instead of attaining a high absorption by adjusting the solar cell thickness, additional light coupling elements are introduced. As figure 2.9 shows there are mainly three different approaches to concentrate the incident light inside the solar cell. Firstly, metallic particles can be used to scatter light into the solar cell (see figure 2.9.a). Normally light is scattered to the same extend back and forth. However, metal particles at the interface between two dielectrics will predominantly scatter the light into the material of higher permittivity [49]. As Catchpole et al. [50] demonstrated, the coupling efficiency depends on the shape of the particles, with hemispheres providing the best results. Such particles increase the optical path length in the solar cell by a factor of 17. By using dielectric coatings the light scattering cross-section can be further improved [51], such that a 10 % coverage of nanoparticles would be sufficient to fully scatter the incident power. It is noteworthy that the reflection at the back electrode further confines the light in the solar cell.

A second approach is to bring metal nanoparticles close to the photoactive junction of the solar cell (see figure 2.9.b). Metallic particles with sizes of a few tens of nanometers show resonant plasmon excitations, which lead to strong local field enhancements around the particle. In this

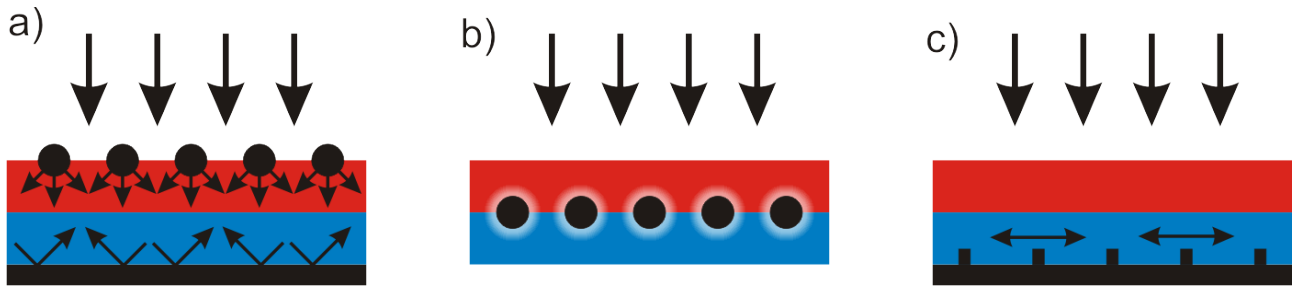


Figure 2.9: Concepts to improve light absorption in thin film solar cells. The interface between red and blue regions represents the photoactive junction. a) Metal particles at the surface scatter the light into the solar cell. b) Upon photoexcitation of plasmonic resonances in metallic particles, their optical near field increases in the area of the junction. c) A structured back electrode is used to launch surface plasmons along the horizontal direction, thus increasing the optical path length in the solar cell. (Adapted from [52])

manner, light intensity can be concentrated in the photoactive area, with the particles acting as antennas. This effect is useful to focus the light to the interfaces in bulk heterojunction solar cells, where exciton diffusion lengths are short. However, the particles need to be coated with an insulating layer to avoid recombination or exciton quenching.

A third approach, which is easy to integrate in most solar cells is to structure the back electrode of the solar cell (see figure 2.9.c). Upon illumination, surface plasmons are excited which propagate along the metal surface. Thus the vertical incident light is turned by 90° into a plasmonic mode that propagates in horizontal direction through the solar cell. This increases the light path and works especially well in the infrared where the propagation length of surface plasmons is large (10 - 100 μm).

3 Cadmium sulfide nanowire Schottky-contacts

Semiconductor nanowires (NWs) are versatile components of optoelectronic devices like solar cells [53] and photodetectors [54]. Owing to their high density of surface states, such wires can have a higher sensitivity to light than the corresponding bulk material [55, 56, 57]. As was already discussed in section 2.2.2 they are promising building blocks of novel nanostructured solar cells [58, 59]. To use nanowires effectively good contacts are necessary, which are often difficult to achieve due to the small and thus sensitive contact area. Depending on the type of application, either ohmic- or Schottky-contacts are preferred. Photodetectors for example commonly comprise Schottky-type contacts because of their fast response time of 10 ps which originates from the strong built-in electric fields [60]. In solar cells, by contrast, Schottky-contacts are often avoided, as recombination with the metal electrode leads to higher losses than in pn- or hetero-junctions (see section 2.1.2).

3.1 Photoresponse distribution

In this chapter, we show that very efficient charge separation is possible at nanowire Schottky-contacts. To this end, the photocurrent response of a gold-covered cadmium sulfide nanowire is measured by SPCM. In the investigated devices diffusion currents can be effectively separated from the drift contribution, thus enabling reliable measurements of the electron diffusion length in the nanowires. This in turn yields the electron recombination rate at the metal contact, a quantity which otherwise is only indirectly accessible, for example from the ideality factor of diode-type I/V-curves [61]. It is demonstrated that the recombination rate is close to zero over a few micrometer along the Schottky-contact.

Experimental details

The CdS NWs were synthesized by a solvothermal method using cadmium diethyldithiocarbamate $[\text{Cd}(\text{S}_2\text{CN}(\text{CH}_2\text{CH}_3)_2)_2]$ as precursor and ethylenediamine $\text{H}_2\text{N}-\text{CH}_2-\text{CH}_2-\text{NH}_2$ as coordinating solvent [62]. After 48 h of growth at 200°C , single-crystalline CdS wires with lengths of up to $20\text{ }\mu\text{m}$ and diameters in the range of 20 to 80 nm were obtained. The wires were dispersed in ethanol with the aid of ultrasonication.

In order to obtain stable and reproducible photocurrent responses in the contact regions, it proved essential to remove the oxide from the nanowire surface. This was achieved by dispersing the wires in an aqueous HCl solution (pH 2) for 15 minutes at room temperature. Subsequently, the wire surface was passivated by attachment of an organic thiol layer (immersion in a $70\text{ }\mu\text{mL/mL}$ solution in ethanol for 48 h under ambient conditions, followed by three washing steps using pure ethanol). While we did not systematically study the suitability of different types of thiols, we obtained reproducible results with heptadecafluoro-1-decanethiol (Sigma-Aldrich) as ligand. All samples described in the following comprised CdS NWs capped with this thiol.

The surface-functionalized nanowires were deposited by spin coating ($20\text{ }\mu\text{L}$ droplet at 5000 rpm) from dispersion in ethanol onto a highly doped silicon substrate covered with a 300 nm thick layer of thermal SiO_2 . Subsequently, individual NWs were provided first with a gold contact extending over several micrometers on top of the wire. For this purpose, e-beam lithography was used followed by thermal evaporation of 80 nm of gold. The sample was then annealed at 350°C for 15 min in argon atmosphere to improve the contact. Due to the high work function of the gold, a Schottky-like contact is formed at this electrode [63]. Finally, a second contact made of titanium was defined at a separation of $5\text{ }\mu\text{m}$ from the edge of the gold contact. Before evaporation of 80 nm titanium, the sample was subjected to argon plasma ($P = 200\text{ W}$, $p = 0.3\text{ Torr}$, $t = 2\text{ min}$) in order to locally n-dope the contact area [64] and thereby ensure an Ohmic contact [65]. The SPCM studies were performed under ambient conditions using a laser wavelength of 488 nm, a 50x objective ($\text{NA}=0.8$) and a light intensity of 190 kW cm^{-2} .

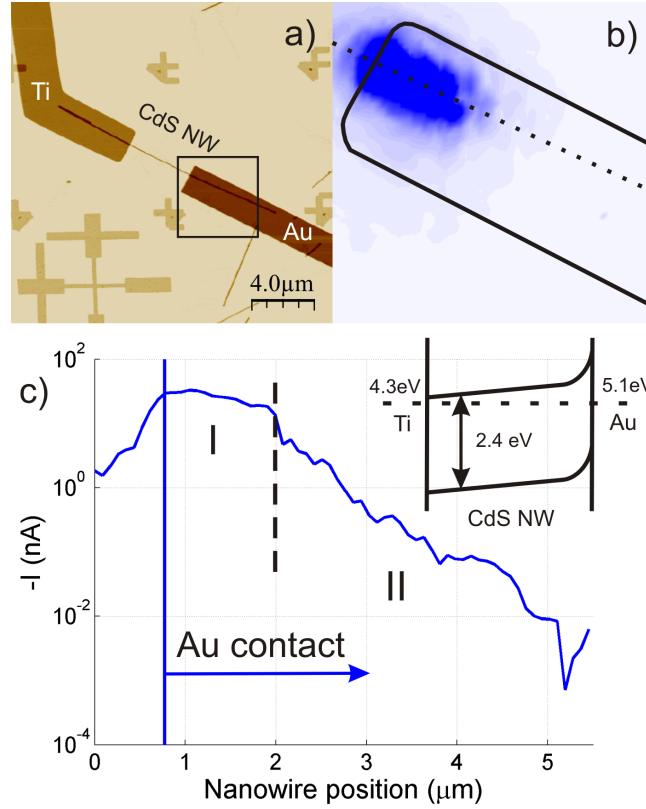


Figure 3.1: a) AFM image of a CdS nanowire contacted by a gold and titanium electrode. The black rectangle marks the position of the photocurrent map in panel b). c) Photocurrent profile along the dotted line in panel b). The inset depicts the energy band diagram of the nanowire with a titanium and gold contact under short circuit condition. The numbers indicate the respective work functions of the two metals.

Photocurrent response

Figure 3.1.a shows an AFM-image of the completed CdS NW device. The combination of an Ohmic and a Schottky-type contact on the wires resulted in a pronounced photoresponse located around the edge of the gold contact, as exemplified by the photocurrent map in figure 3.1.b. Similar behaviour has been reported for different other nanowires [66, 67]. While previous works have focused on the signal along the bare NW section, here we address the photoresponse along the Schottky-contact between the gold layer and the underlying wire segment. Like for the bare wire section, this response originates from the separation of photoexcited electron-hole pairs in the CdS NW by the electric field of the Schottky-contact. While the holes are transferred into the gold electrode, the internal field drives the electrons along the NW to the titanium

Parameter	Value	Parameter	Value
Bandgap	2.482 eV [68]	Electron mobility	300 cm ² /Vs [65, 69]
Effective density of states	2.4×10^{18} eV [70]	Hole mobility	50 cm ² /Vs [65, 69]
Electron affinity	3.7 eV [71]	Dielectric constant	8.73 [68]

Table 3.1: Material constants of cadmium sulfide used for the FEM calculations.

contact. In the corresponding photocurrent profile in figure 3.1.c (taken along the dotted line in figure 3.1.b) two different regimes can be distinguished, specifically region I wherein the current remains almost constant over approximately 1 μm from the electrode edge, and region II displaying an exponential current decrease, detectable up to 5 μm into the contact region.

3.2 Calculated electric potential along a nanowire/metal contact

To further analyze the photocurrent profiles, we performed two-dimensional finite element (FEM) calculations. For this purpose, we solved the set of differential equations 2.16-2.18 derived in section 2.1.1 with the open-source package PoissonNL. The material constants used for the calculation are summarized in table 3.1. Figure 3.2.a shows a schematic drawing of the simulated mesh representing the CdS/Au contact. In figure 3.2.b, the calculated electric potential map is depicted for the device under open circuit condition. The titanium electrode is defined as source at 0 V, which places the gold electrode at a potential of -0.6 V as a result of the Schottky contact formation [63], leading to a corresponding potential gradient along the nanowire. The electric field distribution calculated using the relation $\vec{E} = -\vec{\nabla}V$ in the x- and y- direction within the CdS NW is illustrated by figure 3.2.c and 3.2.d, respectively. The white arrows in the colour maps indicate the direction of the electric field-induced forces on electrons, according to the relation $\vec{F} = -q\vec{E}$ with the positive elementary charge q .

The maximum of the E_x component (1 MV/m) is located just outside of the metal contact (figure 3.2.e). Photo-excited electrons in the NW are moved by the E_x field in axial direction towards the titanium contact. As the electrical field also extends below the electrode, electrons at this location are pushed out of the contact. The exponential decay of the E_x component below the electrode is largely independent of an applied bias. Even if bias is applied, the potential along the gold electrode remains constant and with it the axial electric field distribution

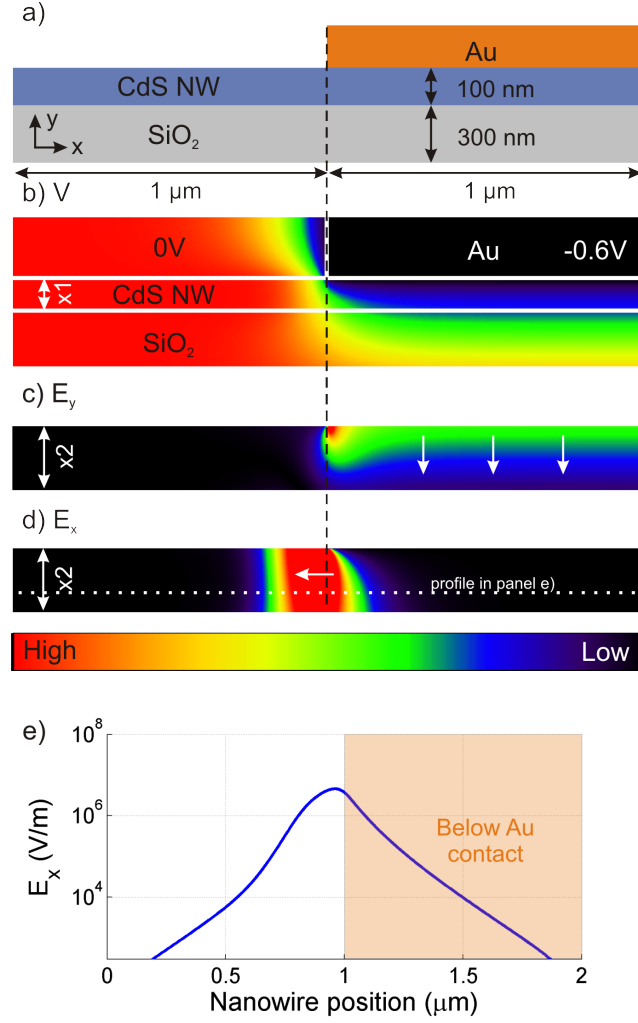


Figure 3.2: Result of a two-dimensional FEM calculation of photocurrents generated at the Au/CdS nanowire contact. a) Schematic representation of the simulation space with the relevant dimensions. b) Calculated electric potential distribution plotted as a colour map. c), d) The calculated y- and x-component of the electric field, respectively. For clearer graphical representation, the maps were vertically stretched. The white arrows indicate the force direction acting on electrons in the nanowire. e) Semi-logarithmic plot of the E_x component along the bare and gold-coated wire, corresponding to a profile taken along the dotted line in panel d.

(see figure 3.3.a).

The E_y component assumes a similarly strong magnitude (1 MV/m), pushing the electrons towards the CdS/SiO₂ interface and thus hindering the electrons to recombine with the gold

electrode. Without this field acting in radial direction of the NW, the probability of electron recombination with the surrounding metal would be very high and correspondingly no photocurrent could be detected below the contact. In the following, the radial and axial electric fields will be utilized to simulate the photoresponse below the gold contact and thereby to determine the electron recombination rates.

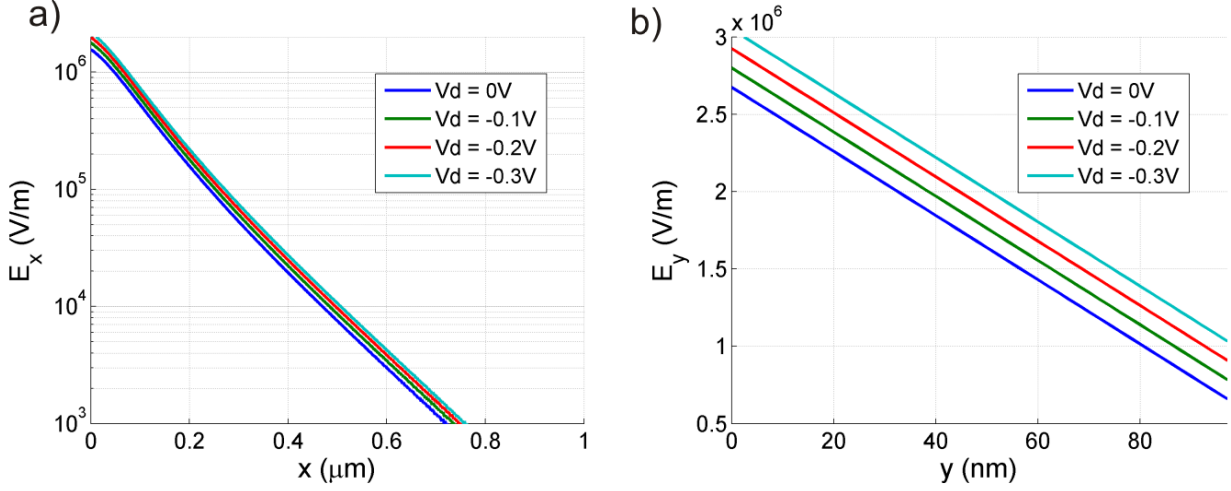


Figure 3.3: Electric field profiles in a) x- and b) y-direction, extracted from the FEM calculations, at difference bias voltages V_d .

3.3 Drift- and diffusion-currents

Modelling the photocurrent along the NW requires solving the continuity equation under illumination. To this end, it is assumed that whenever an electron-hole pair is excited, the hole is directly transferred into the gold. Due to the above mentioned electron accumulation at the CdS/SiO₂ interface, the problem can be reduced to one dimension (see figure 3.4). The time independent continuity equation is then given by:

$$\frac{dn_e(x)}{dt} = G_e - R_e - \text{div } j_e = 0 \quad (3.1)$$

where $n_e(x)$ is the electron excess charge, and j_e is the electron current density, while G_e and R_e are the electron generation and recombination rate, respectively. Their difference gives the position dependent recombination rate of excess electrons:

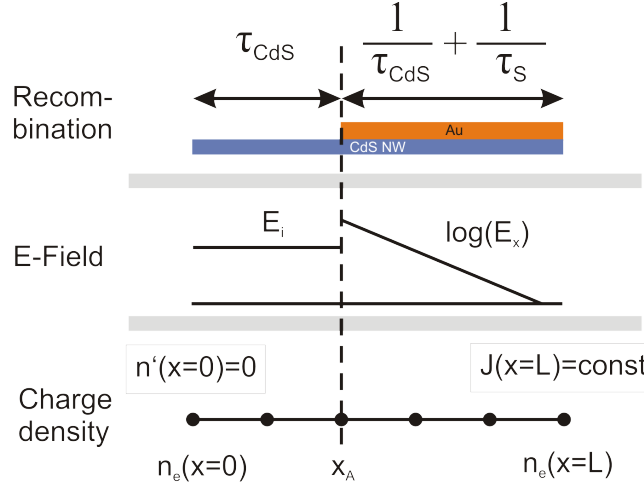


Figure 3.4: Schematic representation of the boundary conditions, the E-Field distribution, as well the recombination rates used for solving the drift and diffusion equation in one dimension.

$$G_e - R_e = -\frac{n_e(x)}{\tau} \quad (3.2)$$

where τ is the electron lifetime. On this basis, the current density j_e is obtained as the sum of the diffusion- and drift-current:

$$j_e = -D_e \frac{dn_e(x)}{dx} + n_e(x)b_e E(x) \quad (3.3)$$

where D_e is the diffusion coefficient (given by the Einstein relation $D_e = b_e kT/q$). To solve equation 3.1 the electric field, the electron lifetime and the boundary conditions have to be specified (see figure 3.4). For the electric field, the distribution gained by the FEM calculation (figure 3.2.e) can be used. The position of maximal electric field is denoted by x_A corresponding to the edge of gold contact. As the SPCM measurements are performed under short circuit condition of the device, with both electrodes forced to the same potential (compare inset figure 3.1.c), a constant internal field occurs along the nanowire. For a Schottky barrier height of 0.6 V and a distance between the contacts of 5 μm , the internal field is estimated to be $E_i = 1.2 \times 10^5$ V/m. As discussed further below, the field magnitude is important to account for the bias dependence of the measured photocurrent profiles. The recombination rate ($1/\tau$) along the bare wire is determined by the electron lifetime $\tau = \tau_{CdS}$ of pristine CdS [65], whereas in the gold-coated segment the electron lifetime will be reduced according to:

$$\frac{1}{\tau} = \frac{1}{\tau_{CdS}} + \frac{1}{\tau_S} \quad (3.4)$$

where τ_S accounts for an increased recombination of electrons with the near metal surface of the gold contact. By choosing an appropriate boundary condition at the right border of the simulation space (Figure 3.4, $x = L$) the injection of excess electrons (via laser illumination) is implemented (see below for more details). The second boundary condition $n'_e(x = 0) = 0$ fixes the diffusion current at $x = 0$ to zero, ensuring a minimal error in the simulation.

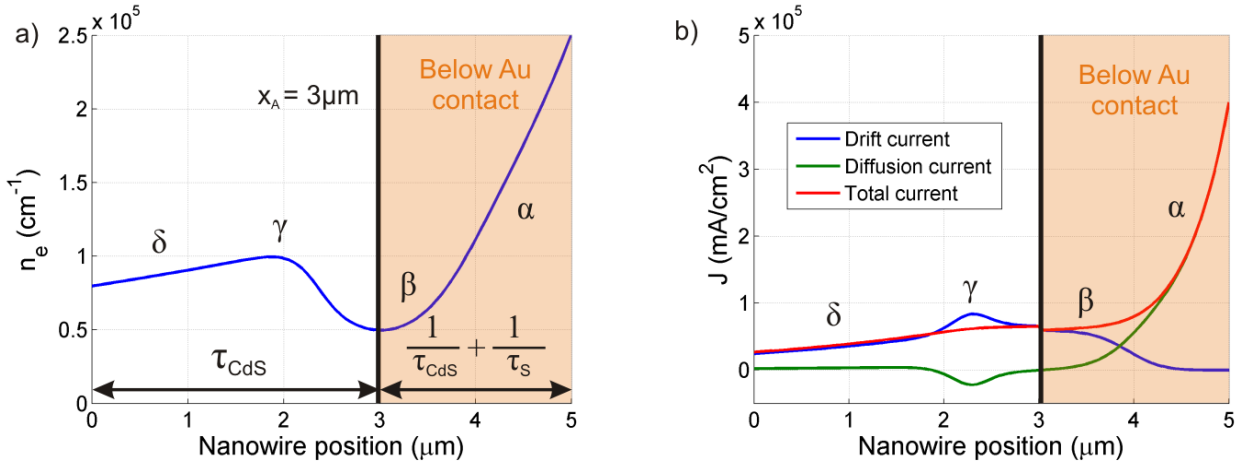


Figure 3.5: Calculated charge carrier density (a) and current density (b) along the CdS nanowire.

Charge distribution along the nanowire

Solving the differential equation 3.1 within the above framework yields the charge distribution along the nanowire, as shown in Figure 3.5.a. It can be seen that at the charge injection point ($x = L$) the electron density $n_e(x)$ reaches its maximum. Upon approaching the electrode edge, $n_e(x)$ steeply decreases (region α) due to recombination. At the electrode edge (position β), the electric field becomes so strong that the drift component of j_e (see equation 3.1 and 3.3) extracts charge carriers from below the contact, leading to charge accumulation outside the contact (region γ). This effect explains the minimum in the charge carrier density at the electrode edge. Further away from the contact (region δ) the charge carrier density decreases

more slowly, due to the internal field and the longer electron lifetime τ_{CdS} .

Based upon the charge distribution $n_e(x)$, the current along the nanowire can be calculated with the aid of equation 3.3. Thus obtained components of drift- and diffusion-current are plotted in figure 3.5.b. Deep within the contact region the electrode (position α) the current is mainly driven by diffusion. As expected for such type of transport, it exhibits an exponential decrease as a consequence of recombination. Around position β the drift current becomes dominant (compare with E_x in figure 3.2.e), while the diffusion current vanishes due to the local minimum in $n_e(x)$. This crossover of transport characteristics leads to the shape of the current profile in figure 3.1.c.

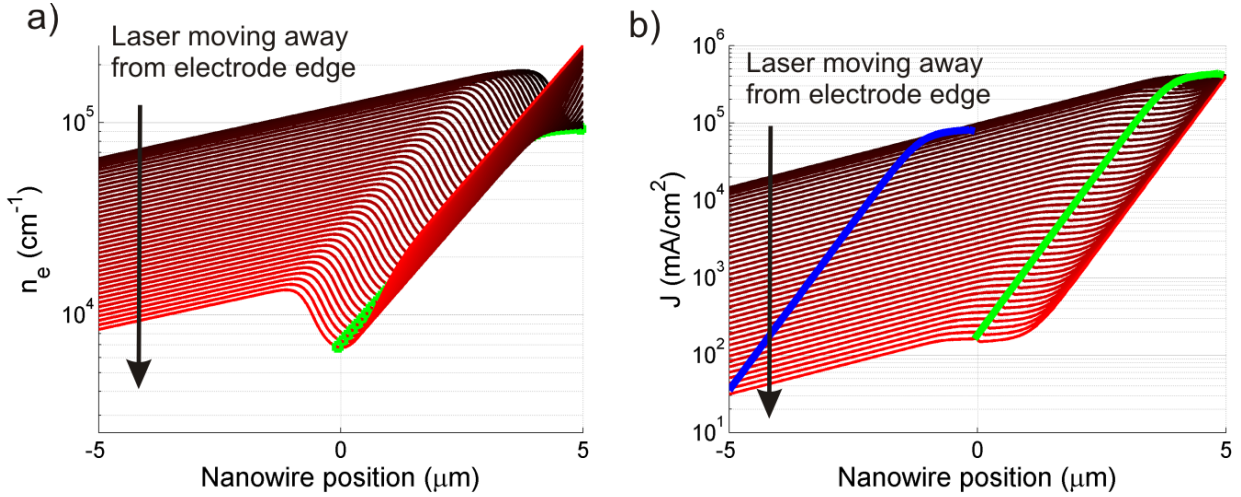


Figure 3.6: Calculated a) electron density $n_e(x)$ and b) electron current j for different charge injection points to reproduce the scanning of the laser spot along the nanowire. Charges are always injected at $x = 5 \mu\text{m}$. The green curve indicates the edge of the metal contact, while the blue curve marks the position of the titanium contact.

In order to simulate entire photocurrent profiles, the continuity equation has to be solved for the corresponding range of charge injection (illumination) points as illustrated by figure 3.6. The laser position is altered in the simulation by varying the distance between the charge injection point ($x = L$) and the edge of the metal contact (x_A , marked by the green line). The result are a series of curves for the electron density $n_e(x)$ (figure 3.6.a) and the current $j_e(x)$ (figure 3.6.b). The blue curve marks the position of the titanium electrode, where the electrons

are collected. Thus, in figure 3.7.a the current at the titanium electrode is plotted as function of the charge injection point (more precisely $x = L - x_A$).

Apparently, the model reproduces well the measured current profile in figure 3.1.c. While the exponential decay in region II can be attributed to the diffusion-limited current with its strong recombination characteristic, the constant current in region I arises from the high electric field close to the electrode edge which efficiently extracts all charges out of the contact. To properly account for this effect, it is necessary to choose the appropriate boundary condition. This precludes fixing the carrier density $n_e(x = L)$ to a constant value, corresponding to an infinite reservoir of charge carriers, as in this scenario, there would be no electric field which could deplete this reservoir, and the current profile would simply show an exponential decay. Instead, it needs to be considered that due to the spatially limited illumination only a finite particle current can be excited, and accordingly it is the current density which has to be set constant (see figure 3.4).

Charge carrier lifetime along the contact

We have furthermore measured the influence of the source-drain bias on the photocurrent profiles. Upon application of a negative bias the associated higher internal electric field reduces the recombination rate along the bare nanowire due to the additional drift current. As a consequence, the current profiles are shifted by an offset because the applied bias does not significantly modify the axial field below the contact (see figure 3.3.a).

However, the normalized experimental curves in figure 3.7.b display also a noticeable change in the slope, an observation that cannot be rationalized by the axial component of the electric field (E_x) which penetrates maximally $1\ \mu\text{m}$ into the contact (see figure 3.3.a). A plausible alternative explanation involves an increase in the radial E_y component which is expected to confine the electrons even closer to the SiO_2 interface and thus reduce the recombination rate. The 2D FEM calculations reveal that the reason why the E_y component is at all affected by the bias (see figure 3.3.b) is the presence of the backgate which fixes the potential at some distance to zero. This conclusion gains support from the experimental finding that a similar effect occurs upon the application of a gate voltage.

In figure 3.7.c, the measured variation of the electron diffusion length L_e , calculated from

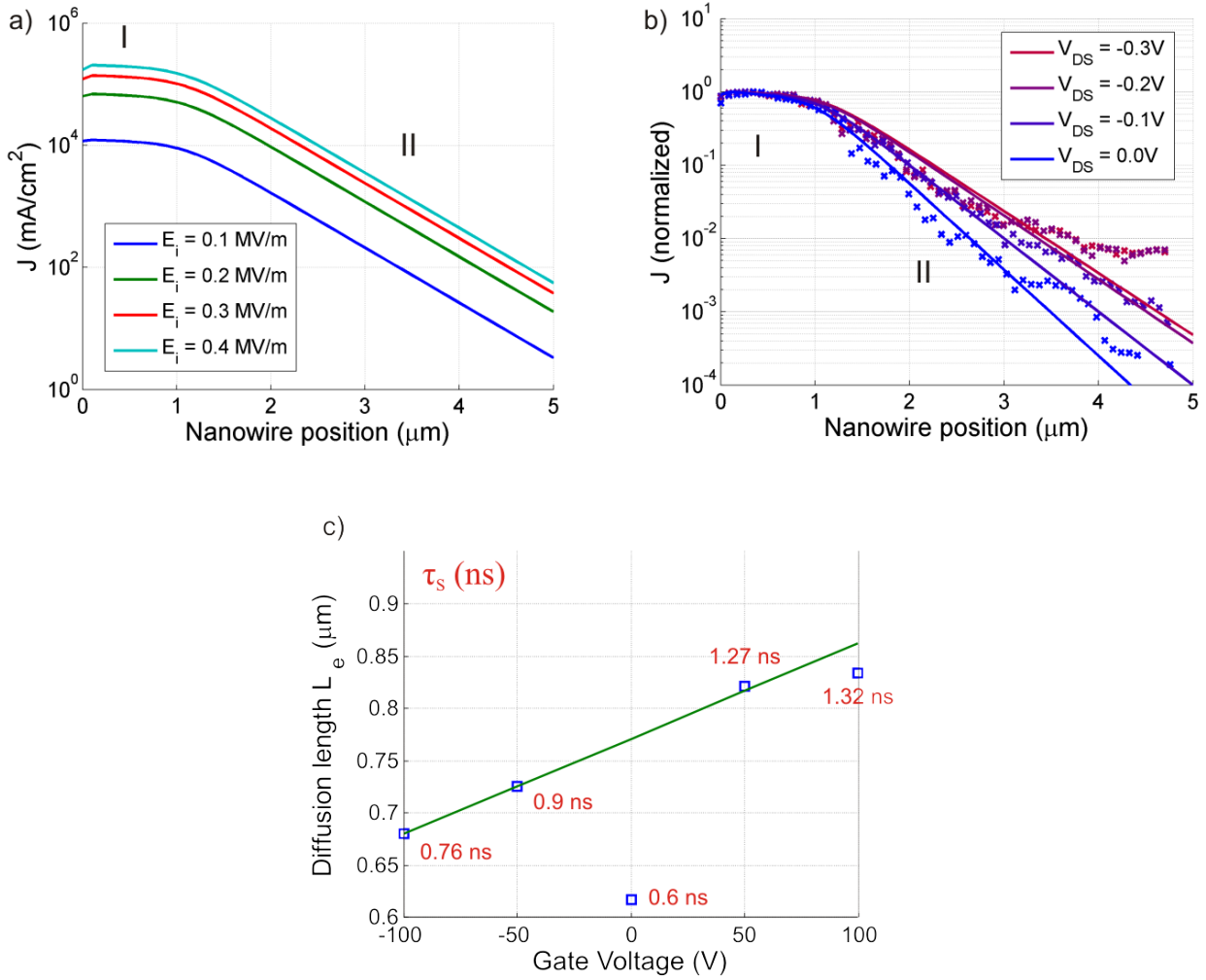


Figure 3.7: a) Calculated photocurrent profiles along the gold-coated CdS nanowire section for different internal electric fields. b) Fitted and calculated photocurrent profiles along the same wire section for different applied bias voltages. c) Electron diffusion length plotted as a function of the applied gate voltage. The red numbers are the corresponding lifetimes τ_s at each data point.

$L_e = \sqrt{D_e \cdot \tau}$, is plotted against the applied backgate voltage. Following the method of Gu et al. [65], the intrinsic value of the product $b_e \tau_{CdS}$ can be determined in CdS nanowires. In a separate device a CdS nanowire was connected by a gold and a titanium electrode. Contrary to the previously discussed devices in this chapter, both contacts were doped by an Argon plasma to obtain two Ohmic contacts. Figure 3.8.a shows the reflection image of such a device. In the

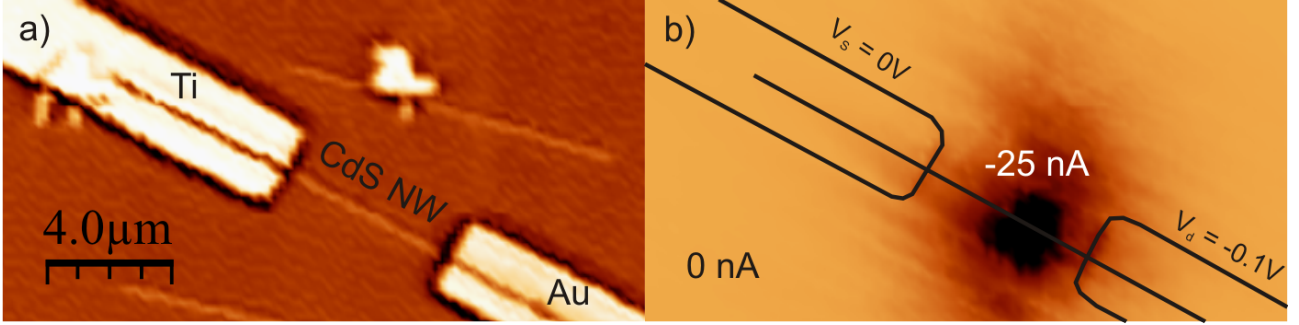


Figure 3.8: a) Reflection image and b) photocurrent map of a CdS nanowire with a titanium, and a gold contact. Both contacts are doped by an argon-plasma.

corresponding photocurrent map (figure 3.8.b, measured at $V_d = -0.1$ V) a local photoresponse appears at the nanowire, while no photocurrent is generated at the contacts. By fitting the spatial decay on both sides of the photoresponse to $\exp(-x/L_i)$ the intrinsic $b_i\tau_{CdS}$ product for electrons and holes can be obtained (see [65] for more details). Further, by assuming an electron mobility of $b_e = 300$ cm²/Vs [65, 69] and using equation 3.4, the recombination rate $1/\tau$ is obtained, which is included in the plot of figure 3.7.c. It should be mentioned that besides the change in the E_y component, an additional mechanism might play a role. This becomes evident from the intrinsic electron lifetime of CdS τ_{CdS} given by the relation

$$\tau_{CdS} = \frac{1}{R_{ec} \cdot N_A} \quad (3.5)$$

where R_{ec} is a material parameter depending on the recombination rate, and N_a is the hole concentration. Correspondingly, by increasing the hole concentration due to the gating, electron-hole pair recombination becomes more probable which is expected to lower the electron lifetime.

4 Graphene-Cadmium sulfide solar cells

Graphene, a perfect two-dimensional conductor made of sp^2 -bonded carbon atoms has attracted a lot of interest due to its rich physics. Examples are the study of massless Dirac fermions [72] or the room temperature quantum-Hall effect in graphene [73]. Besides the interest in this material for fundamental research also possible applications are envisioned. Owing to its high mobility it could be used in field effect-transistors (FET) [74, 75] or photovoltaic devices.

Graphene is a transparent and conductive material which can be produced at macroscopic scales (growth on copper [76, 77] or chemically derived [78]). It could hence serve as a replacement for transparent conducting oxides (TCO) in solar cells. The most commonly used TCO indium tin oxide (ITO), is less conductive than graphene, has a higher absorption and contains indium which is a rare element on earth. Graphene has already been successfully used in dye-sensitized solar cells [79] as a replacement of ITO. Furthermore, it has been blended with P3HT in bulk heterojunction solar cells [80] to improve the transport in these devices (compare with section 2.2.1).

To effectively integrate graphene in solar cells, the electrical contact between graphene and other materials is of great importance. While previous studies focussed on metal-graphene contacts [81], solar cells strongly depend on contacts to semiconductors. In this chapter, the photoelectric properties of a junction between graphene and a CdS nanowire is described.

4.1 Solar cell structure and assembly

To fabricate graphene-CdS junctions, graphene sheets were exfoliated on a silicon substrate with a 300 nm thick top layer of SiO_2 . The CdS NWs were synthesized by the same procedure as described in section 3.1, however, without surface treatment. They were deposited by spin coating 20 μ L droplets of the wire dispersion in ethanol at 5000 rpm. The graphene was then

contacted by gold/palladium (AuPd) electrodes, while the CdS nanowire was provided with a doped titanium contact (see section 3.1).

The device structure is illustrated by the optical micrograph in figure 4.1.a. The graphene sheet consists of two connected, parallel stripes ((I.) $0.3\ \mu\text{m}$ and (II.) $1.2\ \mu\text{m}$ wide)) which both cross the CdS nanowire. A close-up view of the intersection of the graphene and the nanowire (diameter $50\ \text{nm}$) is given by the atomic force microscopy (AFM) image in the inset of figure 4.1.a.

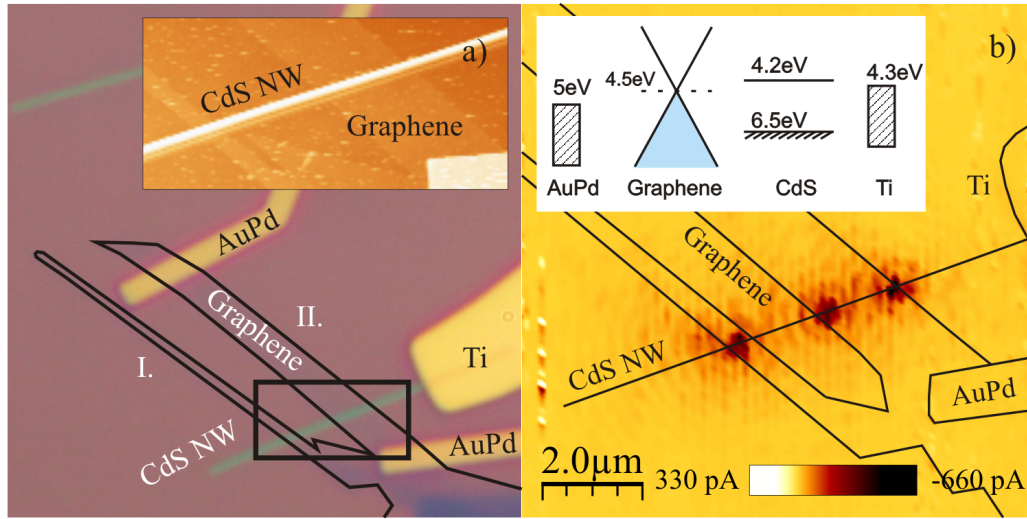


Figure 4.1: a) Optical image of a nanoscale graphene-CdS nanowire solar cell. The inset shows an AFM image of the graphene/CdS interface. b) Zero-bias SPCM image of a graphene-CdS nanowire device, revealing a photoresponse at the intersection of the graphene edge and the wire. The three major lobes are surrounded by concentric features which originate from diffraction of the focused laser beam. The inset depicts an energy diagram of the device components.

Figure 4.1.b shows the photocurrent map of the device with the titanium contact connected as source, and the AuPd electrode as drain. The SPCM image displays pronounced photocurrent signals on the order of $-0.7\ \text{nA}$ at the two intersections between the CdS nanowire and the two edges of the underlying wider graphene stripe (II.). By contrast, the edge signals have merged into one signal in case of the narrower stripe (I.). A similar signal pattern has been observed on six other samples. Among these, only two displayed a very weak response along the entire interface. All measurements were performed at $\lambda = 488\ \text{nm}$. At higher wavelengths, only

very low photoresponses could be observed since the excitation energy falls below the bandgap of the CdS.

The photocurrent response reflects the presence of potential barriers in the CdS wire, and their negative sign indicates that the local built-in electric field drives the photogenerated electrons along the CdS wire to the titanium contact, whereas the holes are injected into the graphene sheet from where they travel to the AuPd contact. It thus follows that upon contact formation between the two materials, electrons are transferred from the CdS nanowire to graphene, which leads to an upward band bending within the wire section close to the graphene interface. On this basis, it can be concluded that the CdS NWs are n-doped to such an extent that their work function is below that of graphene (4.5 eV [82]). This doping could be due to the introduction of sulfur vacancies on CdS wires, as documented by previous studies [83]. Especially at the surface of CdS such vacancies may be formed due to the reaction of sulfide ions with oxygen, leading to an overall n-doping of the nanowire. The finding that the photoresponse is strongly localized at the edge of the graphene sheet, instead of being distributed homogeneously along the entire CdS-graphene interface, can be partially ascribed to the presence of adsorbates on the graphene sheet, which can be removed by annealing (see below).

Another noteworthy observation is the lack of a photoresponse at the Ti-CdS nanowire and AuPd-graphene contacts in the photocurrent map. The same behaviour has been observed for several other graphene-CdS nanowire devices. A plausible explanation for the negligible signal at the Ti-CdS contact is the lower work function of titanium (4.3 eV [84, 85]) in comparison to graphene, which enables the formation of a quasi-ohmic contact, in close correspondence to observations made on Ti-contacted individual CdS nanoribbons [55]. Upon illumination of the AuPd-graphene interface, a flow of holes would be expected toward the metal contact due to the local potential step [80]. The absence of such signal is attributable to the electron transport barrier that exists at the graphene-CdS interface. This barrier also contributes to the very high device resistance in the dark.

4.2 Chemical interface tailoring

The weak, varying and inhomogeneous photocurrents are indicative of a non-intimate contact between graphene and the CdS wire. It could be significantly improved via chemical control of the graphene-CdS interface (figure 4.2.a). To this end, a similar treatment of the CdS NWs was

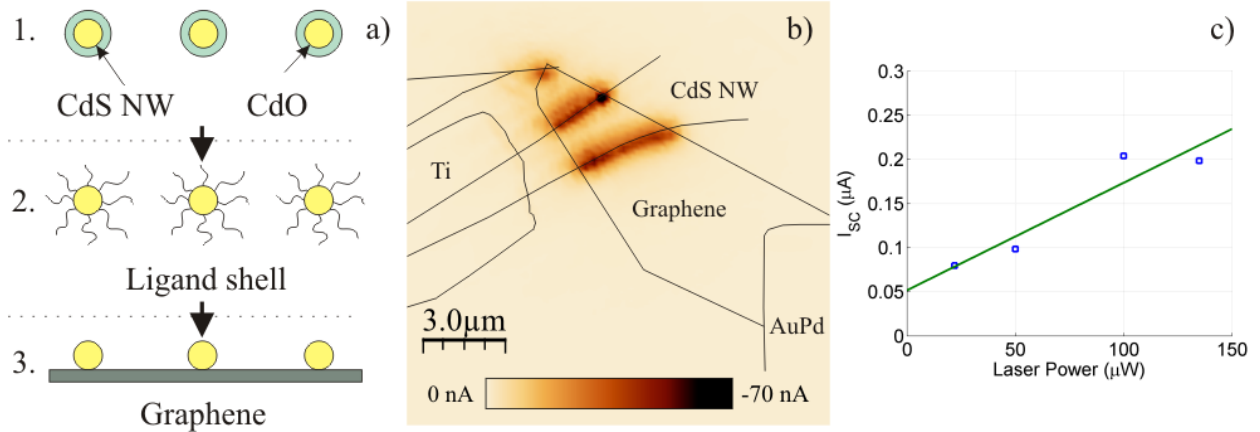


Figure 4.2: a) Scheme illustrating the chemical modification steps used to improve the coupling between a CdS nanowire and the underlying graphene. The steps comprise 1) the removal of CdO from the CdS wire surface by dilute aqueous acid, 2) addition of thioglycerol as a capping ligand, and finally 3) annealing to simultaneously remove the ligands and adsorbates on the graphene surface. b) A zero-bias photocurrent map of a graphene-CdS nanowire device subjected to the steps described in panel a. In contrast to unmodified devices, a strong photoresponse emerges along the entire graphene-CdS interface. c) The short-circuit current as a function of the illumination intensity. The green line is a linear fit of the data points.

performed as in section 3.1. In this case, thioglycerol $\text{HS-CH}_2\text{-CH(OH)-CH}_2\text{-OH}$ (10 μL per 10 mL) was used as a ligand to stabilize the CdS surface [86]. After removal of the excess thiol by several consecutive centrifugation and washing steps, the surface-capped CdS wires were deposited onto the graphene-coated substrate. Finally, an annealing step (15 min at 350°C under argon) was performed with the aim of removing the ligand on the CdS wire as well as adsorbates on the graphene sheet. These adsorbates are probably leftovers of the e-beam resist [87] combined with water adsorbed from the ambient [88].

The resulting improved contact between graphene and the CdS wire is manifested by two major changes in comparison to the above described devices, as can be discerned from the SPCM image in figure 4.2.b. Firstly, the devices displayed considerably larger short-circuit photocurrents, with reached up to 200 nA for strongest laser intensity (191 kW cm⁻²), corresponding to an enhancement by approximately two orders of magnitude. Secondly, the photoresponse is no longer restricted to the intersection between sheet edge and wire, but rather distributed along

the entire graphene-CdS interface. The creation of an intimate graphene-CdS interface during annealing is likely caused by coordinative bond formation between the Cd^{2+} ions on the CdS surface and the π -conjugated electrons in graphene, akin to the interaction between graphene and CdSe nanoparticles attached via a solution-based process [89]. It should be noted that also annealing alone, i.e., without prior CdO removal and CdS surface capping, resulted in a notable photocurrent increase, albeit the enhancement was limited to a factor of only ten.

It follows that the removal of contaminants on the graphene sheet contributes to the better electronic coupling between the two materials. Adsorbates on graphene are known to impede the charge carrier transport in graphene, making for example Joule heating necessary in order to remove these scattering centers and thus reach high electrical performance [90]. The samples could be stored for several weeks under ambient conditions without any observable degradation of the device performance. Figure 4.2.c shows the linear dependence of the short circuit current as a function of the illumination intensity, which is expected due to equation 2.27.

4.3 Device performance and efficiency

Figure 4.3 presents I/V-curves of a CdS-graphene junction before and after chemical interface improvement. As the devices are insulating in the dark, the generated photocurrents can be entirely attributed to separated electron hole pairs. With increasing negative bias the photocurrent rises owing to the enhanced separation of electron-hole pairs in the stronger electric field. Moreover, under forward bias there emerges a positive photocurrent, which likely originates from weak co-illumination of the Ti/CdS interface (see discussion below). The considerable photocurrent increase after interface improvement is accompanied by a decrease of the open-circuit voltage from 0.17 V to less than 0.1 V, pointing toward an increased recombination rate. The latter change causes a drop of the fill factor (FF) from 35 % to 23%, which falls significantly below values reported for dye-sensitized solar cells (FF up to 75 % [91]), but nonetheless compares favourably to graphene-based bulk heterojunction cells [92]. The absolute photocurrents collected from the present single-interface devices are inherently much lower than the currents in bulk solar cells. Downscaling the typical bulk photocurrents of the order of 1 mA/cm^2 to a single interface with an illuminated area of $0.07 \text{ }\mu\text{m}^2$ (corresponding to the size of the confocal laser spot) would yield a current of 0.7 pA, well below the 200 nA measured in our devices. Consequently, in the present SPCM experiments a measurable current is obtained only because

of the high illumination intensity.

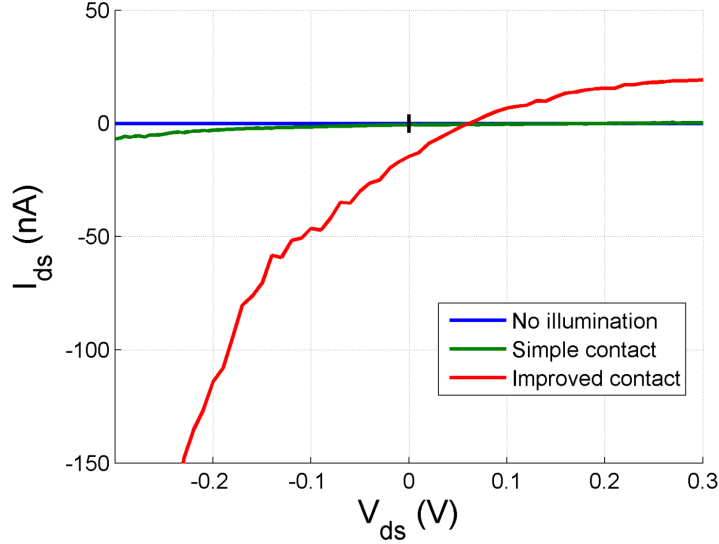


Figure 4.3: Current-voltage characteristics of a graphene-CdS nanowire device recorded under ambient in the dark (blue curve), without (green curve) and with (red curve) interface improvement. The laser spot ($\lambda = 488$ nm) was positioned at the maximum current of the SPCM map.

To account for the low absorption of the device, the internal power conversion efficiency (IPCE) is calculated. It provides the efficiency of the conversion of absorbed photons to charge carriers and is obtained by modifying equation 2.32:

$$\eta = \frac{V_{OC} \cdot I_{SC} \cdot FF}{I_{in} \cdot \alpha} \quad (4.1)$$

where α represents the fraction of absorbed light. A value of $\alpha = 0.01$ was calculated by FDTD simulations using Meep [93] (see ref. [94] for the optical constants of CdS). In contrast to bulk solar cells, re-absorption and light scattering, which would increase the length of the light path, play only a minor role in the present devices. Thus the amount of absorbed light is much lower, leading to a low α . Despite the small absorption, the IPCE remains small at 0.34 % as a consequence of the aforementioned high recombination rate. It is noteworthy that by inserting a hole blocking layer such as TiO_2 , the recombination and accordingly the IPCE might be improved, analogous to vertical carbon nanotube arrays coated with TiO_2 [95].

5 Electrical detection of surface plasmons

Surface plasmon polaritons (SPP) allow to efficiently confine incident light in the active area of solar cells (see section 2.2.4), which is used to improve the otherwise low absorption of thin-film devices. The possibility to confine electrical fields to subwavelength dimensions is the most important property of plasmonics. This capability could be exploited to build highly integrated optical circuits that operate at very high speeds. Most of the required passive plasmonic components such as waveguides [96], resonators [97], couplers [98], or interferometers [99] can already be routinely realized. However, in order to integrate SPPs with established semiconductor technology, it is necessary to electrically launch and detect surface plasmons at a microscopic scale. Plasmonic lasers [100, 101] and detectors [102, 103, 104, 99] mark first important steps in this direction.

In this chapter the contribution of surface plasmons to graphene/CdS solar cells (see chapter 4) is discussed. On this basis an electrical detector for surface plasmons was developed.

5.1 Surface plasmons in Graphene-CdS nanowire solar cells

The interface improvement described in section 4.2 enables the observation of an additional feature at the titanium electrode. Figure 5.1.a shows the photocurrent map of a graphene/CdS solar cell. For clarity the edges of the contacts, the nanowire and the graphene sheet are marked in the image. There is a negative photoresponse at the graphene/CdS interface, which was already discussed in section 4.2. Additionally, a positive photo response appears at the edges of the titanium electrode and along the nanowire beneath the electrode.

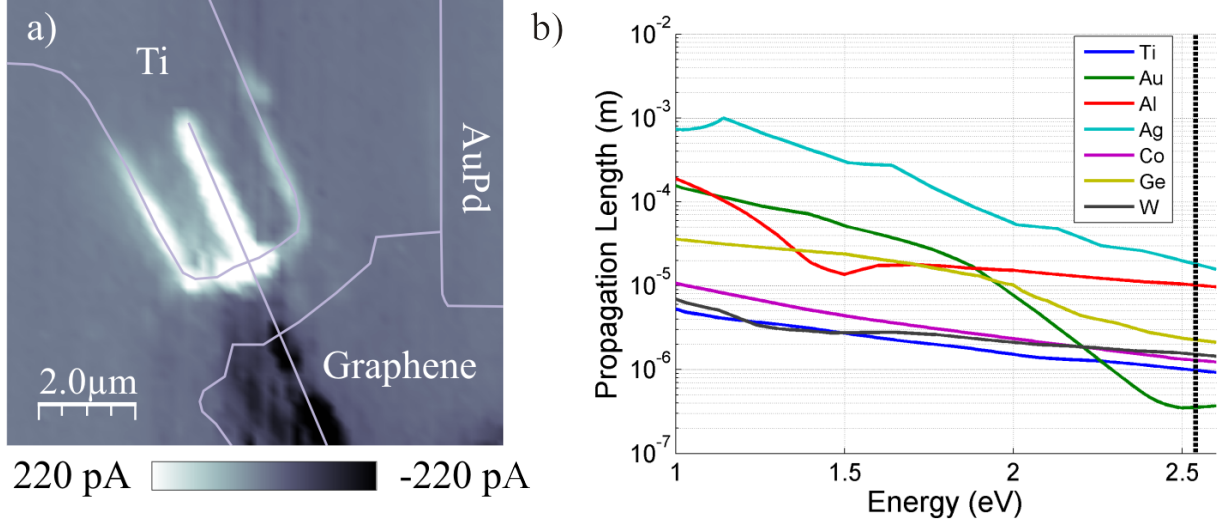


Figure 5.1: a) Photocurrent map of a graphene/CdS solar cell. b) Propagation length of surface plasmons for different metals, as a function of energy. The broken, black line marks the energy corresponding to the wavelength of 488 nm.

The photo current at the edges of the titanium electrode cannot be explained by charge excitation and separation as in semiconductors. Metals have much higher charge carrier densities ($10^{22} - 10^{23} \text{ cm}^{-3}$) which lead to very fast recombination times and hence charge separation is very unlikely. Instead, the excitation of surface plasmons offers a reasonable explanation for this photosignal.

To excite surface plasmons, the wave vector of freely propagating light has to be matched to the dispersion relation of a SPP. In the present device, the sharp edge of the titanium contact acts as a single ridge of a grating. In k -space this allows the coupling to numerous plasmonic modes [105], which then propagate at the Ti/air and Ti/SiO₂ interface. When these modes intersect with the CdS NW, the light component excites charge carriers which are separated in the electrical field of the contact. The plasmon propagation is limited by the decay length L , which is defined as the length over which the surface plasmon is attenuated by $1/e$. It can be calculated by $L = 1/2k_{x,Ti}$, with $k_{x,Ti}$ as the imaginary part of the wave vector which is given by [106]:

$$k_{x,Ti} = k_0 \sqrt{\frac{\epsilon_{Ti} \cdot \epsilon_{air}}{\epsilon_{Ti} + \epsilon_{air}}} \quad (5.1)$$

where k_0 is the wave vector of the propagating wave in vacuum and $\epsilon_{Ti/air}$ is the permittivity of titanium/air as a function of the wavelength. Figure 5.1.b shows the plasmon decay length L for different metals as a function of excitation energy. The SPCM measurements are performed at $\lambda = 488$ nm (marked by the black line). Titanium has a propagation length of roughly $L = 1 \mu m$. The plasmon decay explains why the edges of the titanium contact (figure 5.1.a) which are farther away than L from the CdS NW do not show a photoresponse.

5.2 Electrical detection of SPPs

The effect described above is a suitable basis for the electrical detection of surface plasmons in nanoscale devices. However, it would be desirable to increase the propagation length and to improve the coupling efficiency of the surface plasmons. For this purpose we have used another metal than Ti to fabricate the grating. Figure 5.2.a shows an optical reflection image of such a device. The cross-section of the device along the dashed line is schematically depicted in figure 5.2.b. Surface plasmons are launched at the grating and propagate along the metal stripe until they intersect with the CdS nanowire. The nanowire lies on top of the aluminium and forms a Schottky contact with a titanium electrode. In contrast to the previous devices the plasmon propagates along a metal stripe while the electrical contact is realized separately. This configuration effectively combines the advantages of both materials, aluminium and titanium. Specifically, as figure 5.1.b shows, aluminium allows more efficient propagation of surface plasmons (propagation length $L \approx 10 \mu m$). Only silver would be a better choice at this wavelength (488 nm), but it is less stable against oxidation. However, aluminium forms high resistive electrical contacts to CdS. Titanium, by comparison, yields good Schottky contacts (work function 4.3 eV [85]) on CdS, but is a poor plasmonic waveguide.

The light coupling to the surface plasmons is improved by using a small grating, consisting of three ridges. The dimensions of the grating, with a spacing of 265 nm, a width of 216 nm, and a height of 80 nm, have been adapted to the used materials and laser wavelength [105]. Due to the limited laser spot size achieved by the 50x air objective (NA = 0.8), the number of aluminium ridges in the grating has been restricted to three. The coupling efficiency of a grating is at maximum when the incident light is linearly polarized perpendicular to the ridges

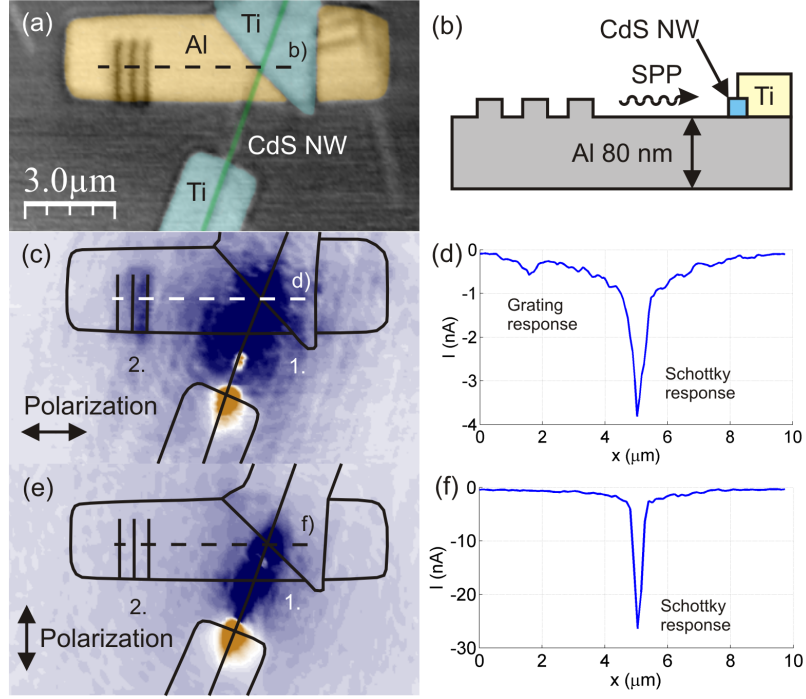


Figure 5.2: a) Reflection image and b) corresponding schematic cross section of a typical device. The Ti electrodes and CdS NWs are colored to increase their visibility. Panels c) and e) show the photocurrent maps of the same device for respective light polarization perpendicular and parallel to the grating. The dashed lines in panels c) and e) correspond to the current profiles d) and f), respectively.

of the grating. If the polarization is parallel to the ridges the coupling strength goes to zero. Accordingly, polarization-dependent measurements provide valuable hints for the existence of surface plasmons [107].

The devices were fabricated by consecutive e-beam lithography steps. The CdS NWs were spin-coated onto the Si substrate coated with a 300 nm thermal oxide layer. Prior to the evaporation of 100 nm titanium, the contact areas on the CdS NWs were exposed to an argon plasma for 2 min in order to achieve local n-type doping [64].

Figure 5.2.c and 5.2.e display photocurrent maps recorded on the device in figure 5.2.a with light polarization perpendicular and parallel to the grating, respectively. The current profiles in figure 5.2.d and 5.2.f are taken along the corresponding dashed lines in panel 5.2.c and 5.2.e.

Both maps exhibit two major signals, one at the contacts (1.) and the other at the grating (2.). The strong signal at the titanium electrodes originates from the direct illumination of the Schottky contact. It shows pronounced polarization dependence, with maximum magnitude for light polarization parallel to the nanowire long axis [108]. Simulations of CdS nanowires on an aluminium surface reveal their optical absorption to differ by a factor of 9 between the two polarization directions. This difference agrees well with the 7 to 8-fold larger signal in case of the parallel light polarization. The second photoresponse in figure 5.2.c at the grating can be attributed to surface plasmons, as supported by its polarization dependence. If the incident light is polarized perpendicular to the ridges a photoresponse appears at the grating (figure 5.2.c) which vanishes for parallel polarized light (figure 5.2.e). This is expected for a plasmonic coupler [107]. In the photocurrent profile of figure 5.2.d the plasmon response can be discerned, although it overlaps with the spatially decaying signal of the Schottky contact.

5.2.1 Polarization dependence

To better distinguish the plasmon response from stray light at the nanowire contact, the device structure was modified by capping the Schottky contact by a thick metal layer, as depicted in figure 5.3.a and the corresponding cross-section in figure 5.3.b. To this end, a 200 nm thick layer of SiO₂ was evaporated onto the whole substrate, and a restricted area around the Schottky contact selectively covered by another 80 nm layer of aluminium. This resulted in a metal-insulator-metal (MIM) structure which prevents direct illumination of the contact, but does not hinder the propagation of plasmonic transversal magnetic (TM) waves. Figure 5.3.c and 5.3.d display the photocurrent maps of such a device, acquired with perpendicular and parallel light polarization, respectively. For polarization perpendicular to the ridges (figure 5.3.c), three photoresponses at different locations can be distinguished. The first signal occurs at the edge of the top metal layer, which can also excite modes inside the MIM structure. The second one is due to surface plasmons launched at the grating. The shape of the two separate peaks in the photo response will be discussed further below. A third signal emerges at the left outer edge of the aluminium stripe. At this aluminium/substrate interface, a plasmon is launched which does not intersect directly with the CdS NW, and therefore results in only a very weak signal. In case of light polarization parallel to the grating (figure 5.3.d), the photoresponse unexpectedly doubles in size. It furthermore changes its shape, leading to a broad photoresponse in the vicinity of the MIM structure, with some minima at the grating position. At the same time, no separate contribution from the edge of the top metal layer can be observed.

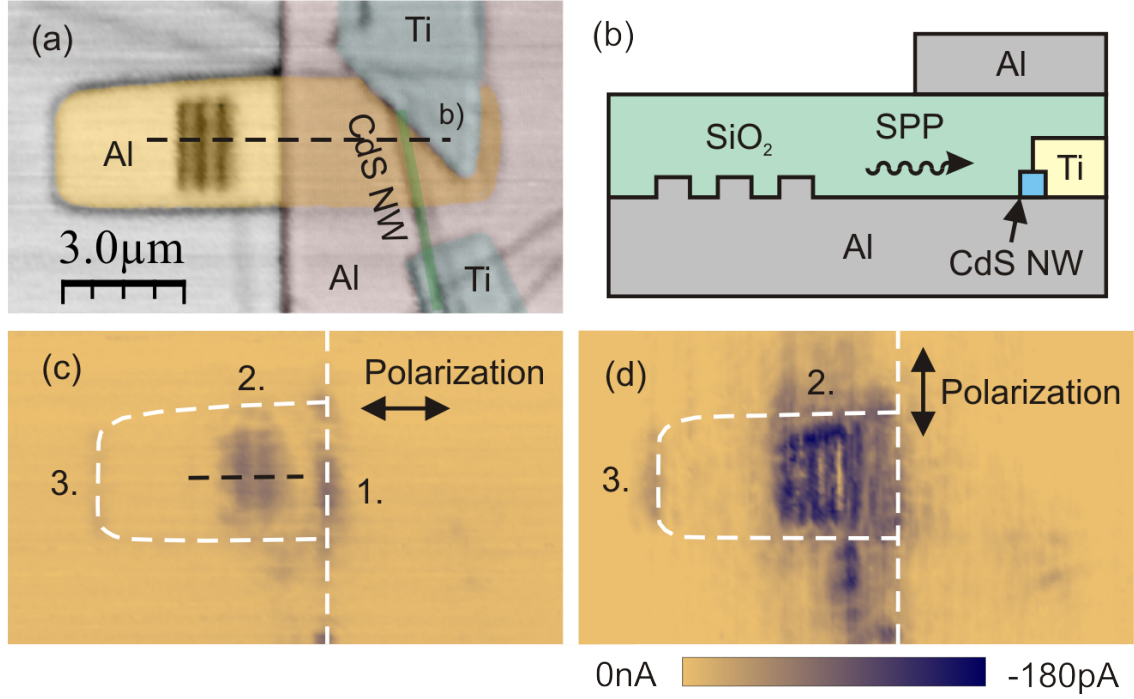


Figure 5.3: a) Colored reflection image and b) corresponding schematic cross section of an Al-capped device. The panels c) and d) show the photocurrent map for light polarization perpendicular and parallel to the grating.

5.2.2 FDTD calculations

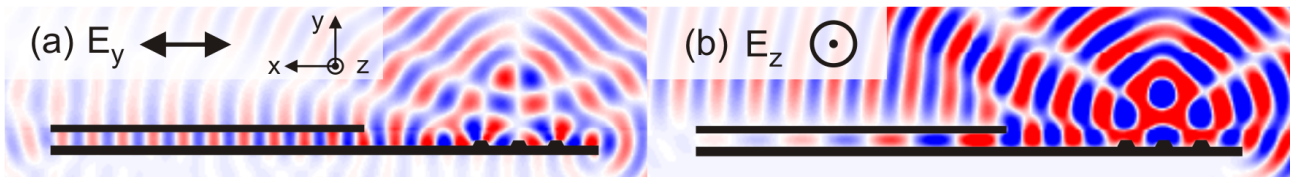


Figure 5.4: Finite difference time domain calculations of the device structure. Panel a) shows the E_y component of a TM-wave (source polarized in E_x) and b) the E_z component of a TE-wave (source polarized in E_z).

Valuable clues regarding the origin of the detected polarization dependence could be gained from Finite Difference Time Domain (FDTD) simulations of the plasmon detection devices. Two-dimensional calculations were performed using the Meep software package (see Oskooi et

al. [93] and Mathewson et al. [109] for optical constants of aluminium), with the light source modelled by a Gaussian field distribution with a FWHM of 450 nm. The calculated electric field distribution for both polarization directions is shown in figure 5.4, where the bold black features represent the aluminium layers and the grating. For a MIM mode to be excited by a surface plasmon (see figure 5.4.a), the light source must be polarized perpendicular to the grating (E_x component, not shown here). Such a mode corresponds to a TM-wave comprising E_x , E_y and H_z components. Of these, the major field component E_y is plotted in figure 5.4.a, in which the propagating wave in the MIM structure can be clearly seen. Conversely, for light polarization parallel to the grating, one would expect no plasmon propagation since surface plasmons only exist as TM-waves [110] and a light source polarized in E_z cannot (in 2D) couple to a TM mode. Hence, the MIM mode in figure 5.4.b must be directly excited corresponding to a TE-wave (H_x , H_y , E_z). As reported by Dionne et al. [96], it is possible to excite TE-waves in MIM structures at short enough wavelengths (<600 nm). The dispersion relation of such a mode crosses the light line, such that no grating is needed to achieve a k-vector matching. Consequently, any scattered light with polarization in the E_z direction that reaches the MIM structure can easily couple to the TE mode. Standard multilayer eigenmode calculations revealed the existence of an excitable TE mode with a propagation length of around $3.5 \mu\text{m}$ for the given device structure. Even though this mode is strongly damped, it is absorbed more strongly by the CdS nanowire, since the E_z component lies in the plane of the nanowire. This mechanism is also operative for the device in figure 5.2, and explains the higher photocurrent observed for parallel polarization in this case (cf. figure 5.3.d).

5.2.3 Position-dependent coupling efficiency

To further elucidate the coupling mechanism, the plasmonic light flux was calculated as a function of the source position, thus simulating the SPCM measurements. In previous experiments wherein light was focused on single ridges, the maximal coupling efficiency was found to be centred over the single ridge [111]. The situation is different for the present devices, since the launched plasmons can be detected only in one direction, whereby the coupling maximum is shifted to one side. In figure 5.5.a, the computed data is compared to the normalized, measured data for light polarization perpendicular to the grating. While the profile obtained for perfect rectangular ridges exhibits its maximum on the right side where the detector is located, it is unable to account for the left maximum in the measured photocurrent (red squares, taken from the profile in figure 5.3.c). Significantly better agreement is achieved by incorporating a

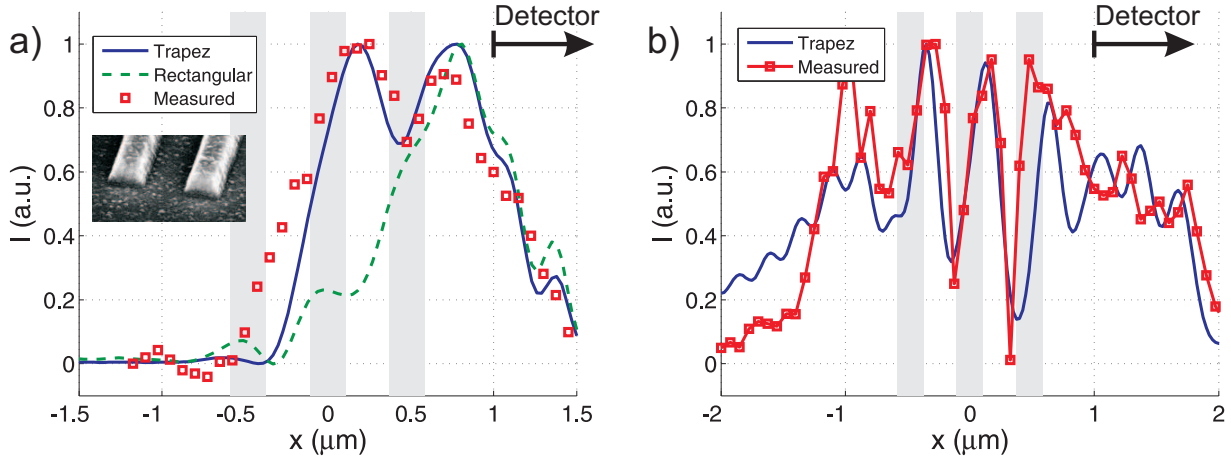


Figure 5.5: Comparison of measured photocurrents (see figure 5.3) and the calculated coupling efficiency for light polarized perpendicular a) and parallel b) to the grating. The gray bars in both panels mark the position of the grating.

trapezoid shape of the ridges, which is apparent from SEM images of the grating (see inset of figure 5.5.a). It is known from previous studies (see Radko et al. [105]) that the shape of the ridges and the spacing of the grating can significantly alter the coupling efficiency to surface plasmons. The trapezoid shape originates from metal deposited on the side walls of the PMMA resist during the evaporation of the grating.

Additionally figure 5.5.b shows the position-dependent coupling efficiency for light polarized parallel to the ridges. Although the coupling mechanism is different (see previous section), there is also a good agreement between the measured profile and the calculated coupling efficiency.

5.2.4 Bias dependence

CdS nanowire based devices are good photodetectors due to their high sensitivity [54] and the negligible dark current (in the range of pA [112]). Thus, even under applied bias, the total current can be entirely attributed to photoexcitation. Figure 5.6 shows the current-voltage curve of a surface plasmon detector with a top metal layer (like in figure 5.3). Without illumination no current is observable (blue curve). Upon illumination, but without bias, a photocurrent of 0.3 nA is measured. Already at $V = -0.5$ V the current increases by three

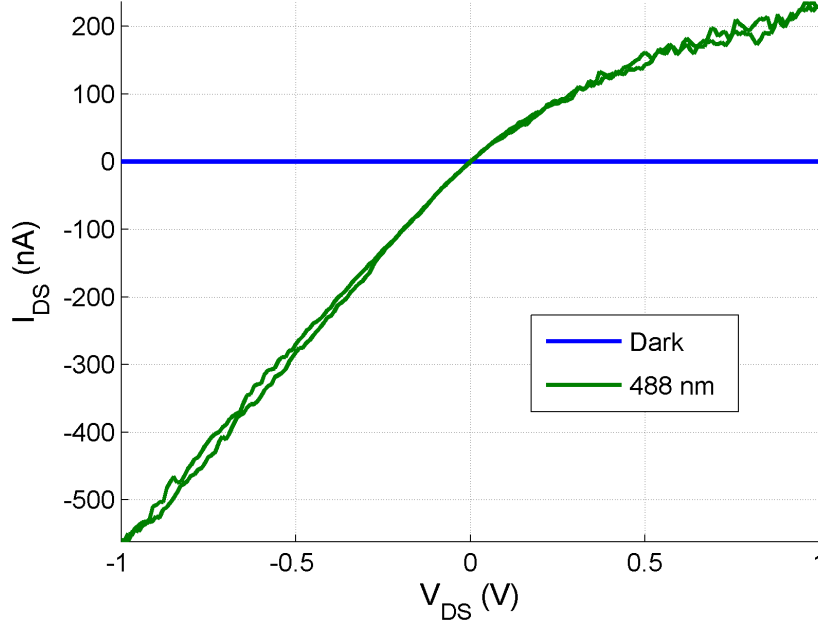


Figure 5.6: Current-voltage curve of a MIM surface plasmon detector. The blue curve is measured without illumination, while the green curve is recorded with the laser spot positioned directly on the grating.

orders of magnitude to 300 nA. By applying a bias between both titanium contacts, the electron-hole recombination along the nanowire is lowered due to an additional drift current. Thus charge carriers which are excited further away from the electrodes than their diffusion length can also contribute to the photocurrent. Furthermore, under an external bias ϕ the depletion zone width $x(\phi) = \sqrt{2\epsilon|V|ne}$ is increased (with n as the charge carrier density, e the elementary charge, and ϵ the dielectric constant of CdS), which additionally leads to a larger area of absorbed photons.

6 Hybrid organic solar cells

In hybrid solar cells, charge carriers are separated at the interface between an organic donor and an inorganic acceptor material. The inorganic component can either be prestructured or directly mixed with the organic phase to form an interpenetrating network (see section 2.2.2). In either case, the device performance depends strongly on the charge transport efficiency. Especially in blend solar cells, percolation transport leads to significant losses.

This chapter deals with SPCM as a tool to explore the charge transport in model systems for blend and prestructured hybrid solar cells. It is first described how the lateral, hybrid solar cells were fabricated, and then the SPCM data of devices combining P3HT with CdSe nanoparticles or CdS nanowires are shown.

6.1 Anodic oxidation of titanium

A well-studied material combination in hybrid solar cells is made of titanium dioxide (TiO_2) and P3HT. TiO_2 is a wide bandgap (3.7 eV) semiconductor which exists under normal pressure in three different phases: anatase, rutile and brookite. The stable form is rutile, into which anatase and brookite are converted upon annealing. Within TiO_2 /P3HT solar cells, rutile yields lower V_{OC} , but higher J_{SC} and longer device stability [113]. The major advantage of TiO_2 is its very low lying valence band, rendering it an effective hole blocking material. Practically, only electrons can be transferred into the TiO_2 which allows an efficient charge separation at the interface and reduces e-h recombination.

For the fabrication of lateral, hybrid solar cells titanium electrodes were structured by e-beam lithography and then partially oxidized to TiO_2 . A combination of anodic oxidation and thermal annealing was used for the latter task. A specific advantage of anodic oxidation is the good control over the morphology of the formed oxide. For instance, when diluted hydrofluoric acid (HF) is utilized as electrolyte, nanowires of TiO_2 can be directly grown on a titanium

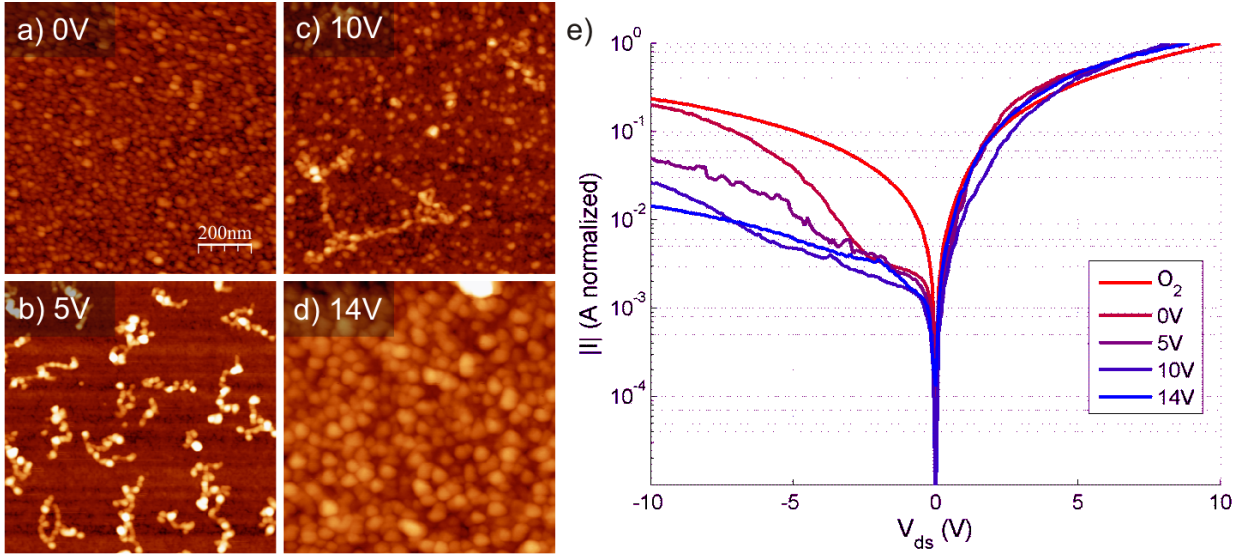


Figure 6.1: AFM images of titanium electrode which was anodized for 5 minutes at an overpotential of a) 0 V, b) 5 V, c) 10 V, or d) 14 V. In panel e) the current voltage curves of a TiO_2 / P3HT / Au diode are compared for different applied overpotentials and oxygen plasma treatment.

film [114, 115]. Here, the major focus is on studying the electronic properties of the interface, which requires flat, dense, and thin films of TiO_2 . These could be obtained using 1 M of H_2SO_4 as electrolyte [116, 117]. By varying the voltage the film thickness could be adjusted properly (roughly 3 nm/V). Figure 6.1.a-d shows AFM images of titanium electrodes after overpotentials of different magnitude were applied for 5 minutes. At 0 V no significant oxidation process took place and no difference to a freshly evaporated titanium film could be observed. Nevertheless, probably a thin layer of TiO_2 is covering the surface. Upon increasing the voltage (5 V and 10 V) irregular structures appeared on the surface. Only at 14 V a regular layer formed, accompanied by a significant colour change in optical images of the electrode (not shown).

Figure 6.1.e displays current-voltage curves of the oxidized electrodes incorporated within a TiO_2 /P3HT/Au diode. The higher the overpotential used for the oxidation step the lower is the reverse current of the diode, indicating that less holes can be transported through the titanium layer. For comparison, a device with a titanium electrode treated by an oxygen plasma is included ($P = 200$ W, $p = 0.3$ Torr, $t = 30$ sec). Apparently, the plasma produces only a very thin and permeable layer of TiO_2 , as concluded from the high reverse current and the

unchanged electrode colour of the optical images.

In a final step, the oxidized TiO_2 electrodes were annealed for 10 minutes at 370°C under ambient. The short circuit current was found to be significantly increased after the annealing, suggesting that this step further improves the stoichiometry of the film by saturating remaining oxygen vacancies.

6.2 Photocurrent distribution in $\text{TiO}_2/\text{P3HT}/\text{Au}$ devices

In figure 6.2, SPCM results obtained from a $\text{TiO}_2/\text{P3HT}/\text{Au}$ solar cell are shown. The inset in figure 6.2.a shows a side view of the sample structure. Titanium and gold electrodes were defined by e-beam lithography. The surface of the titanium electrode was oxidized by the procedure described above, leaving a conductive metal core in the center. Finally, a layer of P3HT was spin coated over the sample. Figure 6.2.a displays the reflection image and 6.2.b the corresponding photocurrent map of the device. The gold and titanium electrodes were placed at varying distance to study transport effects in the solar cell. As apparent from figure 6.2.b there is a photoresponse only at the TiO_2 electrode which vanishes at the edges of the contact. The signal is confined to the electrode since only excitons which are generated at a distance of the exciton diffusion length (see section 2.2.1) can contribute to the photocurrent. The absence of a photoresponse at the gold electrodes is a consequence of the almost identical work function of P3HT and gold. In figure 6.2.c, current-voltage curves of the device are compared in the dark and under illumination. One obtains a fill-factor of 0.36, a short circuit current of ≈ 0.5 nA, and an open circuit voltage around 0.42 V, which is a bit lower than in bulk devices (0.51 V, [39]).

6.3 Blend solar cells: Ligand exchange of CdSe NP

A quite simple but efficient solar cell is obtained using a blend of CdSe NPs and P3HT (see section 2.2.2). Upon illumination, charge carriers are excited in both materials and separated at the heterojunction. The holes are transported in the P3HT layer to the gold electrode, while the electrons move along the semiconductor nanoparticles.

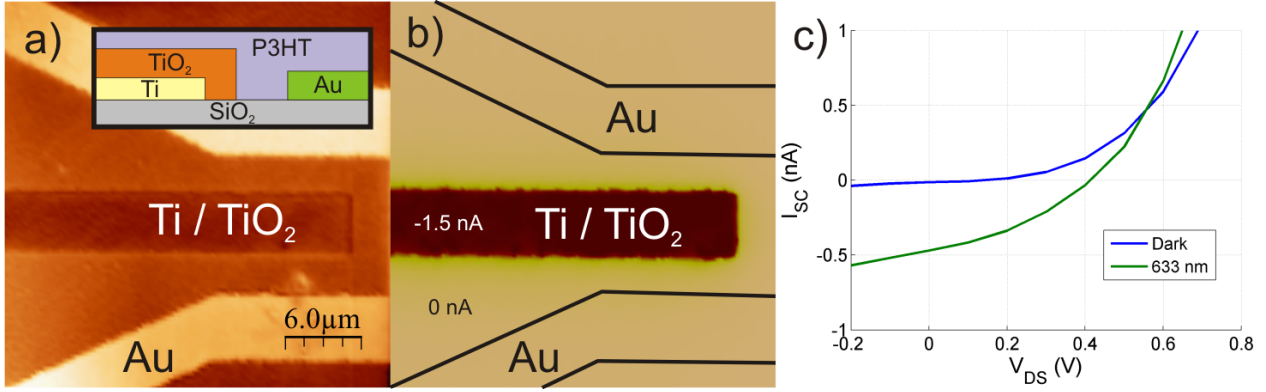


Figure 6.2: a) Reflection and b) photocurrent map of a TiO₂/P3HT/Au solar cell. The inset in panel a) is a schematic side view of the sample. Panel c) shows the current-voltage characteristic of the device in the dark and under monochromatic illumination with 633 nm.

The major limitation of this type of device is the electron transport along the percolation network of the nanoparticles. To study this type of transport a thin film of CdSe NPs was inserted between the TiO₂ and the P3HT layer (see figure 6.3.a). In contrast to the TiO₂/P3HT/Au devices, an additional photoresponse would be expected between the TiO₂ and the gold electrode, as in this region charge carriers are separated at the CdSe/P3HT interface.

Figure 6.3.b shows photocurrent profiles (measured by SPCM) of two differently treated TiO₂/CdSe NP/P3HT/Au devices. Since the photoresponse at the CdSe/P3HT heterojunction is very small, semi logarithmic current profiles along a direction perpendicular to the TiO₂ electrode (see black line in inset) are shown. The position of the TiO₂ electrode is marked in the middle by a grey bar.

In one case, the device was annealed after the CdSe nanoparticle deposition for 15 minutes at 150°C (green curve) to render the CdSe film more compact. This step did not damage the nanoparticles, as confirmed by photoluminescence measurements before and after. Figure 6.3.b reveals that the photocurrent strongly decreases away from the TiO₂ electrode. This spatial decay of the photocurrent is probably widened due to the convolution with the finite laser spot size.

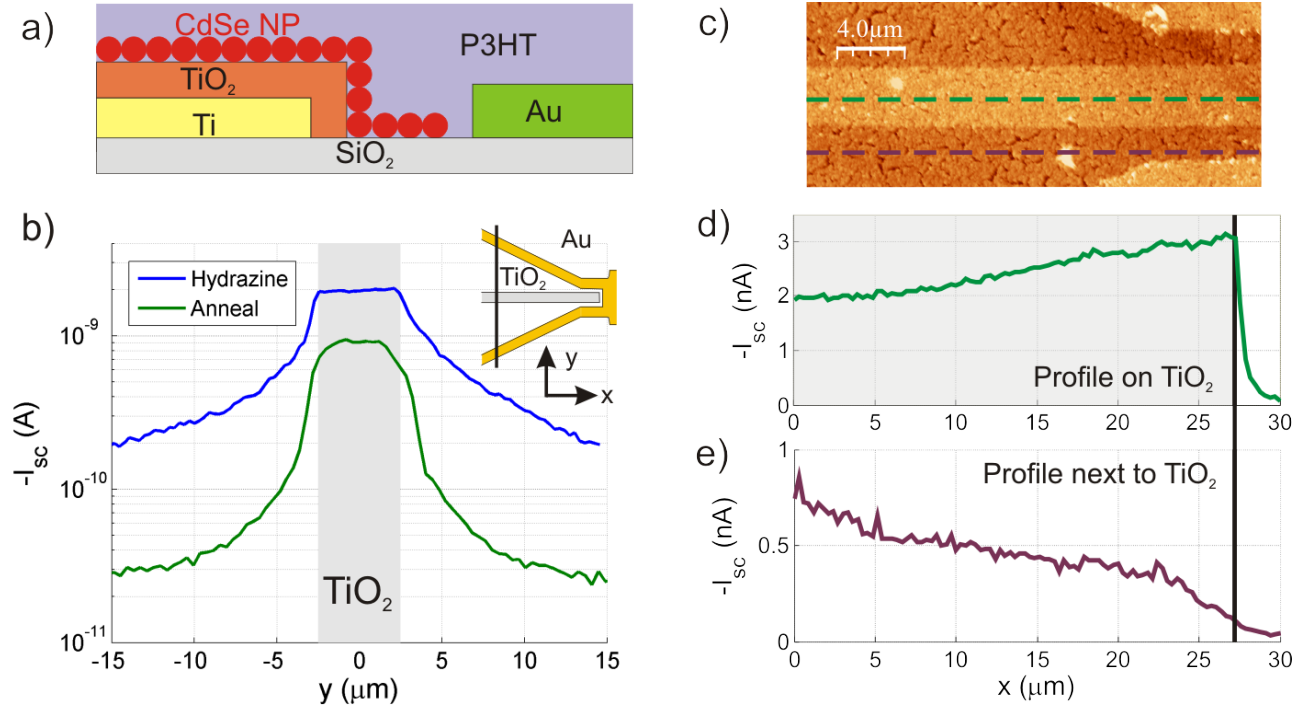


Figure 6.3: a) Schematic representation of a TiO₂/CdSe NP/P3HT/Au solar cell. b) Photocurrent profiles (marked in inset) of devices which were treated by temperature (green curve) or hydrazine (blue curve). AFM image of hydrazine treated CdSe nanoparticle film. d) Photocurrent profile along d) and beside e) TiO₂ electrode.

As described in section 2.2.2, ligands on the nanoparticle surface can impede the charge transport. One possibility to enhance the conductivity is to exchange the ligands by short ligands in order to decrease the interparticle spacing. One option is to use metal chalcogenide complexes [118, 119] which allow to fabricate FETs comprising CdSe NP films with mobilities of 16 cm²/Vs. In the present work, the nanoparticles were exposed to hydrazine (1 M in acetonitril for 12 hours, [120]). As a result of this treatment cracks were formed, as exemplified by the AFM image in figure 6.3.c. The blue curve in figure 6.3.b evidences that the photocurrent response of the hydrazine-treated film is significantly increased, not only on the TiO₂, but also around the electrode edge.

The photoresponse in the hydrazine-treated samples was found to depend on the distance between the gold and the TiO₂ electrode, as demonstrated by the comparison of photocurrent profiles along the TiO₂ electrode (6.3.d) and beside it (6.3.e) (profiles are marked in figure 6.3.c).

On top of the TiO_2 electrode (profile 6.3.d) the photocurrent increases with decreasing distance between the TiO_2 and the gold electrode. This behaviour is expected since a smaller electrode distance should result in a lower Ohmic resistance. Conversely, the photocurrent next to the electrode (profile 6.3.e) increases at greater electrode distances. One plausible explanation for this difference could be the numerous cracks in the CdSe nanoparticle film. Since they are up to $2\ \mu\text{m}$ long, they may indeed block the electron current at short electrode distances. For larger electrode distances, in comparison, there are more pathways available for the transport, thus leading to a higher conductivity.

6.4 Nanostructured solar cells: charge transfer at CdS-P3HT heterojunction

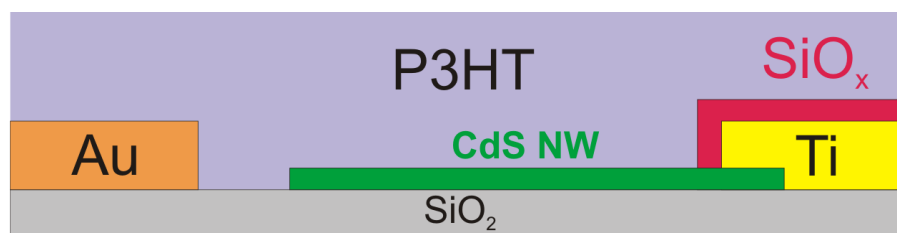


Figure 6.4: Schematic drawing of a nanoscale CdS NW/P3HT heterojunction. The CdS NW is contacted by a titanium electrode covered with SiO_2 . The hole transport occurs over the P3HT to the gold electrode.

The nanoparticle films in the previous section, even after chemical treatment, exhibit only a very low conductivity which varies significantly from sample to sample. To avoid these problems the nanoparticle film was replaced by a single crystal CdS nanowire (see previous sections). The resulting devices are interesting since they represent the basic functional unit of a nanostructured solar cell made of vertical arrays of nanowires (see section 2.2.2). Figure 6.4 shows a schematic cross-sectional view of such a device. The surface-functionalized nanowires were deposited by spin coating on a Si/SiO_2 substrate, followed by e-lithography to define the gold and titanium electrodes. To assure a good electrical contact, the CdS nanowire was locally doped by an argon-plasma prior to titanium deposition (see section 3.1). As the titanium electrode is not oxidized, it was covered by an approximately 200 nm thick layer of SiO_x in the next step. Finally, a layer of P3HT was spin coated over the hole sample.

In figure 6.5.a a reflection image of a representative CdS/P3HT heterojunction device is shown. The gold electrode is arranged at a constant distance from the CdS nanowire such that the photocurrent distribution along the wire is not influenced by the transport through the P3HT. Figure 6.5.b and 6.5.c show photocurrent maps of the device recorded at a wavelength of 633 nm and 488 nm, respectively. In both cases, the major photoresponse is located at the nanowire itself. Depending on the excitation energy, the signal has a maximum either close to the titanium contact ($\lambda = 633$ nm) or is evenly distributed along the entire nanowire ($\lambda = 488$ nm). There is also a small photoresponse at the edges of the gold contacts, which is further discussed in section 7.7.

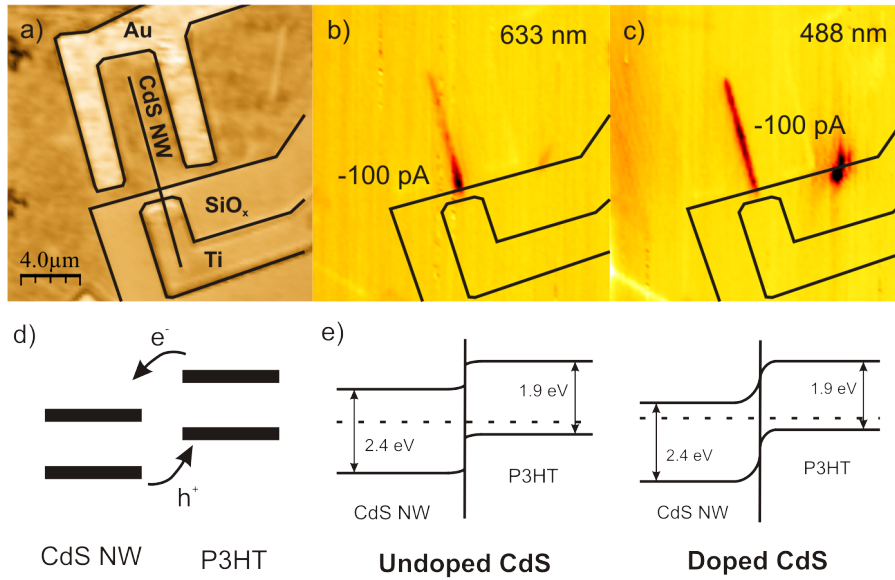


Figure 6.5: a) Reflection and photocurrent maps of a CdS/P3HT heterojunction acquired at b) 633 nm and c) 488 nm. Panel d) shows possible charge transfers upon illumination and panel e) band diagrams of the heterojunction for an undoped (left) and doped (right) CdS nanowire.

A tentative explanation of the different behaviours involves the following model. At 633 nm (1.96 eV) only the P3HT is excited, as it has a smaller bandgap ($E_{g,\text{P3HT}} = 1.9$ eV) than CdS ($E_{g,\text{CdS}} = 2.4$ eV [94]). As depicted in figure 6.5.d, electrons excited in the P3HT are transferred into the CdS, while the holes are transported along the polymer to the gold electrode. To separate charge carriers in polymers the exciton binding energy has to be overcome (see section 2.2.1). Hence a certain band bending is required at an interface to separate charge carriers.

Figure 6.5.e shows that the band bending at the CdS/P3HT heterojunction depends on the doping level of the nanowire. At a higher doping, the Fermi levels of both materials differ more, leading to a larger potential step at the junction. In the device of figure 6.5, the nanowire is locally doped in the titanium contact region. Probably only in this region the band bending is strong enough to separate charge carrier at the CdS/P3HT interface. As the exciton dissociation is the limiting step, it determines the spatial photocurrent distribution leading to a photocurrent maximum at the electrode (figure 6.5.b). Excitons which are excited at 488 nm in the CdS NW dissociate already at room temperature. As a consequence, the separation of charge carriers in this material is less dependent on the band bending, which would account for the constant photoresponse along the nanowire in figure 6.5.c.

7 Field-stimulated exciton dissociation

7.1 Limitations of bulk heterojunction solar cells

State-of-the-art bulk heterojunction solar cells attain efficiencies of 7.4% [33] and internal quantum efficiencies of 100 % [32]. Their high performance is due to their morphology (see section 2.2.1), which allows almost every exciton to dissociate at an interface. Despite this advantage, the charge transport in these devices is not very effective, which demands the fabrication of nanostructured solar cells. However, achieving such tiny structures like in bulk heterojunctions by nanoscale patterning of inorganic electrodes still poses a great challenge.

In this chapter an alternative approach is discussed, which aims at electric field-assisted exciton dissociation within a solar cell. First, some general aspects of photophysics in polymers are presented, followed by first experimental efforts to realize an electrostatic gated pn-homojunction in the π -conjugated polymer P3HT.

7.2 The Onsager-Braun model of exciton dissociation

Upon absorption of a photon in a semiconductor, an electron-hole pair is created and both charges feel their mutual Coulomb attraction. To separate them, additional energy is necessary which is denoted as the exciton binding energy E_b . Depending on the type of semiconductor there are different types of excitons.

In inorganic semiconductors, so called Wannier-Mott excitons have a low binding energy of around 10 meV. The high dielectric constant of most inorganic semiconductors (e.g., $\epsilon_{Si} = 11.7$, $\epsilon_{CdS} = 8.7$) substantially screens the Coulomb attraction. Since this reduces the force acting on the charge carriers, their distance becomes larger and the binding energy decreases. In general, these excitons already dissociate due to the thermal energy at room temperature

($kT \approx 25$ meV) and hence play no significant role in solar cells made of inorganic semiconductors.

In contrast, organic semiconductors have much lower dielectric constants ($\epsilon_{P3HT} = 3.0$). Thus the exciton binding energy is larger ($E_b \approx 1$ eV) and so called Frenkel type excitons are formed. The strong attraction of electrons and holes is ideal for organic light emitting diodes (OLED) since it allows an efficient recombination of the injected charge carriers. However, in solar cells it impedes the charge separation. As a consequence, it is important to gain a better understanding of the exciton dissociation processes in organic materials.

7.2.1 Charge transfer states in π -conjugated polymers

Upon absorption of a photon, an electron is excited from the HOMO to the LUMO of a polymer chain. To obtain free charge carriers, either the hole or the electron must be transferred to an adjacent polymer chain. This reduces the Coulomb interaction, but to get free charge carriers this process has to be repeated multiple times. Electron-hole pairs which are not residing on the same molecule or polymer chain, but which still feel a Coulombic attraction are called geminate pairs. Their existence is a major difference to inorganic solar cells where the charges of dissociated excitons can freely move through the whole crystal. In organic solar cells geminate pairs can still recombine and significantly contribute to the losses in solar cells [121]. Such losses should not be confused with the recombination of free charges which is termed bimolecular recombination.

The separation of charges in organic polymers is preceded by the formation of charge transfer states (CT), like at the heterojunction in bulk solar cells. Charge carriers can tunnel into available energy levels inside the neighbouring material before the exciton decays. A compound which is often used as acceptor and readily forms charge transfer states with P3HT is PCBM. The electron affinity of PCBM is around 1 eV larger than for P3HT, rendering it into a very efficient quencher.

Apart from heterojunctions, charge transfer states also exist in the material itself. This arises partially from impurities remaining from the synthesis. As an example, table 7.1 lists impurities commonly found in P3HT. In addition, adsorbed oxygen can form a charge transfer state in

Element	$\mu\text{gr}/\text{gr}$	$(1/\text{cm}^3)$	Element	$\mu\text{gr}/\text{gr}$	$(1/\text{cm}^3)$
Zn	150.0	1.5×10^{18}	Fe	10.0	1.2×10^{16}
Ca	50.0	8.3×10^{17}	Mg	3.0	8.2×10^{16}
Ni	60.0	6.7×10^{17}	Ti	3.0	4.1×10^{16}
Al	5.0	1.2×10^{17}	Ba	5.0	2.4×10^{16}

Table 7.1: List of impurities found by element analysis in P3HT.

P3HT. As a consequence, P3HT films with a lower oxygen content show a stronger photoluminescence [122]. However, even in pure polymer samples CT states exist. In the simplest case, the polymer chains are so close together that the Coulomb binding energy of an electron-hole pair occupying these molecules exceeds the exciton binding energy [29]. Defects in the polymer chain or the crystal order can have the same effect.

In organic materials, E_b is defined as the sum of the binding energy of an electron-hole (e-h) pair (the actual exciton) and the energy needed to create a charge transfer state. Without CT centers excitons could not dissociate at room temperature in an organic material.

7.2.2 Field-assisted exciton dissociation

In inorganic materials the exciton dissociation generally cannot be influenced by an external electric field (unless at very low temperatures). By contrast, in organic materials geminate e-h pairs can be separated by the action of such fields. As a rough estimate, the displacement of a charge by 1 nm in a field of 400 MV/m corresponds to an electrostatic energy of 0.4 eV which is roughly the exciton binding energy in P3HT.

The dissociation probability Ψ of an excitation in an electric field is described by the Onsager-Braun model. Onsager calculated the probability that a pair of oppositely charged ions in a weak electrolyte would escape recombination [123]. In this model, the ions perform a three-dimensional Brownian random walk under the influence of their mutual Coulomb attraction and an external electric field. Braun extended the model by incorporating finite lifetimes of the e-h pairs [124]. The dissociation probability is expressed by the following three rate constants k_F , $k_D(E)$, and k_R . A geminate e-h pair can recombine to the ground state (k_F) or be separated into free carriers ($k_D(E)$). Already separated pairs can form a new pair at the rate of k_R . $k_D(E)$ can be calculated from:

$$k_D(E) = k_R \frac{3}{4\pi r^3} e^{-E_b/kT} \left[1 + b + \frac{b^2}{3} + \frac{b^3}{18} + \frac{b^4}{180} + \dots \right] \quad \text{with} \quad b = \frac{e^3 E}{8\pi \epsilon k^2 T^2} \quad (7.1)$$

where r is the initial distance of the eh-pair, E is the external electrical field, e is the elementary charge, ϵ is the dielectric constant of the material, k is the Boltzman constant and T the temperature. The constant k_R follows from the Langevin equation as $k_R = e\mu_{eh}/\epsilon_0\epsilon_r$ [125] where μ_{eh} is the averaged sum of the hole and electron mobilities. The dissociation probability Ψ can be expressed by the three rate constants as follows:

$$\Psi = \frac{k_D(E)}{k_D(E) + k_F} \quad (7.2)$$

This relation has been extensively used to describe exciton dissociation. It explains well the measured field-dependent dissociation probability in various materials and provides for a reasonable estimate of the exciton binding energy. However, it should only be regarded as a rough approximation since it does not fully account for the underlying physics. For example, it does not consider the excitation wavelength or the crystallinity of the material. Hot excitons with a large excess energies create phonons upon relaxation. These phonons can contribute to the exciton dissociation, giving a higher yield at short wavelength [126]. Furthermore, the alignment of the energy levels in polymers depends sensitively on the crystallinity, which in turn affects the efficiency of exciton dissociation by CT states. It has been shown that the exciton dissociation is more efficient at higher disorder which broadens the energy distribution of CTs states. Thus, the probability that a charge finds a suitable energy level to tunnel into is higher [127].

7.3 SPCM-based experiments

There exist numerous methods to measure the exciton dissociation probability, including photoluminescence quenching [128], time-resolved microwave conductivity technique (FP-TRMC) [129], or photoinduced absorption (PIA) spectroscopy [130]. These elaborate methods have been optimized to avoid measurement errors due to charge injection or exciton quenching at the electrodes. Here, we use a photoconduction experiment to study the exciton dissociation in P3HT films. Compared to the methods mentioned above, this approach is somewhat less accurate, but it is directly related to the development of novel photovoltaic devices.

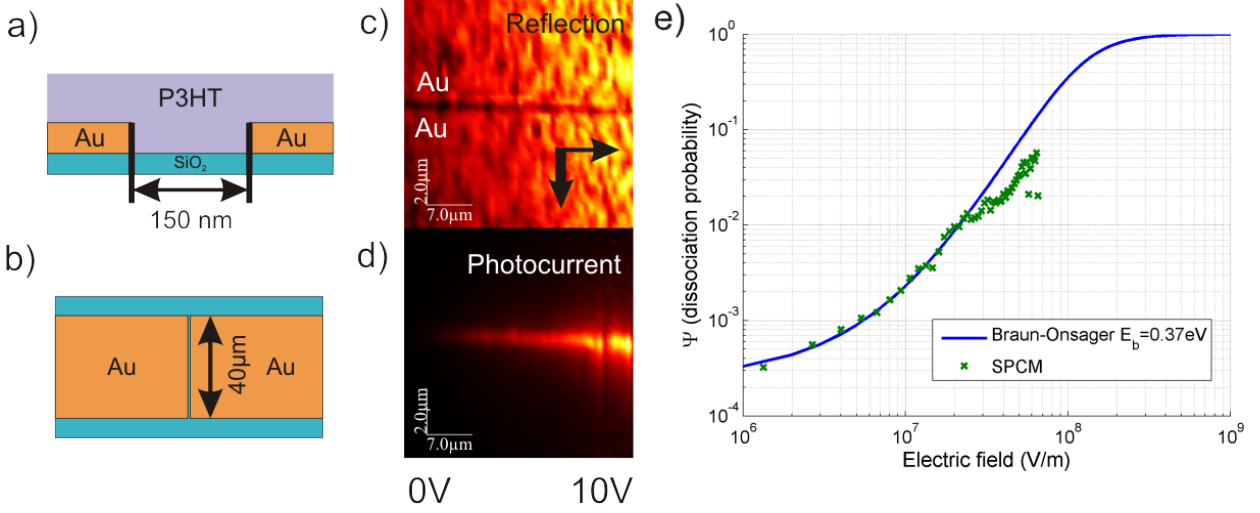


Figure 7.1: a) Side and b) top view of the device consisting of two gold electrodes with 150 nm spacing. SPCM measurement gives c) the reflection and d) photocurrent map of such a device. The bias is increased at every vertical line scan from 0 to 10 V. Panel e) shows the current detected at the center of the electrode gap (green points), in dependence of the electrical field. For comparison the calculated dissociation probability given by the Onsager-Braun model is also plotted (blue curve).

The high electrical fields necessary to dissociate the excitons were obtained by small gaps between metal contacts. To this end, gold electrodes with a spacing of $d = 150$ nm and a width of $40\ \mu\text{m}$ were defined by e-beam lithography, as schematically illustrated in figure 7.1.a and 7.1.b. At an applied bias of 10 V, this gives an electric field of $E = V/d = 70$ MV/m. On top of the electrodes a layer of P3HT was spin coated. Figure 7.1.c shows the reflection image of a completed device. The horizontal line in the middle of the image is the gap between both gold electrodes. Figure 7.1.d displays the corresponding photocurrent map, obtained by increasing the bias between the electrodes stepwise from 0 V to 10 V at each measured vertical line. To eliminate the dark current, the measurements were performed with a lock-in amplifier combined with a chopper in the light path of the microscope. Figure 7.1.d reveals a sizeable conductivity at the location of the gap, which increases with the applied bias. Since there is normally no photoresponse at the gold/P3HT contacts this current is attributed to the intrinsic photoconductivity of the P3HT. In figure 7.1.e, the normalized photocurrent (green points) in the electrode gap is plotted as a function of the electric field. For comparison, the blue curve

is calculated from the Onsager-Braun model. A fit of the curve parameters gives an exciton binding energy of 0.37 eV. It is furthermore apparent that the electric field would have to be increased by an order of magnitude to fully separate the excited excitons.

7.4 Split gate solar cells

Since it is possible to separate electron-hole pairs by electric fields, it should also be feasible to design a device wherein these separated charges are collected. One approach is the split gate structure proposed in figure 7.2. Similar electrostatic gated pn-junctions in photodetectors or solar cells have already been realized with materials like graphene [131] or CNTs [132, 133]. Split gates were already used to implement simple logic circuits with polymers [134]. There are several potential advantages of such a structure compared to bulk heterojunction cells. Firstly, charge carriers are spatially separated inside the electrode gap and then transported to different directions. This should reduce losses due to bimolecular recombination. Secondly, the device can be designed such that the electrical field extends over distances (here 150 nm) which are much larger than the exciton diffusion length (5-10 nm). This greatly reduces the need of nanostructuring, and would in principle allow to obtain thicker solar cells. Finally, it enables control over the exciton dissociation process while the device can be operated in different regimes like accumulation or depletion.

In figure 7.2, the same arrangement of the gold electrodes as in figure 7.1 now acts as a split gate with the bottom electrodes V_{gs} and V_{gd} . The gold was covered with 30 nm of Al_2O_3 by atomic layer deposition (ALD). On top of the aluminium oxide, a monolayer of octadecylphosphonic acid [135] was self-assembled onto the Al_2O_3 . Free hydroxyl groups on the oxide would act as electron traps, and may hence shield an applied positive gate voltage. Chua et al. showed that by using SAMs as dielectrics even n-type FETs can be realized with P3HT [136]. The top electrodes V_s and V_d are devised to collect the photocurrent of the separated charges. Finally, a layer of P3HT was spin coated onto the device.

7.5 Gate penetration depth in split gate devices

Carbon nanotubes on top of split gates [132, 133] show diode-like current voltage characteristics and a distinct photoresponse under illumination. As CNTs have an inherently surface-like

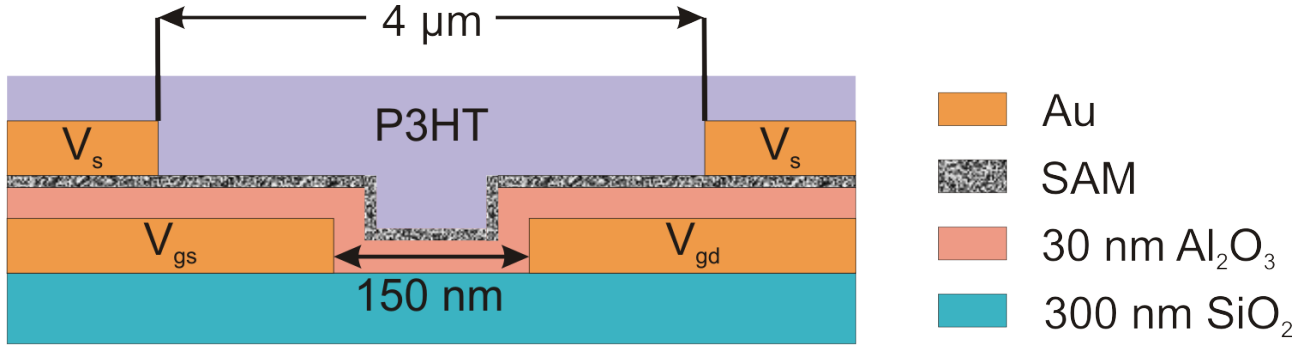


Figure 7.2: Schematic representation of a split-gate solar cell. In the ideal case, the application of a different bias to V_{gs} and V_{gd} a strong electric field separates geminate pairs in the P3HT. These charges are collected at the electrodes V_s and V_d .

conduction, the gate directly controls the transport in the nanotube. The situation is different in a bulk material (like the present P3HT films) where the gate only penetrates partly into the material.

Two-dimensional FEM calculations (see section 2.1.1 and 3.2) were performed to estimate the penetration depth into the split-gate structure, and to ensure that the electric field is high enough. In figure 7.3, the obtained potential map (a), electric field (b) and charge carrier density of electrons (c) and holes (d) are displayed. An untreated spin cast film of P3HT has a hole carrier density of the order of 10^{18} cm^{-3} [137]. As figure 7.3.a shows, the potential and the electric field extends only a few nanometers into the semiconductor at such high doping levels. This leads to a very weak charge accumulation in the p-region ($V_{gd} = -3 \text{ V}$) and a thin depletion layer in the n-region ($V_{gs} = 3 \text{ V}$) which is efficiently screened by negatively filled acceptor states. Even if excitons could dissociate in this thin layer, the large amount of holes would cause strong recombination with electrons so that no photocurrent would flow.

To increase the penetration depth of the gate the charge carrier density has to be decreased. Since P3HT is strongly p-doped by oxygen from the ambient it is possible to significantly reduce the doping concentration via oxygen removal (see next section 7.6). Figure 7.4 shows the same device for a low doping level of 10^{12} cm^{-3} obtained in this manner. In this case the electric field can penetrate the whole sample, resulting in a defined pn-junction according to the calculation.

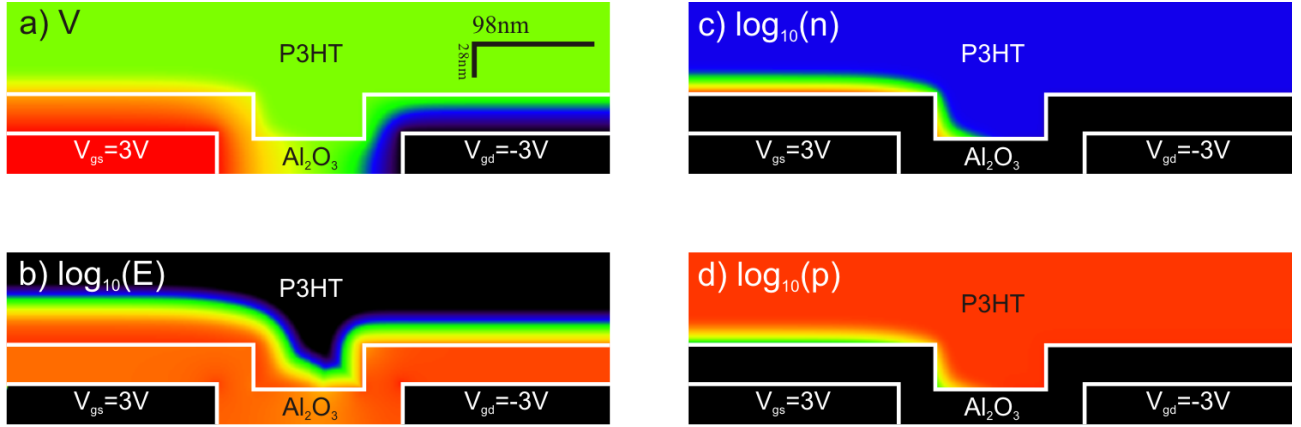


Figure 7.3: Two-dimensional FEM calculation for a split-gated, p-doped (10^{18} cm^{-3}) P3HT film. Calculated a) potential map, b) electric field, c) and d) electron and hole concentration, respectively.

However, the above calculations do not consider charge injection from the electrodes, although this is an important factor in organic semiconductors. In undoped organic FETs the charges along the channel are injected from the contacts. This injection is expected to also play a role in split-gate devices, i.e., to lead to a similar charge distribution as in figure 7.3. To avoid this problem the device can be driven into depletion by applying positive gate voltages. Under this condition, the top gold (or titanium) contacts cannot inject electrons into the P3HT due to the difference between the metal Fermi level and the LUMO level of the P3HT. By keeping a potential difference between the gates (for example $V_{gs} = 5 \text{ V}$ and $V_{gd} = 1 \text{ V}$), one hence, should be able to attain a high electric field while keeping the semiconductor in a depleted state.

7.6 Undoping of P3HT by oxygen desorption

The major doping mechanism in P3HT is via reversible adsorption of oxygen on the polymer chains. There are different methods to remove the oxygen, either by exposure to a gas phase saturated with TDAE [138] or by annealing in vacuum [139]. In this manner, the doping concentration can be reduced by several orders of magnitude. The dedoping and redoping (by oxygen exposure) are both very slow processes. However, the combination of oxygen and light dramatically increases the redoping speed and even damages the material [139]. Therefore, the

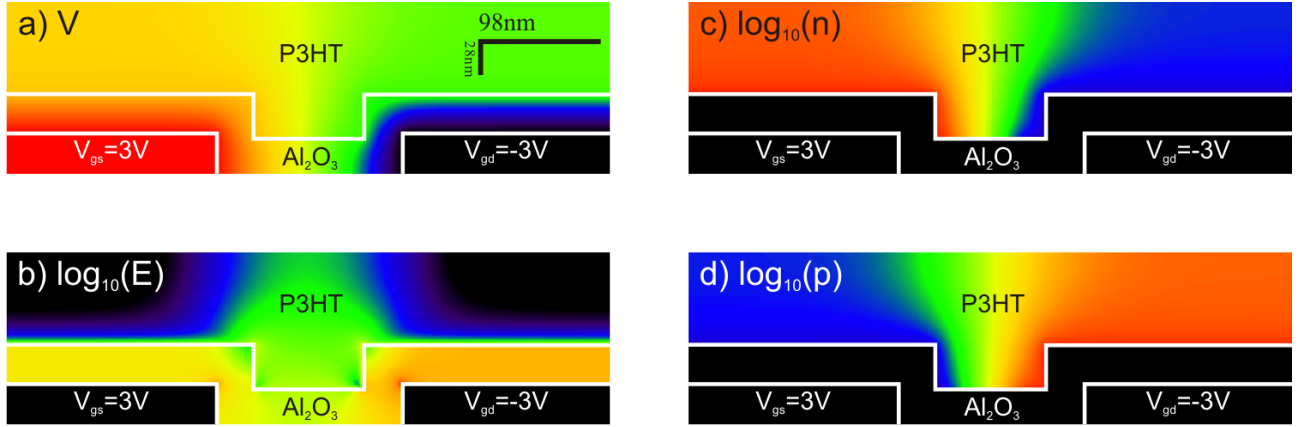


Figure 7.4: Two-dimensional FEM calculation for a split-gated, dedoped (10^{12} cm^{-3}) P3HT film. Calculated a) potential map, b) electric field, c) and d) electron and hole concentration, respectively.

dedoping is not only important to reduce the hole density but also to make the samples stable against light exposure.

In this work, we use annealing in vacuum to dedope the P3HT. To measure the resulting doping concentration, 4-point resistance measurements were performed. Figure 7.5 shows the gate dependent current through a P3HT film, measured under high vacuum ($p = 10^{-6} - 10^{-9} \text{ mbar}$) at a temperature of 125°C . The first curves (in blue) show only a weak gating effect due to the high doping. After 20 hours most of the oxygen is desorbed, as reflected by a much stronger gate dependence.

Figure 7.6 shows the transfer- (a) and output-characteristic (b) after 20 hours of dedoping the P3HT film. At $V_{gs} = 0 \text{ V}$ the current closely approaches zero, indicating that the semiconductor is nearly intrinsic.

7.7 SPCM on split gate devices

Figure 7.7 shows the current-voltage curve of a fully dedoped P3HT split gate device. For both gates at 0 V , a nearly linear relationship is observed (blue curve). The small asymmetry

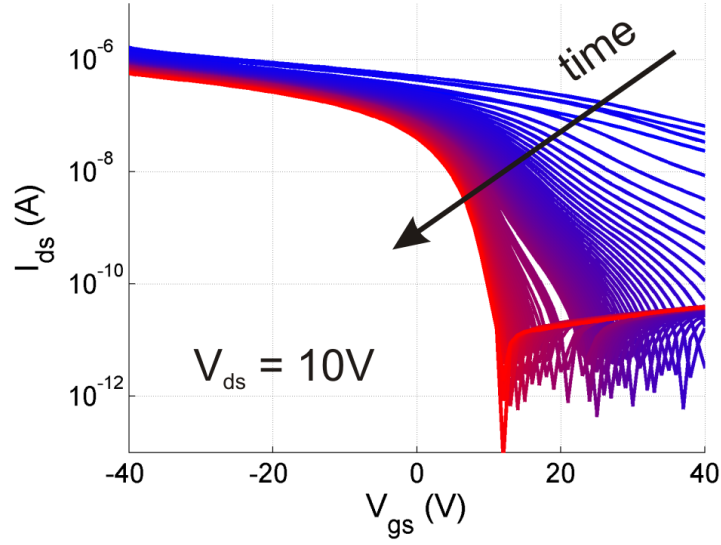


Figure 7.5: Transfer characteristic of a P3HT FET under annealing at 125°C in HV for 20 hours.

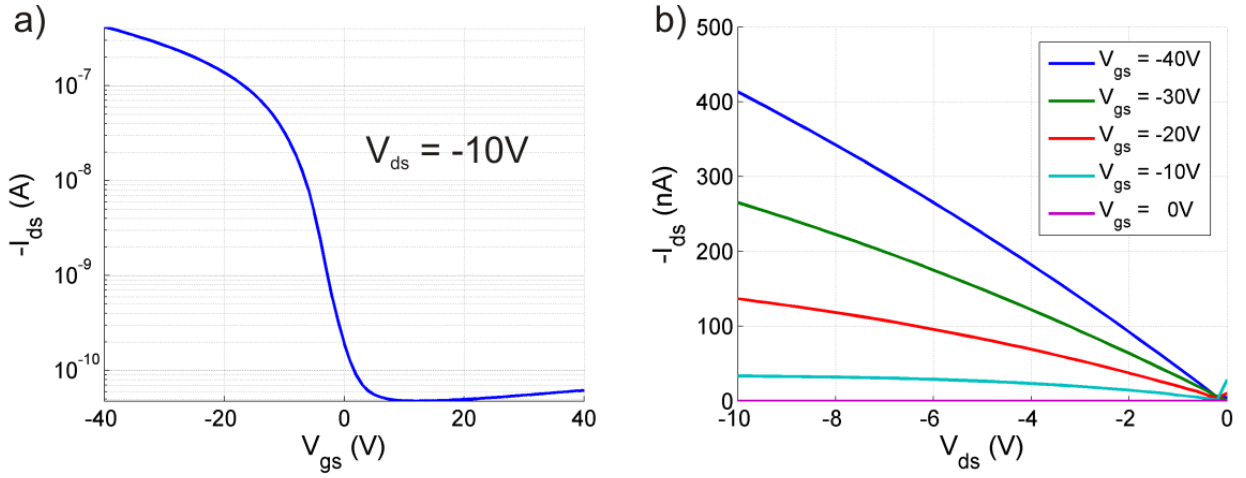


Figure 7.6: Transfer a) and output b) characteristic of a dedoped P3HT field effect transistor ($W=400 \mu m$, $L=10 \mu m$).

is probably due to different contact resistances at the electrodes. Upon gating, a diode-like behaviour emerges which proves that the charge carrier density is influenced by the field-effect in the device.

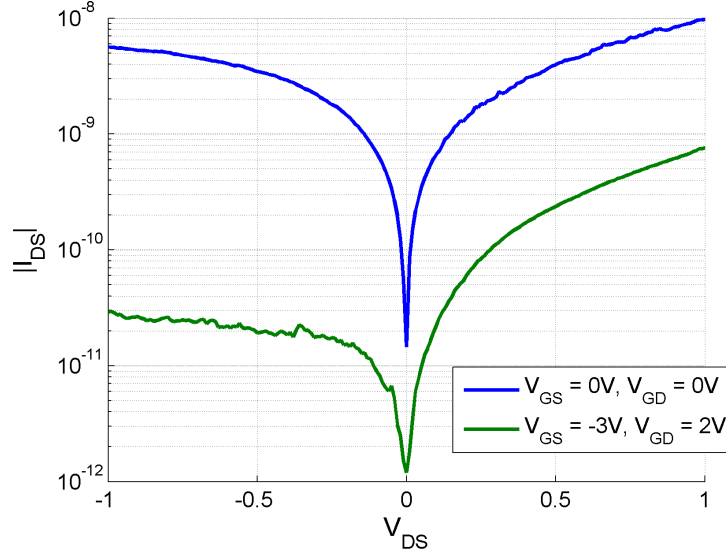


Figure 7.7: Current-voltage curves acquired between source and drain contact of a dedoped P3HT device. At $V_{gs} = V_{gd} = 0$ V the device shows a linear resistance, while at $V_{gs} = -3$ V and $V_{gd} = 2$ V a diode characteristic appears.

In figure 7.8, a series of SPCM images of the same dedoped split gate device are presented. Since the P3HT film is dedoped, the measurements were carried out under argon atmosphere (ensuring that even after several measurements no degradation could be observed). The photocurrent maps (b-f) were measured under different split gate bias configurations. In panel b) and c) the gate voltage generates an electric field above 10^7 V/m, which should be sufficient to separate a significant amount of charge carriers (compare with figure 7.1.e). However, there is no distinguishable photoresponse at the position of the split gate gap. Only the edges of the top gold contacts display a significant photocurrent, which increases upon accumulation of holes. Normally, as described for the $\text{TiO}_2/\text{P3HT}/\text{Au}$ solar cells (section 6), the gold electrodes do not show a photoresponse (even in the dedoped case). It is hence concluded that the photocurrent at the edges must have a different origin than the ones described in the previous chapters. Conventional Schottky contacts can be ruled out, since the photoresponse would not be confined to the edges, but extend across the whole electrode. Instead, we attribute the edge signal to the Seebeck effect. At 633 nm, the P3HT film absorbs ≈ 37 % of the incident light (calculated by Beer's law with $\alpha = 10^5 \text{ cm}^{-1}$). This causes local heating of the material, producing a temperature gradient which due to the Seebeck effect generates an electrical field:

$$\vec{E} = S \cdot \nabla T \quad (7.3)$$

where S is the Seebeck coefficient, T the temperature, and \vec{E} the electric field. The generated electric field will accumulate the holes in the hot region. Under equilibrium conditions, this accumulation of holes will be counterbalanced by a diffusion current. Due to conservation laws, both currents have to cancel each other out. Importantly, this balance is broken when the laser spot crosses the edge of a contact. At this point the generated electric field drives holes toward the electrode resulting in a measurable net current. When the laser spot has moved further onto the contact, again both currents cancel each other out. By considering the local Ohmic law $\vec{J}_h = \sigma_h \cdot \vec{E}$ with $\sigma_h = q \cdot p \cdot b_h$, the influence of the gate can be understood as a consequence of the higher total current that originates from an enhanced charge carrier density. In solar cells like $\text{TiO}_2/\text{P3HT}/\text{Au}$ this effect is not observable because the TiO_2 layer blocks the holes coming from the gold electrode.

In order to observe a photoresponse inside the gap of the split gate, similar measurements have been performed for different electrode arrangements and bias voltages. Instead of two gold electrodes, combinations of one gold and one titanium electrode were used, since the gold electrodes could form a Fermi-level-dependent electron barrier and thereby block the transport. In another attempt, the gate bias was increased to dissociate more excitons. However, neither under depletion nor accumulation conditions, a photocurrent could be observed between the gates.

A plausible explanation why these split gate devices did not work is the limited electron transport in P3HT. An important figure of merit of a material is the $b \cdot \tau$ product, from which important properties like the diffusion length can be directly derived. The mobilities in polymers are generally low (at maximum $0.1 \text{ cm}^2/\text{Vs}$). To nevertheless achieve reasonable values for $b\tau$ the charge carrier lifetime has to be increased. Even though the hydroxyl groups at the dielectric were coated by a SAM, there could still be a high trap density in the bulk material. An indication that this may indeed be the case derives from the elemental analysis performed by inductively coupled plasma optical emission spectrometry (ICP-OES) of P3HT (see table 7.1).

The most abundant impurity is zinc, which probably occurs as ZnO in the material. ZnO is a good electron acceptor and thus is likely to act as an efficient electron trap. This poses a

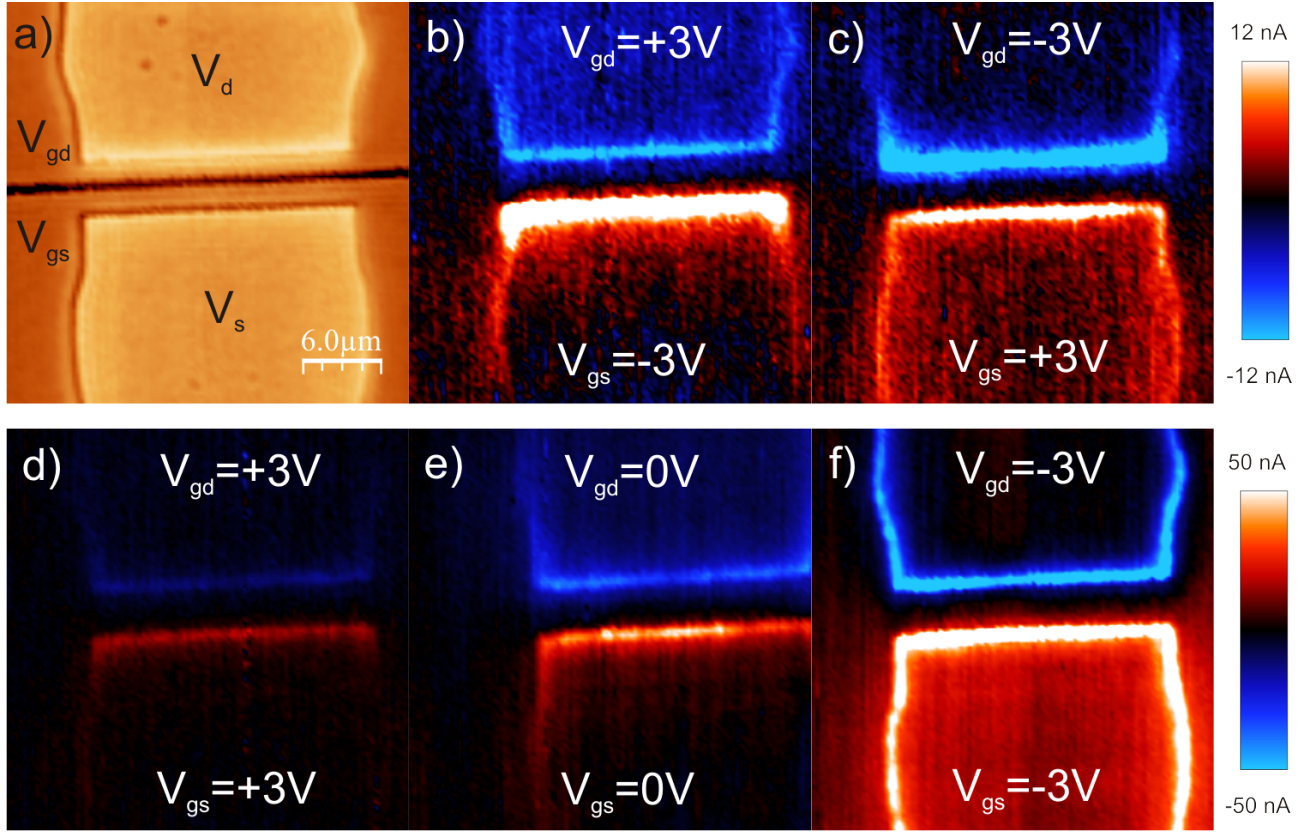


Figure 7.8: a) Reflection image of P3HT split gate device. The blurred horizontal line in the center of the image is the gap of the split gate. On top are the source V_s and V_d contact. The entire surface is covered by P3HT. b-f) Photocurrent maps recorded at different split gate voltage combinations.

general problem, since due to the low electron affinity of P3HT (3 eV) nearly all impurities will act as such traps. To compensate the limited diffusion length, the distance between the top gold electrodes could be decreased. However, the distance would become so small that the top electrodes would screen the split-gates. As another consequence, it would not be possible any more to resolve optically the origin of the photoresponse.

8 Summary and outlook

In thesis, scanning photocurrent microscopy (SPCM) was used to study different types of nanoscale lateral photojunctions whose properties are relevant for the charge separation mechanisms in common bulk solar cells. The obtained results demonstrate that the SPCM technique provides convenient access to the spatial electric field distributions or diffusion lengths in such devices. As one type of photoactive junction, gold/CdS-nanowire Schottky-contacts were explored. The SPCM measurements revealed different regions of transport (drift- and diffusion-dominated) along the nanowire. Finite element (FEM) calculations of the potential distribution along the contact region revealed the presence of strong electric fields (1 MV/m) along the radial and axial directions with respect to the nanowire. The shape of these field distributions was found to depend on the geometric nanowire/electrode arrangement. In particular, while the radial field component separates excited electron-hole pairs and effectively suppresses charge recombination, the axial field component only penetrates for 1 μm inside the contact region. Upon illumination, the axial electric field drives a drift current, which allows a nearly lossless charge carrier extraction out of the contact. This effect may be exploited to improve the performance of solar cells or photodetectors by concentrating the incident light to the region of efficient charge extraction. In addition, evaluation of the diffusion currents below the gold contact enabled determining the recombination losses in the nanowires due to the presence of the metal electrode. The SPCM experiments provided evidence that the application of a gate or bias voltage to the Schottky-contacts only affects the radial electric field, thereby modulating the recombination rates within the gold-coated wire section. On this basis, it became furthermore possible to separate intrinsic and contact related recombination rates.

A second topic involved the separation of electron-hole pairs that are generated upon photo-illumination of the interface between graphene and a CdS nanowire. The spatial distribution and magnitude of this photocurrent signal could be controlled through chemical modification of the graphene/CdS interface, comprising stabilization of the nanowire surface with an organic thiols and a subsequent annealing step to remove remaining contaminations. Moreover,

the SPCM measurements revealed a surface plasmon contribution to the photocurrent. This effect was exploited in nanoscale, electrical detectors for surface plasmon polaritons (SPP). These devices are based upon launching of SPPs at a small grating, from where they propagate several micrometers along an aluminium stripe. The detector is a CdS Schottky contact, which is placed in the near-field of the surface plasmon. Polarization-dependent measurements on the grating confirmed the excitation of surface plasmons. Upon incorporation of a metal-insulator-metal (MIM) structure into the detector device, the polarization-dependent excitation of surface plasmons changed significantly. This is due to the excitation of transversal electric modes, which are supported by the MIM structure, but do not exist at metal-dielectric interfaces. By comparing the obtained SPCM data with finite-difference time domain (FDTD) calculations, the influence of the geometry on the coupling efficiency could be determined. In general, nanoscale electrical detection of surface plasmons is important for the integration of plasmonics in existing semiconductor technologies. A promising future direction might be the study of Si/CdS nanowire junctions, from which efficient avalanche diodes have been made [54]. Another interesting approach is the detection of phase information of surface plasmons. This task may be achieved by applying a bias in order to alter the depletion width of the Schottky contact and accordingly the photoactive area. In this manner, it would be possible to probe the spatial intensity modulation of the standing plasmonic waves, which in turn provides access to the phase information of the light signal. However, this objective would require a very well-defined behaviour of the contact, which is especially difficult to achieve with nanowires.

Another focus was on the spatially resolved photoresponse of hybrid solar cells composed of poly(3-hexylthiophene) (P3HT), titanium dioxide (TiO_2), and cadmium selenide (CdSe) nanoparticles. In a first step, the fabrication of thin and dense films of TiO_2 was optimized. SPCM measurements on TiO_2 /P3HT/Au devices revealed a photoresponse along the TiO_2 electrode, but no signal at the gold electrode. In these devices, the photocurrents were found to be nearly independent of the electrode distance, demonstrating that the transport along the P3HT is not a limiting factor. In a second step, a layer of CdSe nanoparticles was incorporated in the devices to clarify the extent to which its conductivity limits the device performance. The layer could be rendered sufficiently conductive by exchanging the ligands on the nanoparticle surface. Thus modified devices behaved similar to hybrid solar cells made of blends [35]. A related approach was used to obtain CdS nanowire/P3HT heterojunctions as a model system for nanostructured solar cells. Selective optical excitation of the CdS nanowire or the P3HT component enabled to spatially resolve the electron (hole) injection into the nanowire (polymer).

These two injection processes were observed to be differently distributed along the nanowire, which likely originates from the localized doping of the nanowire contacts. Further elucidation of the underlying mechanism requires further experiments with varying doping profiles along the nanowire.

Finally, the electric field-assisted exciton dissociation in P3HT was studied. Upon electrical biasing small (150 nm width) electrode gaps, electric fields of 70 MV/m were generated, sufficiently large to dissociate excitons inside the organic polymer, as demonstrated by SPCM photoconduction experiments. The measured electric field dependence agrees well with the Onsager-Braun model of charge separation, which allows determining the exciton binding energy to 0.37 eV. On this basis, a split gate structure was designed with the aim to fabricate a photovoltaic device. To this end, additional electrodes were structured on top of the split gate to collect the free charges of the dissociated excitons. Although different material combinations and electrode arrangements were tested, no measurable photocurrent could be detected at the split gate gap. The only apparent signal occurred at the edges of the gold electrodes, and could be explained by a photothermal (Seebeck) effect. The realization of true photovoltaic devices that rely upon such type of exciton dissociation would require the use of other materials than P3HT, which exhibit ambipolar charge transport behaviour. A promising candidate would be poly(9,9-di-n-octylfluorene-alt-benzothiadiazole) (F8BT) which besides its well-established ambipolar transport, shows an intense photoluminescence [140].

Bibliography

- [1] J. F. Geisz. 40.8% efficient inverted triple-junction solar cell with two independently metamorphic junctions. *Applied Physics Letters*, 93(12):123505– (2008). doi:[10.1063/1.2988497](https://doi.org/10.1063/1.2988497).
- [2] L. Qi, H. Coelfen, and M. Antonietti. Synthesis and Characterization of CdS Nanoparticles Stabilized by Double-Hydrophilic Block Copolymers. *Nano Letters*, 1(2):61–65 (2000). doi:[10.1021/nl0055052](https://doi.org/10.1021/nl0055052).
- [3] A. L. Rogach, A. Kornowski, M. Gao, A. Eychmueller, and H. Weller. Synthesis and Characterization of a Size Series of Extremely Small Thiol-Stabilized CdSe Nanocrystals. *Journal of Physical Chemistry B*, 103(16):3065–3069 (1999). doi:[10.1021/jp984833b](https://doi.org/10.1021/jp984833b).
- [4] M. S. Gudixsen, L. J. Lauhon, J. Wang, D. C. Smith, and C. M. Lieber. Growth of nanowire superlattice structures for nanoscale photonics and electronics. *Nature*, 415(6872):617–620 (2002). doi:[10.1038/415617a](https://doi.org/10.1038/415617a).
- [5] Y.-w. Jun, S.-M. Lee, N.-J. Kang, and J. Cheon. Controlled Synthesis of Multi-armed CdS Nanorod Architectures Using Monosurfactant System. *Journal of the American Chemical Society*, 123(21):5150–5151 (2001). doi:[10.1021/ja0157595](https://doi.org/10.1021/ja0157595).
- [6] J.-C. Lee, W. Lee, S.-H. Han, T. G. Kim, and Y.-M. Sung. Synthesis of hybrid solar cells using CdS nanowire array grown on conductive glass substrates. *Electrochemistry Communications*, 11(1):231–234 (2009). doi:[10.1016/j.elecom.2008.11.021](https://doi.org/10.1016/j.elecom.2008.11.021).
- [7] E. J. H. Lee, K. Balasubramanian, R. T. Weitz, M. Burghard, and K. Kern. Contact and edge effects in graphene devices. *Nat Nano*, 3(8):486–490 (2008). doi:[10.1038/nnano.2008.172](https://doi.org/10.1038/nnano.2008.172).
- [8] J. Carstensen, G. Popkirov, J. Bahr, and H. Foell. CELLO: an advanced LBIC measurement technique for solar cell local characterization. *Solar Energy Materials and Solar Cells*, 76(4):599–611 (2003). doi:[10.1016/S0927-0248\(02\)00270-2](https://doi.org/10.1016/S0927-0248(02)00270-2).

-
- [9] M. Rinio, H. J. Moeller, and M. Werner. LBIC investigations of the lifetime degradation by extended defects in multicrystalline solar silicon. *Solid State Phenomena*, 63-64:115–122 (1998). doi:[10.4028/www.scientific.net/SSP.63-64.115](https://doi.org/10.4028/www.scientific.net/SSP.63-64.115).
- [10] O. Breitenstein, J. Bauer, and J. Rakotoniaina. Material-induced shunts in multicrystalline silicon solar cells. *Semiconductors*, 41(4):440–443 (2007). doi:[10.1134/S106378260704015X](https://doi.org/10.1134/S106378260704015X).
- [11] M. Acciarri, S. Binetti, A. Racz, S. Pizzini, and G. Agostinelli. Fast LBIC in-line characterization for process quality control in the photovoltaic industry. *Solar Energy Materials and Solar Cells*, 72(1-4):417–424 (2002). doi:[10.1016/S0927-0248\(01\)00189-1](https://doi.org/10.1016/S0927-0248(01)00189-1).
- [12] J. Cai and G. D. Mahan. Effective Seebeck coefficient for semiconductors. *Physical Review B*, 74(7):075201– (2006). doi:[10.1103/PhysRevB.74.075201](https://doi.org/10.1103/PhysRevB.74.075201).
- [13] P. Wuerfel. *Physics of Solar Cells*. Wiley-VCH (2009).
- [14] S. M. Sze and K. N. Kwok. *Physics of semiconductor devices*. Wiley-VCH (2007).
- [15] W. Shockley. Detailed Balance Limit of Efficiency of p-n Junction Solar Cells. *Journal of Applied Physics*, 32(3):510– (1961). doi:[10.1063/1.1736034](https://doi.org/10.1063/1.1736034).
- [16] G. Jellison. Optical absorption of silicon between 1.6 and 4.7 eV at elevated temperatures. *Applied Physics Letters*, 41(2):180– (1982). doi:[10.1063/1.93454](https://doi.org/10.1063/1.93454).
- [17] R. W. Birkmire and E. Eser. Polycrystalline Thin Film Solar Cells: Present Status and Future Potential. *Annual Review of Materials Science*, 27(1):625–653 (1997). doi:[10.1146/annurev.matsci.27.1.625](https://doi.org/10.1146/annurev.matsci.27.1.625).
- [18] J. Britt and C. Ferekides. Thin-film CdS/CdTe solar cell with 15.8% efficiency. *Applied Physics Letters*, 62(22):2851– (1993). doi:[10.1063/1.109629](https://doi.org/10.1063/1.109629).
- [19] W. Shafarman. Device and material characterization of Cu(InGa)Se₂ solar cells with increasing band gap. *Journal of Applied Physics*, 79(9):7324– (1996). doi:[10.1063/1.361431](https://doi.org/10.1063/1.361431).
- [20] M. A. Contreras, B. Egaas, K. Ramanathan, J. Hiltner, A. Swartzlander, F. Hasoon, and R. Noufi. Progress toward 20% efficiency in Cu(In,Ga)Se₂ polycrystalline thin-film solar cells. *Progress in Photovoltaics: Research and Applications*, 7(4):311–316 (1999). doi:[10.1002/\(SICI\)1099-159X\(199907/08\)7:4<311::AID-PIP274>3.0.CO;2-G](https://doi.org/10.1002/(SICI)1099-159X(199907/08)7:4<311::AID-PIP274>3.0.CO;2-G).

- [21] B. M. Basol. Electrodeposited CdTe and HgCdTe solar cells. *Solar Cells*, 23(1-2):69–88 (1988). doi:[10.1016/0379-6787\(88\)90008-7](https://doi.org/10.1016/0379-6787(88)90008-7).
- [22] D. Carlson. Amorphous silicon solar cell. *Applied Physics Letters*, 28(11):671– (1976). doi:[10.1063/1.88617](https://doi.org/10.1063/1.88617).
- [23] M. Pope and C. E. Swennberg. *Electronic Processes in Organic Crystals and Polymers*. Oxford University Press (1999).
- [24] H. Klauk (editor). *Organic Electronics, Materials, Manufacturing and Applications*. Wiley-VCH (2006).
- [25] J. H. Burroughes, D. D. C. Bradley, A. R. Brown, R. N. Marks, K. Mackay, R. H. Friend, P. L. Burns, and A. B. Holmes. Light-emitting diodes based on conjugated polymers. *Nature*, 347(6293):539–541 (1990). doi:[10.1038/347539a0](https://doi.org/10.1038/347539a0).
- [26] W. Bruetting, S. Berleb, and A. G. Mueckl. Device physics of organic light-emitting diodes based on molecular materials. *Organic Electronics*, 2(1):1–36 (2001). doi:[10.1016/S1566-1199\(01\)00009-X](https://doi.org/10.1016/S1566-1199(01)00009-X).
- [27] H. Hoppe and N. S. Sariciftci. Organic solar cells: An overview. *Journal of Materials Research*, 19:1924 (2004). doi:[10.1557/JMR.2004.0252](https://doi.org/10.1557/JMR.2004.0252).
- [28] J.-F. Chang, B. Sun, D. W. Breiby, M. M. Nielsen, T. I. Soelling, M. Giles, I. McCulloch, and H. Sirringhaus. Enhanced Mobility of Poly(3-hexylthiophene) Transistors by Spin-Coating from High-Boiling-Point Solvents. *Chemistry of Materials*, 16(23):4772–4776 (2004). doi:[10.1021/cm049617w](https://doi.org/10.1021/cm049617w).
- [29] V. I. Arkhipov and H. Baessler. Exciton dissociation and charge photogeneration in pristine and doped conjugated polymers. *Physica Status Solidi (a)*, 201:1152–1187 (2004). doi:[10.1002/pssa.200404339](https://doi.org/10.1002/pssa.200404339).
- [30] H. Najafov, B. Lee, Q. Zhou, L. C. Feldman, and V. Podzorov. Observation of long-range exciton diffusion in highly ordered organic semiconductors. *Nature Materials*, 9(11):938–943 (2010). doi:[10.1038/nmat2872](https://doi.org/10.1038/nmat2872).
- [31] G. Yu, J. Gao, J. C. Hummelen, F. Wudl, and A. J. Heeger. Polymer Photovoltaic Cells: Enhanced Efficiencies via a Network of Internal Donor-Acceptor Heterojunctions. *Science*, 270(5243):1789–1791 (1995). doi:[10.1126/science.270.5243.1789](https://doi.org/10.1126/science.270.5243.1789).

-
- [32] S. H. Park, A. Roy, S. Beaupre, S. Cho, N. Coates, J. S. Moon, D. Moses, M. Leclerc, K. Lee, and A. J. Heeger. Bulk heterojunction solar cells with internal quantum efficiency approaching 100%. *Nature Photonics*, 3(5):297–302 (2009). doi:[10.1038/nphoton.2009.69](https://doi.org/10.1038/nphoton.2009.69).
- [33] Y. Liang, Z. Xu, J. Xia, S.-T. Tsai, Y. Wu, G. Li, C. Ray, and L. Yu. For the Bright Future-Bulk Heterojunction Polymer Solar Cells with Power Conversion Efficiency of 7.4%. *Advanced Materials*, 22:E135–E138 (2010). doi:[10.1002/adma.200903528](https://doi.org/10.1002/adma.200903528).
- [34] Y. Kim, S. Cook, S. M. Tuladhar, S. A. Choulis, J. Nelson, J. R. Durrant, D. D. C. Bradley, M. Giles, I. McCulloch, C.-S. Ha, and M. Ree. A strong regioregularity effect in self-organizing conjugated polymer films and high-efficiency polythiophene:fullerene solar cells. *Nature Materials*, 5(3):197–203 (2006). doi:[10.1038/nmat1574](https://doi.org/10.1038/nmat1574).
- [35] W. U. Huynh, J. J. Dittmer, and A. P. Alivisatos. Hybrid Nanorod-Polymer Solar Cells. *Science*, 295:2425–2427 (2002). doi:[10.1126/science.1069156](https://doi.org/10.1126/science.1069156).
- [36] I. Lokteva, N. Radychev, F. Witt, H. Borchert, J. Parisi, and J. Kolny-Olesiak. Surface Treatment of CdSe Nanoparticles for Application in Hybrid Solar Cells: The Effect of Multiple Ligand Exchange with Pyridine. *Journal of Physical Chemistry C*, 114(29):12784–12791 (2010). doi:[10.1021/jp103300v](https://doi.org/10.1021/jp103300v).
- [37] A. C. Mayer, S. R. Scully, B. E. Hardin, M. W. Rowell, and M. D. McGehee. Polymer-based solar cells. *Materials Today*, 10(11):28–33 (2007). doi:[10.1016/S1369-7021\(07\)70276-6](https://doi.org/10.1016/S1369-7021(07)70276-6).
- [38] V. Kislyuk and O. Dimitriev. Nanorods and Nanotubes for Solar Cells. *Journal of Nanoscience and Nanotechnology*, 8(1):131–148 (2008). doi:[10.1166/jnn.2008.N16](https://doi.org/10.1166/jnn.2008.N16).
- [39] L. E. Greene, M. Law, B. D. Yuhas, and P. Yang. ZnO-TiO₂ Core-Shell Nanorod/P3HT Solar Cells. *Journal of Physical Chemistry C*, 111(50):18451–18456 (2007). doi:[10.1021/jp077593l](https://doi.org/10.1021/jp077593l).
- [40] Y.-Y. Lin, Y.-Y. Lee, L. Chang, J.-J. Wu, and C.-W. Chen. The influence of interface modifier on the performance of nanostructured ZnO/polymer hybrid solar cells. *Applied Physics Letters*, 94(6):063308– (2009). doi:[10.1063/1.3080203](https://doi.org/10.1063/1.3080203).

- [41] C. L. Huisman, A. Huijser, H. Donker, J. Schoonman, and A. Goossens. UV Polymerization of Oligothiophenes and Their Application in Nanostructured Heterojunction Solar Cells. *Macromolecules*, 37(15):5557–5564 (2004). doi:[10.1021/ma0357265](https://doi.org/10.1021/ma0357265).
- [42] K. Coakley, Y. Liu, M. McGehee, K. Frindell, and G. Stucky. Infiltrating Semiconducting Polymers into Self-Assembled Mesoporous Titania Films for Photovoltaic Applications. *Advanced Functional Materials*, 13(4):301–306 (2003). doi:[10.1002/adfm.200304361](https://doi.org/10.1002/adfm.200304361).
- [43] G. Boschloo and A. Hagfeldt. Characteristics of the Iodide/Triiodide Redox Mediator in Dye-Sensitized Solar Cells. *Accounts of Chemical Research*, 42(11):1819–1826 (2009). doi:[10.1021/ar900138m](https://doi.org/10.1021/ar900138m).
- [44] M. Wang, S.-J. Moon, D. Zhou, F. Le Formal, N.-L. Cevy-Ha, R. Humphry-Baker, C. Graetzel, P. Wang, S. M. Zakeeruddin, and M. Graetzel. Enhanced-Light-Harvesting Amphiphilic Ruthenium Dye for Efficient Solid-State Dye-Sensitized Solar Cells. *Advanced Functional Materials*, 20(11):1821–1826 (2010). doi:[10.1002/adfm.200902396](https://doi.org/10.1002/adfm.200902396).
- [45] S. R. Gajjela, K. Ananthanarayanan, C. Yap, M. Gratzel, and P. Balaya. Synthesis of mesoporous titanium dioxide by soft template based approach: characterization and application in dye-sensitized solar cells. *Energy & Environmental Science*, 3(6):838–845 (2010). doi:[10.1039/B921360K](https://doi.org/10.1039/B921360K).
- [46] M. Graetzel. Solar Energy Conversion by Dye-Sensitized Photovoltaic Cells. *Inorganic Chemistry*, 44(20):6841–6851 (2005). doi:[10.1021/ic0508371](https://doi.org/10.1021/ic0508371).
- [47] J. Liu, Y.-T. Kuo, K. J. Klabunde, C. Rochford, J. Wu, and J. Li. Novel Dye-Sensitized Solar Cell Architecture Using TiO₂-Coated Vertically Aligned Carbon Nanofiber Arrays. *ACS Appl. Mater. Interfaces*, 1(8):1645–1649 (2009). doi:[10.1021/am900316f](https://doi.org/10.1021/am900316f).
- [48] M. Graetzel. Recent Advances in Sensitized Mesoscopic Solar Cells. *Accounts of Chemical Research*, 42(11):1788–1798 (2009). doi:[10.1021/ar900141y](https://doi.org/10.1021/ar900141y).
- [49] J. Mertz. Radiative absorption, fluorescence, and scattering of a classical dipole near a lossless interface: a unified description. *Journal of the Optical Society of America B: Optical Physics*, 17(11):1906–1913 (2000).
- [50] K. R. Catchpole and A. Polman. Design principles for particle plasmon enhanced solar cells. *Applied Physics Letters*, 93(19):191113 (2008). doi:[10.1063/1.3021072](https://doi.org/10.1063/1.3021072).

-
- [51] J. N. Munday and H. A. Atwater. Large Integrated Absorption Enhancement in Plasmonic Solar Cells by Combining Metallic Gratings and Antireflection Coatings. *Nano Letters*, 11(6):2195–2201 (2010). doi:[10.1021/nl101875t](https://doi.org/10.1021/nl101875t).
- [52] H. A. Atwater and A. Polman. Plasmonics for improved photovoltaic devices. *Nature Materials*, 9(3):205–213 (2010). doi:[10.1038/nmat2629](https://doi.org/10.1038/nmat2629).
- [53] B. Tian, X. Zheng, T. J. Kempa, Y. Fang, N. Yu, G. Yu, J. Huang, and C. M. Lieber. Coaxial silicon nanowires as solar cells and nanoelectronic power sources. *Nature*, 449(7164):885–889 (2007). doi:[10.1038/nature06181](https://doi.org/10.1038/nature06181).
- [54] O. Hayden, R. Agarwal, and C. M. Lieber. Nanoscale avalanche photodiodes for highly sensitive and spatially resolved photon detection. *Nature Materials*, 5(5):352–356 (2006). doi:[10.1038/nmat1635](https://doi.org/10.1038/nmat1635).
- [55] J. S. Jie, W. J. Zhang, Y. Jiang, X. M. Meng, Y. Q. Li, and S. T. Lee. Photoconductive Characteristics of Single-Crystal CdS Nanoribbons. *Nano Letters*, 6(9):1887–1892 (2006). doi:[10.1021/nl060867g](https://doi.org/10.1021/nl060867g).
- [56] C. Soci, A. Zhang, B. Xiang, S. A. Dayeh, D. P. R. Aplin, J. Park, X. Y. Bao, Y. H. Lo, and D. Wang. ZnO Nanowire UV Photodetectors with High Internal Gain. *Nano Letters*, 7(4):1003–1009 (2007). doi:[10.1021/nl070111x](https://doi.org/10.1021/nl070111x).
- [57] R. Chen. Ultrahigh photocurrent gain in m-axial GaN nanowires. *Applied Physics Letters*, 91(22):223106– (2007). doi:[10.1063/1.2817595](https://doi.org/10.1063/1.2817595).
- [58] J. Zhu, Z. Yu, G. F. Burkhard, C.-M. Hsu, S. T. Connor, Y. Xu, Q. Wang, M. McGehee, S. Fan, and Y. Cui. Optical Absorption Enhancement in Amorphous Silicon Nanowire and Nanocone Arrays. *Nano Letters*, 9(1):279–282 (2008). doi:[10.1021/nl802886y](https://doi.org/10.1021/nl802886y).
- [59] Z. Fan, H. Razavi, J.-w. Do, A. Moriwaki, O. Ergen, Y.-L. Chueh, P. W. Leu, J. C. Ho, T. Takahashi, L. A. Reichertz, S. Neale, K. Yu, M. Wu, J. W. Ager, and A. Javey. Three-dimensional nanopillar-array photovoltaics on low-cost and flexible substrates. *Nature Materials*, 8(8):648–653 (2009). doi:[10.1038/nmat2493](https://doi.org/10.1038/nmat2493).
- [60] C. Soci, A. Zhang, X.-Y. Bao, H. Kim, Y. Lo, and D. Wang. Nanowire Photodetectors. *Journal of Nanoscience and Nanotechnology*, 10(3):1430–1449 (2010). doi:[10.1166/jnn.2010.2157](https://doi.org/10.1166/jnn.2010.2157).

- [61] P. Panayotatos and H. Card. Recombination in the space-charge region of Schottky barrier solar cells. *Solid-State Electronics*, 23(1):41–47 (**1980**). doi:[10.1016/0038-1101\(80\)90166-5](https://doi.org/10.1016/0038-1101(80)90166-5).
- [62] W. Qingqing, X. Gang, and H. Gaorong. Solvothermal synthesis and characterization of uniform CdS nanowires in high yield. *Journal of Solid State Chemistry*, 178(9):2680–2685 (**2005**). doi:[10.1016/j.jssc.2005.06.005](https://doi.org/10.1016/j.jssc.2005.06.005).
- [63] S. Oktik, G. J. Russell, and J. Woods. The correlation between current transport mechanisms and etch features in Au-CdS single-crystal Schottky diodes. *Semiconductor Science and Technology*, 2(10):661– (**1987**). doi:[10.1088/0268-1242/2/10/006](https://doi.org/10.1088/0268-1242/2/10/006).
- [64] Y. Gu, J. P. Romankiewicz, J. K. David, J. L. Lensch, L. J. Lauhon, E.-S. Kwak, and T. W. Odom. Local photocurrent mapping as a probe of contact effects and charge carrier transport in semiconductor nanowire devices. *Journal of Vacuum Science and Technology B*, 24(4):2172– (**2006**). doi:[10.1116/1.2216717](https://doi.org/10.1116/1.2216717).
- [65] Y. Gu, J. P. Romankiewicz, J. K. David, J. L. Lensch, and L. J. Lauhon. Quantitative Measurement of the Electron and Hole Mobility-Lifetime Products in Semiconductor Nanowires. *Nano Letters*, 6(5):948–952 (**2006**). doi:[10.1021/nl052576y](https://doi.org/10.1021/nl052576y).
- [66] M. D. Kelzenberg, D. B. Turner-Evans, B. M. Kayes, M. A. Filler, M. C. Putnam, N. S. Lewis, and H. A. Atwater. Photovoltaic Measurements in Single-Nanowire Silicon Solar Cells. *Nano Letters*, 8(2):710–714 (**2008**). doi:[10.1021/nl072622p](https://doi.org/10.1021/nl072622p).
- [67] D. Fu, J. Zou, K. Wang, R. Zhang, D. Yu, and J. Wu. Electrothermal Dynamics of Semiconductor Nanowires under Local Carrier Modulation. *Nano Letters*, 11(9):3809–3815 (**2011**). doi:[10.1021/nl2018806](https://doi.org/10.1021/nl2018806).
- [68] O. Madelung. *Semiconductors: Data Handbook*. Springer (**2004**).
- [69] R.-M. Ma, L. Dai, and G.-G. Qin. High-Performance Nano-Schottky Diodes and Nano-MESFETs Made on Single CdS Nanobelts. *Nano Letters*, 7(4):868–873 (**2007**). doi:[10.1021/nl062329+](https://doi.org/10.1021/nl062329+).
- [70] A. J. Frank, S. Glenis, and A. J. Nelson. Conductive polymer-semiconductor junction: characterization of poly(3-methylthiophene):cadmium sulfide based photoelectrochemical and photovoltaic cells. *Journal of Physical Chemistry*, 93(9):3818–3825 (**1989**). doi:[10.1021/j100346a088](https://doi.org/10.1021/j100346a088).

-
- [71] C. G. Van de Walle and J. Neugebauer. Universal alignment of hydrogen levels in semiconductors, insulators and solutions. *Nature*, 423(6940):626–628 (2003). doi:[10.1038/nature01665](https://doi.org/10.1038/nature01665).
- [72] A. K. Geim and K. S. Novoselov. The rise of graphene. *Nature Materials*, 6(3):183–191 (2007). doi:[10.1038/nmat1849](https://doi.org/10.1038/nmat1849).
- [73] K. S. Novoselov, Z. Jiang, Y. Zhang, S. V. Morozov, H. L. Stormer, U. Zeitler, J. C. Maan, G. S. Boebinger, P. Kim, and A. K. Geim. Room-Temperature Quantum Hall Effect in Graphene. *Science*, 315(5817):1379 (2007). doi:[10.1126/science.1137201](https://doi.org/10.1126/science.1137201).
- [74] M. Y. Han, B. Oezylmaz, Y. Zhang, and P. Kim. Energy Band-Gap Engineering of Graphene Nanoribbons. *Physical Review Letters*, 98(20):206805– (2007). doi:[10.1103/PhysRevLett.98.206805](https://doi.org/10.1103/PhysRevLett.98.206805).
- [75] Y. Zhang, T.-T. Tang, C. Girit, Z. Hao, M. C. Martin, A. Zettl, M. F. Crommie, Y. R. Shen, and F. Wang. Direct observation of a widely tunable bandgap in bilayer graphene. *Nature*, 459(7248):820–823 (2009). doi:[10.1038/nature08105](https://doi.org/10.1038/nature08105).
- [76] K. S. Kim, Y. Zhao, H. Jang, S. Y. Lee, J. M. Kim, K. S. Kim, J.-H. Ahn, P. Kim, J.-Y. Choi, and B. H. Hong. Large-scale pattern growth of graphene films for stretchable transparent electrodes. *Nature*, 457(7230):706–710 (2009). doi:[10.1038/nature07719](https://doi.org/10.1038/nature07719).
- [77] L. Gao, J. R. Guest, and N. P. Guisinger. Epitaxial Graphene on Cu(111). *Nano Letters*, 10(9):3512–3516 (2010). doi:[10.1021/nl1016706](https://doi.org/10.1021/nl1016706).
- [78] C. Gomez-Navarro, M. Burghard, and K. Kern. Elastic Properties of Chemically Derived Single Graphene Sheets. *Nano Letters*, 8(7):2045–2049 (2008). doi:[10.1021/nl801384y](https://doi.org/10.1021/nl801384y).
- [79] X. Wang, L. Zhi, and K. Mullen. Transparent, Conductive Graphene Electrodes for Dye-Sensitized Solar Cells. *Nano Letters*, 8(1):323–327 (2008). doi:[10.1021/nl072838r](https://doi.org/10.1021/nl072838r).
- [80] Z. Liu, Q. Liu, Y. Huang, Y. Ma, S. Yin, X. Zhang, W. Sun, and Y. Chen. Organic Photovoltaic Devices Based on a Novel Acceptor Material: Graphene. *Advanced Materials*, 20(20):3924–3930 (2008). doi:[10.1002/adma.200800366](https://doi.org/10.1002/adma.200800366).
- [81] F. Xia, T. Mueller, R. Golizadeh-Mojarad, M. Freitag, Y.-m. Lin, J. Tsang, V. Perebeinos, and P. Avouris. Photocurrent Imaging and Efficient Photon Detection in a Graphene Transistor. *Nano Letters*, 9(3):1039–1044 (2009). doi:[10.1021/nl8033812](https://doi.org/10.1021/nl8033812).

- [82] G. Giovannetti, P. A. Khomyakov, G. Brocks, V. M. Karpan, J. van den Brink, and P. J. Kelly. Doping Graphene with Metal Contacts. *Physical Review Letters*, 101:026803 (2008). doi:[10.1103/PhysRevLett.101.026803](https://doi.org/10.1103/PhysRevLett.101.026803).
- [83] S. Kitamura. Effect of Oxygen upon Sintered Cadmium Sulphide Photoconducting Films. *Journal of the Physical Society of Japan*, 15 (12):2343 (1960). doi:[10.1143/JPSJ.15.2343](https://doi.org/10.1143/JPSJ.15.2343).
- [84] R. J. D'Arcy. Work Function of Titanium Films. *Surface Science*, 36:783 (1973). doi:[10.1016/0039-6028\(73\)90421-4](https://doi.org/10.1016/0039-6028(73)90421-4).
- [85] D. R. Lide (editor). *CRC Handbook of Chemistry and Physics*. CRC, London (2008).
- [86] H. Dollefeld, K. Hoppe, J. Kolny, K. Schilling, H. Weller, and A. Eychmuller. Investigations on the stability of thiol stabilized semiconductor nanoparticles. *Physical Chemistry Chemical Physics*, 4(19):4747–4753 (2002). doi:[10.1039/B202101C](https://doi.org/10.1039/B202101C).
- [87] M. Ishigami, J. H. Chen, W. G. Cullen, M. S. Fuhrer, and E. D. Williams. Atomic Structure of Graphene on SiO₂. *Nano Letters*, 7(6):1643–1648 (2007). doi:[10.1021/nl070613a](https://doi.org/10.1021/nl070613a).
- [88] T. O. Wehling, K. S. Novoselov, S. V. Morozov, E. E. Vdovin, M. I. Katsnelson, A. K. Geim, and A. I. Lichtenstein. Molecular Doping of Graphene. *Nano Letters*, 8(1):173–177 (2008). doi:[10.1021/nl072364w](https://doi.org/10.1021/nl072364w).
- [89] B. H. Juarez, M. Meyns, A. Chanaewa, Y. Cai, C. Klinke, and H. Weller. Carbon Supported CdSe Nanocrystals. *Journal of the American Chemical Society*, 130(46):15282–15284 (2008). doi:[10.1021/ja805662h](https://doi.org/10.1021/ja805662h).
- [90] J. Moser. Current-induced cleaning of graphene. *Applied Physics Letters*, 91(16):163513– (2007). doi:[10.1063/1.2789673](https://doi.org/10.1063/1.2789673).
- [91] D. Shi, Y. Cao, N. Pootrakulchote, Z. Yi, M. Xu, S. M. Zakeeruddin, M. Gratzel, and P. Wang. New Organic Sensitizer for Stable Dye-Sensitized Solar Cells with Solvent-Free Ionic Liquid Electrolytes. *The Journal of Physical Chemistry C*, 112(44):17478–17485 (2008). doi:[10.1021/jp807191w](https://doi.org/10.1021/jp807191w).
- [92] Q. Liu, Z. Liu, X. Zhang, L. Yang, N. Zhang, G. Pan, S. Yin, Y. Chen, and J. Wei. Polymer Photovoltaic Cells Based on Solution-Processable Graphene and P3HT. *Advanced Functional Materials*, 19(6):894–904 (2009). doi:[10.1002/adfm.200800954](https://doi.org/10.1002/adfm.200800954).

-
- [93] A. F. Oskooi, D. Roundy, M. Ibanescu, P. Bermel, J. Joannopoulos, and S. G. Johnson. Meep: A flexible free-software package for electromagnetic simulations by the FDTD method. *Computer Physics Communications*, 181(3):687–702 (**2010**). doi:[10.1016/j.cpc.2009.11.008](https://doi.org/10.1016/j.cpc.2009.11.008).
 - [94] S. Ninomiya and S. Adachi. Optical properties of wurtzite CdS. *Journal of Applied Physics*, 78(2):1183–1190 (**1995**). doi:[10.1063/1.360355](https://doi.org/10.1063/1.360355).
 - [95] G. K. Mor, K. Shankar, M. Paulose, O. K. Varghese, and C. A. Grimes. Use of Highly-Ordered TiO₂ Nanotube Arrays in Dye-Sensitized Solar Cells. *Nano Letters*, 6(2):215–218 (**2006**). doi:[10.1021/nl052099j](https://doi.org/10.1021/nl052099j).
 - [96] J. A. Dionne, H. J. Lezec, and H. A. Atwater. Highly Confined Photon Transport in Subwavelength Metallic Slot Waveguides. *Nano Letters*, 6(9):1928–1932 (**2006**). doi:[10.1021/nl0610477](https://doi.org/10.1021/nl0610477).
 - [97] L. Douillard, F. Charra, Z. Korczak, R. Bachelot, S. Kostcheev, G. Lerondel, P.-M. Adam, and P. Royer. Short Range Plasmon Resonators Probed by Photoemission Electron Microscopy. *Nano Letters*, 8(3):935–940 (**2008**). doi:[10.1021/nl080053v](https://doi.org/10.1021/nl080053v).
 - [98] M. Hochberg, T. Baehr-Jones, C. Walker, and A. Scherer. Integrated plasmon and dielectric waveguides. *Optics Express*, 12(22):5481–5486 (**2004**).
 - [99] R. W. Heeres, S. N. Dorenbos, B. Koene, G. S. Solomon, L. P. Kouwenhoven, and V. Zwiller. On-Chip Single Plasmon Detection. *Nano Letters*, 10(2):661–664 (**2010**). doi:[10.1021/nl903761t](https://doi.org/10.1021/nl903761t).
 - [100] D. M. Koller, A. Hohenau, H. Ditlbacher, N. Galler, F. Reil, F. R. Aussenegg, A. Leitner, E. J. W. List, and J. R. Krenn. Organic plasmon-emitting diode. *Nature Photonics*, 2(11):684–687 (**2008**). doi:[10.1038/nphoton.2008.200](https://doi.org/10.1038/nphoton.2008.200).
 - [101] R. F. Oulton, V. J. Sorger, T. Zentgraf, R.-M. Ma, C. Gladden, L. Dai, G. Bartal, and X. Zhang. Plasmon lasers at deep subwavelength scale. *Nature*, 461(7264):629–632 (**2009**). doi:[10.1038/nature08364](https://doi.org/10.1038/nature08364).
 - [102] A. L. Falk, F. H. L. Koppens, C. L. Yu, K. Kang, N. de Leon Snapp, A. V. Akimov, M.-H. Jo, M. D. Lukin, and H. Park. Near-field electrical detection of optical plasmons and single-plasmon sources. *Nature Physics*, 5(7):475–479 (**2009**). doi:[10.1038/nphys1284](https://doi.org/10.1038/nphys1284).

- [103] P. Neutens, P. Van Dorpe, I. De Vlaminck, L. Lagae, and G. Borghs. Electrical detection of confined gap plasmons in metal-insulator-metal waveguides. *Nature Photonics*, 3(5):283–286 (**2009**). doi:[10.1038/nphoton.2009.47](https://doi.org/10.1038/nphoton.2009.47).
- [104] H. Ditlbacher. Organic diodes as monolithically integrated surface plasmon polariton detectors. *Applied Physics Letters*, 89(16):161101– (**2006**). doi:[10.1063/1.2362975](https://doi.org/10.1063/1.2362975).
- [105] I. P. Radko, S. I. Bozhevolnyi, G. Brucoli, L. Martin-Moreno, F. J. Garcia-Vidal, and A. Boltasseva. Efficiency of local surface plasmon polariton excitation on ridges. *Physical Review B*, 78:115115 (**2008**). doi:[10.1103/PhysRevB.78.115115](https://doi.org/10.1103/PhysRevB.78.115115).
- [106] J. Homola (editor). *Surface Plasmon Resonance Based Sensors*. Springer (**2006**).
- [107] H. L. Offerhaus, B. van den Bergen, M. Escalante, F. B. Segerink, J. P. Korterik, and N. F. van Hulst. Creating Focused Plasmons by Noncollinear Phasematching on Functional Gratings. *Nano Letters*, 5:2144–2148 (**2005**). doi:[10.1021/nl0515089](https://doi.org/10.1021/nl0515089).
- [108] J. Wang, M. S. Gudiksen, X. Duan, Y. Cui, and C. M. Lieber. Highly Polarized Photoluminescence and Photodetection from Single Indium Phosphide Nanowires. *Science*, 293(5534):1455–1457 (**2001**). doi:[10.1126/science.1062340](https://doi.org/10.1126/science.1062340).
- [109] A. G. Mathewson and H. P. Myers. Absolute Values of the Optical Constants of Some Pure Metals. *Physica Scripta*, 4(6):291– (**1971**). doi:[10.1088/0031-8949/4/6/009](https://doi.org/10.1088/0031-8949/4/6/009).
- [110] S. A. Maier. *Plasmonics*. Springer (**2007**).
- [111] H. Ditlbacher. Efficiency of local light-plasmon coupling. *Applied Physics Letters*, 83(18):3665– (**2003**). doi:[10.1063/1.1625107](https://doi.org/10.1063/1.1625107).
- [112] Y. Gu, E.-S. Kwak, J. L. Lensch, J. E. Allen, T. W. Odom, and L. J. Lauhon. Near-field scanning photocurrent microscopy of a nanowire photodetector. *Applied Physics Letters*, 87(4):043111 (**2005**). doi:[10.1063/1.1996851](https://doi.org/10.1063/1.1996851).
- [113] M. Lira-Cantu, A. Chafiq, J. Faissat, I. Gonzalez-Valls, and Y. Yu. Oxide/polymer interfaces for hybrid and organic solar cells: Anatase vs. Rutile TiO₂. *Solar Energy Materials & Solar Cells*, 95:1362–1374 (**2011**). doi:[10.1016/j.solmat.2010.12.028](https://doi.org/10.1016/j.solmat.2010.12.028).
- [114] J. Zhao, X. Wang, R. Chen, and L. Li. Fabrication of titanium oxide nanotube arrays by anodic oxidation. *Solid State Communications*, 134:705–710 (**2005**). doi:[10.1016/j.ssc.2005.02.028](https://doi.org/10.1016/j.ssc.2005.02.028).

-
- [115] D. Gong, C. A. Grimes, O. K. Varghese, W. Hu, R. Singh, Z. Chen, and E. C. Dickey. Titanium oxide nanotube arrays prepared by anodic oxidation. *Journal of Materials Research*, 16:3331–3334 (2001). doi:[10.1557/JMR.2001.0457](https://doi.org/10.1557/JMR.2001.0457).
- [116] B. Yanga, M. Uchidab, H.-M. Kimc, X. Zhanga, and T. Kokubo. Preparation of bioactive titanium metal via anodic oxidation treatment. *Biomaterials*, 25:1003–1010 (2004). doi:[10.1016/S0142-9612\(03\)00626-4](https://doi.org/10.1016/S0142-9612(03)00626-4).
- [117] B. J. Hwang and J. R. Hwang. Kinetic model of anodic oxidation of titanium in sulphuric acid. *Journal of Applied Electrochemistry*, 23:1056–1062 (1993). doi:[10.1007/BF00266129](https://doi.org/10.1007/BF00266129).
- [118] J.-S. Lee, M. V. Kovalenko, J. Huang, D. S. Chung, and D. V. Talapin. Band-like transport, high electron mobility and high photoconductivity in all-inorganic nanocrystal arrays. *Nature Nanotechnology*, 6:348 (2011). doi:[10.1038/NNANO.2011.46](https://doi.org/10.1038/NNANO.2011.46).
- [119] M. V. Kovalenko, M. Scheele, and D. V. Talapin. Colloidal Nanocrystals with Molecular Metal Chalcogenide Surface Ligands. *Science*, 324:1417–1420 (2009). doi:[10.1126/science.1170524](https://doi.org/10.1126/science.1170524).
- [120] D. V. Talapin and C. B. Murray. PbSe Nanocrystal Solids for n- and p-Channel Thin Film Field-Effect Transistors. *Science*, 310:86–89 (2005). doi:[10.1126/science.1116703](https://doi.org/10.1126/science.1116703).
- [121] J. D. Servaites, M. A. Ratner, and T. J. Marks. Organic solar cells: A new look at traditional models. *Energy & Environmental Science*, pages – (2011). doi:[10.1039/c1ee01663f](https://doi.org/10.1039/c1ee01663f).
- [122] M. S. A. Abdou, F. P. Orfino, Y. Son, and S. Holdcroft. Interaction of Oxygen with Conjugated Polymers: Charge Transfer Complex Formation with Poly(3-alkylthiophenes). *Journal of the American Chemical Society*, 119:4518–4524 (1997). doi:[10.1021/ja964229j](https://doi.org/10.1021/ja964229j).
- [123] L. Onsager. Deviations from Ohm’s Law in Weak Electrolytes. *Journal of Chemical Physics*, 2:599 (1934). doi:[10.1063/1.1749541](https://doi.org/10.1063/1.1749541).
- [124] C. L. Braun. Electric field assisted dissociation of charge transfer states as a mechanism of photocarrier production. *Journal of Chemical Physics*, 80:4157 (1984). doi:[10.1063/1.447243](https://doi.org/10.1063/1.447243).

- [125] V. D. Mihailetschi, L. J. A. Koster, J. C. Hummelen, and P. Blom. Photocurrent Generation in Polymer-Fullerene Bulk Heterojunctions. *Physical Review Letters*, 93:216601 (2004). doi:[10.1103/PhysRevLett.93.216601](https://doi.org/10.1103/PhysRevLett.93.216601).
- [126] D. Hertela, E. V. Soha, H. Baessler, and L. J. Rothberga. Electric field dependent generation of geminate electron-hole pairs in a ladder-type π -conjugated polymer probed by fluorescence quenching and delayed field collection of charge carriers. *Chemical Physics Letters*, 361:99–105 (2002). doi:[10.1016/S0009-2614\(02\)00898-9](https://doi.org/10.1016/S0009-2614(02)00898-9).
- [127] H. Baessler and E. V. Emelianova. Steady-State Photoconduction in Amorphous Organic Solids. *Advances in Polymer Science*, 223:1–28 (2010). doi:[10.1007/12_2009_11](https://doi.org/10.1007/12_2009_11).
- [128] C. Deibel, D. Mack, J. Gorenflot, A. Schoell, S. Krause, F. Reinert, D. Rauh, and V. Dyakonov. Energetics of Excited States in the Conjugated Polymer Poly(3-hexylthiophene). *Physical Review B*, 81:085202 (2010). doi:[10.1103/PhysRevB.81.085202](https://doi.org/10.1103/PhysRevB.81.085202).
- [129] G. Dicker, M. P. de Haas, L. D. Siebbeles, and J. M. Warman. Electrodeless time-resolved microwave conductivity study of charge-carrier photogeneration in regioregular poly(3-hexylthiophene) thin films. *Physical Review B*, 70:045203 (2004). doi:[10.1103/PhysRevB.70.045203](https://doi.org/10.1103/PhysRevB.70.045203).
- [130] I.-W. Hwang, D. Moses, and A. J. Heeger. Photoinduced Carrier Generation in P3HT/PCBM Bulk Heterojunction Materials. *Journal of Physical Chemistry C*, 112:4350–4354 (2008). doi:[10.1021/jp075565x](https://doi.org/10.1021/jp075565x).
- [131] J. R. Williams, L. DiCarlo, and C. M. Marcus. Quantum Hall Effect in a Gate-Controlled p-n Junction of Graphene. *Science*, 317:638 (2007). doi:[10.1126/science.1144657](https://doi.org/10.1126/science.1144657).
- [132] N. M. Gabor, Z. Zhong, K. Bosnick, J. Park, and P. L. McEuen. Extremely Efficient Multiple Electron-Hole Pair Generation in Carbon Nanotube Photodiodes. *Science*, 325:1367 (2009). doi:[10.1126/science.1176112](https://doi.org/10.1126/science.1176112).
- [133] J. U. Lee, P. P. Gipp, and C. M. Heller. Carbon nanotube p-n junction diodes. *Applied Physics Letters*, 85(1):145–147 (2004). doi:[10.1063/1.1769595](https://doi.org/10.1063/1.1769595).
- [134] N. J. Pinto, R. Perez, C. H. Mueller, N. Theofylaktos, and F. A. Miranda. Dual input AND gate fabricated from a single channel poly(3-hexylthiophene) thin film field effect transistor. *Journal of Applied Physics*, 99(8):084504 (2006). doi:[10.1063/1.2188131](https://doi.org/10.1063/1.2188131).

-
- [135] U. Zschieschang, F. Ante, M. Schloerholz, M. Schmidt, K. Kern, and H. Klauk. Mixed Self-Assembled Monolayer Gate Dielectrics for Continuous Threshold Voltage Control in Organic Transistors and Circuits. *Advanced Materials*, 22:4489–4493 (**2010**). doi:[10.1002/adma.201001502](https://doi.org/10.1002/adma.201001502).
- [136] L.-L. Chua, J. Zaumseil, J.-F. Chang, E. C.-W. Ou, P. K.-H. Ho, H. Sirringhaus, and R. H. Friend. General observation of n-type field-effect behaviour in organic semiconductors. *Nature*, 434:194 (**2005**). doi:[10.1038/nature03376](https://doi.org/10.1038/nature03376).
- [137] D. Rep, A. Morpurgo, and T. Klapwijk. Doping-dependent charge injection into regioregular poly(3-hexylthiophene). *Organic electronics*, 4:201–207 (**2003**). doi:[10.1016/S1566-1199\(03\)00016-8](https://doi.org/10.1016/S1566-1199(03)00016-8).
- [138] D. Russella, T. Kuglera, C. Newsomea, S. Lia, M. Ishidaa, and T. Shimodab. Dedoping of organic semiconductors. *Synthetic Metals*, 156:769–772 (**2006**). doi:[10.1016/j.synthmet.2006.01.013](https://doi.org/10.1016/j.synthmet.2006.01.013).
- [139] H.-H. Liao, C.-M. Yang, C.-C. Liu, S.-F. Horng, H.-F. Meng, and J.-T. Shy. Dynamics and reversibility of oxygen doping and de-doping for conjugated polymer. *Journal of Applied Physics*, 103(10):104506 (**2008**). doi:[10.1063/1.2917419](https://doi.org/10.1063/1.2917419).
- [140] J. Zaumseil, C. L. Donley, J.-S. Kim, R. H. Friend, and H. Sirringhaus. Efficient Top-Gate, Ambipolar, Light-Emitting Field-Effect Transistors Based on a Green-Light-Emitting Polyfluorene. *Adv. Mater.*, 18(20):2708–2712 (**2006**). doi:[10.1002/adma.200601080](https://doi.org/10.1002/adma.200601080).

Publications

- T. Dufaux, J. Boettcher, M. Burghard, and K. Kern, "Photocurrent Distribution in Graphene - CdS Nanowire Devices", *Small*, 6, 1868 (2010)
- T. Dufaux, J. Dorfmueller, R. Vogelgesang, M. Burghard, and K. Kern, "Surface plasmon coupling to nanoscale Schottky-type electrical detectors", *Applied Physics Letters*, 97, 161110 (2010)
- D. Shopova-Gospodinova, Z. Burghard, T. Dufaux, M. Burghard, and J. Bill, "Mechanical and electrical properties of polymer-derived Si-C-N ceramics reinforced by octadecylamine - modified single-wall carbon nanotubes", *Composites Science and Technology*, 71, 931 (2011)
- T. Lutz, A. Kabakchiev, T. Dufaux, C. Wolpert, Z. Wang, M. Burghard, K. Kuhnke, and K. Kern, "Scanning tunneling luminescence of individual CdSe nanowires", *Small*, 7, 2396 (2011)
- H. Borchert, F. Witt, A. Chanaewa, F. Werner, J. Dorn, T. Dufaux, M. Kruszynska, A. Jandke, M. Hölting, T. Alfere, J. Böttcher, C. Gimmler, C. Klinke, M. Burghard, A. Mews, H. Weller, and J. Parisi, "Vertically oriented carbon nanostructures for more efficient charge transport in polymer-based solar cells", *Accepted, The Journal of Physical Chemistry*
- T. Dufaux, M. Burghard, and K. Kern, "Charge recombination characteristics along Schottky-contacts to CdS nanowires", *Submitted*

Curriculum Vitae

Personal information

Name	Thomas Dufaux
Date of birth	25.10.1983
Place of birth	Cologne, Germany
Nationality	German, Belgian

Education

since May 2008	Research staff at the Max-Planck Institute for Solid State Reseach the department of Prof. Klaus Kern
----------------	--

PhD student at the École Polytechnique Fédéral de Lausanne

March 2008	Diploma Thesis at the research center Jülich Institute of Bio- and Nano Systems (IBN2), Prof. Offenhäusser
------------	---

2002 - 2008	Study of Electrical Engineering at the RWTH-Aachen
-------------	--

2001	"European Abitur" at the European School Ixelles Brussels, Belgium
------	---

Acknowledgements

I am thankful to Prof. Klaus Kern for supervising my thesis and giving me the possibility to work on my PhD at the Max-Planck Institute of Solid State Research in Stuttgart.

I am grateful to Dr. Marko Burghard, my direct advisor, for giving me the opportunity to work in his group. I would like to thank for numerous fruitful discussions, the great freedom I enjoyed during my work and the continuous support during my thesis.

I would like to thank the people of the university Hamburg for the helpful and scientific co-operation, especially Prof. Alf Mews, Dr. Jens Böttcher, Dr. Anton Myalitsin, Dr. Alina Chanaewa, and Sebastian Schäfer.

I thank Dr. Hagen Klauk for regularly trying to answer my many questions on organic materials and Dr. Stephan Rauschenbach for giving me support for scientific and machining tasks.

Especially I would like to thank the people of the organic electronics group Dr. Daniel Kälblein, Dr. Frederick Ante, Hyeyeon Ryu, Ulrike Kraft, and Dr. Ute Zschieschang for many clarifying discussions, the possibility to use their equipment, and diverse social activities.

I am grateful to Dr. Ralf Vogelgesang and Dr. Jens Dorfmueller for the help with the optical setup and their support to resolve my many questions on optics.

I appreciate the technical support of Robert Preuss, for helping me to build my experimental setups and for many non-scientific meetings.

I would also like to thank my office colleagues Sören Krotzky, Pascal Gehring, Moritz Esslinger, and Dr. Thomas Maurer for the friendly atmosphere and the many discussions about scientific and non-scientific topics.

I thank Sabine Birtel for all the paperwork support during my work at the MPI.

I appreciated the continuous technical support in the clean room facilities by Thomas Reindl, Ulrike Weizmann, Marion Hagel, and Achim Güth, but as well the help of Martin Siemers and

Rafail Chaikevitch for their help in all technical questions.

My thanks also go to the other department members who supported me in my work like Eberhard Ulrich Stützel, Dr. Ravi Sundaram, Dr. Adarsh Sagar, Dr. Bo Gao, Dr. Thomas Weitz, Gordon Rinke, Dr. Vivek Pachauri, Tim Koppenrath, and Dr. Alicia Forment-Aliaga.

Finally, I am grateful to my family and especially to my wife Xiaowei who always supported me and followed my work with great interest.